



### 저작자표시-비영리-동일조건변경허락 2.0 대한민국

이용자는 아래의 조건을 따르는 경우에 한하여 자유롭게

- 이 저작물을 복제, 배포, 전송, 전시, 공연 및 방송할 수 있습니다.
- 이차적 저작물을 작성할 수 있습니다.

다음과 같은 조건을 따라야 합니다:



저작자표시. 귀하는 원저작자를 표시하여야 합니다.



비영리. 귀하는 이 저작물을 영리 목적으로 이용할 수 없습니다.



동일조건변경허락. 귀하가 이 저작물을 개작, 변형 또는 가공했을 경우에는, 이 저작물과 동일한 이용허락조건하에서만 배포할 수 있습니다.

- 귀하는, 이 저작물의 재이용이나 배포의 경우, 이 저작물에 적용된 이용허락조건을 명확하게 나타내어야 합니다.
- 저작권자로부터 별도의 허가를 받으면 이러한 조건들은 적용되지 않습니다.

저작권법에 따른 이용자의 권리는 위의 내용에 의하여 영향을 받지 않습니다.

이것은 [이용허락규약\(Legal Code\)](#)을 이해하기 쉽게 요약한 것입니다.

[Disclaimer](#)

공학박사 학위논문

# **Structure control of electrocatalysts for enhanced ORR in PEMFC cathode**

고분자 전해질막 연료전지 공기극내  
산소환원반응 향상을 위한 전극촉매의 구조 조절

2012년 8월

서울대학교 대학원

화학생물공학부

이 원 두



# Structure control of electrocatalysts for enhanced ORR in PEMFC cathode

지도교수 이 호 인

이 논문을 공학박사 학위논문으로 제출함  
2012년 5월

서울대학교 대학원  
화학생명공학부  
이 원 두

이원두의 공학박사 학위논문을 인준함  
2012년 6월

위 원 장 \_\_\_\_\_ (인)

부위원장 \_\_\_\_\_ (인)

위 원 \_\_\_\_\_ (인)

위 원 \_\_\_\_\_ (인)

위 원 \_\_\_\_\_ (인)

# 학위논문 원문제공 서비스에 대한 동의서

본인의 학위논문에 대하여 서울대학교가 아래와 같이 학위논문 제공하는 것에 동의합니다.

## 1. 동의사항

- ① 본인의 논문을 보존이나 인터넷 등을 통한 온라인 서비스 목적으로 복제할 경우 저작물의 내용을 변경하지 않는 범위 내에서의 복제를 허용합니다.
- ② 본인의 논문을 디지털화하여 인터넷 등 정보통신망을 통한 논문의 일부 또는 전부의 복제, 배포 및 전송 시 무료로 제공하는 것에 동의합니다.

## 2. 개인(저작자)의 의무

본 논문의 저작권을 타인에게 양도하거나 또는 출판을 허락하는 등 동의 내용을 변경하고자 할 때는 소속대학(원)에 공개의 유보 또는 해지를 즉시 통보하겠습니다.

## 3. 서울대학교의 의무

- ① 서울대학교는 본 논문을 외부에 제공할 경우 저작권 보호장치(DRM)를 사용하여야 합니다.
- ② 서울대학교는 본 논문에 대한 공개의 유보나 해지 신청 시 즉시 처리해야 합니다.

논문제목 : Structure control of electrocatalysts for enhanced ORR in PEMFC cathode

학위구분 : 석사  · 박사

학 과 : 화학생물공학부

학 번 : 2006-23220

연 락 처 : 02-880-7077

저 작 자 : 이 원 두 (인)

제 출 일 : 2012년 8월 일

서울대학교총장 귀하

## **Abstract**

# **Structure control of electrocatalysts for enhanced ORR in PEMFC cathode**

Weon-Doo Lee

School of Chemical and Biological Engineering

The Graduate School

Seoul National University

Polymer electrolyte membrane fuel cell (PEMFC) has received considerable attention for transportation applications due to its high energy density, relatively low operation temperature, zero or low emission of pollutants, and minimal corrosion problems. However, the commercial viability of PEMFC is still hindered by several problems, including poor kinetics of cathodic reactions and high costs of Pt-based electrocatalysts. It is well known that most of performance losses due to the deviation from the thermodynamic potential of PEMFC come from the cathodic reaction. In order to improve in oxygen reduction reaction (ORR), the highly active PEMFC cathodic catalyst will be developed.

Highly dispersed Pt nanoparticles supported on carbon were synthesized by modified polyol reduction. Based on the XRD and TEM results, we confirmed that the reduction time and the ethylene glycol

concentration affected the size of Pt nanoparticles. 20Pt/C(M-10), which had the smallest Pt particles among all the catalysts prepared with various reduction conditions, had an average Pt particle size of 1.2 nm with quite a narrow distribution between 0.5 and 2 nm. Moreover, this catalyst showed the greatest EAS area, the highest MOR activity, and the highest ORR activity because of the smallest Pt nanoparticles. In addition, 40Pt/C(M) catalyst synthesized by the optimized reduction condition showed higher EAS and better catalytic activity than a commercial one in PEMFC. The method used in this study provided an easy and reproducible procedure for the preparation of Pt nanoparticles supported on carbon.

An effective method was developed for the preparation of size-controlled  $\text{Ce}_{0.5}\text{Zr}_{0.5}\text{O}_2$  in Pt/ $\text{Ce}_{0.5}\text{Zr}_{0.5}\text{O}_2$ -C electrocatalyst for low-temperature fuel cell. From XRD patterns and TEM images, Pt and  $\text{Ce}_{0.5}\text{Zr}_{0.5}\text{O}_2$  nanoparticles were well-dispersed on the carbon support. Catalysts containing  $\text{Ce}_{0.5}\text{Zr}_{0.5}\text{O}_2$  showed higher electrochemical activity for oxygen reduction reaction (ORR) than the catalysts without  $\text{Ce}_{0.5}\text{Zr}_{0.5}\text{O}_2$  addition because desorption of OH adsorbed on Pt occurred easily. The IR spectra result showed that the ORR activity increased with increasing the amount of coordinated hydroxyl groups on  $\text{CeO}_2$ . It suggested that  $\text{CeO}_2$  enhanced the ORR activity due to the lateral repulsion between OH adsorbed on Pt and OH coordinated on its neighbor  $\text{Ce}_{0.5}\text{Zr}_{0.5}\text{O}_2$ .

Core-shell typed PtPd nanoparticles on carbon support were developed to increase the alloyed active surface area. In order to prepare a core-shell structure, all the catalysts were prepared by polyol reduction with

a concentration of 27  $\mu\text{M}$  NaOH. In this NaOH concentration, most of Pd precursor changed to  $\text{Pd}(\text{OH})_2$ . During the polyol reduction procedure, core was formed from Pt precursor and remaining Pd precursor, and then the formed  $\text{Pd}(\text{OH})_2$  was reduced on the surface of the core. The Pd atoms reduced from  $\text{Pd}(\text{OH})_2$  was placed on the outside of the nanocores. Resultantly, core(Pt-rich)-shell(Pd)-typed nanoparticles could be prepared by polyol reduction. In order to observe the relation between metal composition and ORR activity, several catalysts with different Pt/Pd ratio were prepared. Among the catalysts, 5Pt1Pd/C showed the highest ORR activity in the kinetic current region (0.85~0.90 V) in spite of larger particle size than that of 7Pt1Pd/C because the 7Pt1Pd/C had insufficient Pd atoms in the shell. From the CO-stripping test, it was observed that Pd atoms in the shell decreased the OH adsorption on the Pt surface.

**Keywords:** Polymer electrolyte membrane fuel cell, Pt nanoparticle,

**$\text{Ce}_{0.5}\text{Zr}_{0.5}\text{O}_2$ , PtPd nanoparticle, Polyol reduction**

**Student Number: 2006-23220**

# Contents

Abstract .....	i
List of Tables .....	viii
List of Figures.....	ix
Chapter 1. Introduction .....	1
1.1. Fuel cell basics .....	1
1.1.1. Fuel cells as a electrochemical energy conversion device .....	1
1.1.2. Polymer electrolyte membrane fuel cell (PEMFC) .....	3
1.1.3. Electrode reactions.....	5
1.2. Electrocatalyst.....	11
1.2.1. De-alloying in bimetallic systems.....	11
1.2.2.1. Electronic effect.....	16
1.2.2.2. Geometric effect .....	19
Chapter 2. Preparation of Pt nanoparticles on carbon support using modified polyol reduction for low- temperature fuel cells .....	22

2.1. Introduction.....	22
2.2. Experimental.....	24
2.2.1. Electrocatalyst preparation .....	24
2.2.2. Physical characterization .....	26
2.2.3. Electrochemical activity .....	27
2.2.4. Single-cell test.....	27
2.3. Results and discussion.....	29
2.3.1. 20 wt% Pt/C catalyst characterization .....	29
2.3.1.1. Physical characterization.....	29
2.3.1.2. Electrochemical characterizations in a half-cell .....	33
2.3.2. 40 wt% Pt/C catalyst characterization .....	40
2.3.2.1 Physical characterization.....	40
2.3.2.2 Electrochemical characterization in a single-cell .....	47
2.4. Conclusions.....	52
Chapter 3. Preparation and characterization of Pt/Ce <sub>0.5</sub> Zr <sub>0.5</sub> O <sub>2</sub> -C catalyst for ORR.....	53
3.1. Introduction.....	53
3.2. Experimental.....	55
3.2.1. Preparation of Pt/Ce <sub>0.5</sub> Zr <sub>0.5</sub> O <sub>2</sub> -C.....	55
3.2.2. Physical characterization .....	56

3.2.3. Electrochemical activity .....	57
3.3. Results and discussion.....	58
3.3.1. 10 wt% Ce <sub>0.5</sub> Zr <sub>0.5</sub> O <sub>2</sub> -C support characterization .....	58
3.3.2. 20 wt% Pt/Ce <sub>0.5</sub> Zr <sub>0.5</sub> O <sub>2</sub> -C catalyst characterization.....	59
3.3.2.1. Physical characterization.....	59
3.3.2.2. Electrochemical activity.....	65
3.4. Conclusions.....	75

## Chapter 4. Development of core-shell typed PtPd/C catalyst for ORR in PEMFC by polyol reduction .....

4.1 Introduction.....	76
4.2. Experimental.....	77
4.2.1. Preparation of PtPd/C.....	77
4.2.2. Physical characterization .....	78
4.2.3 Electrochemical activity .....	79
4.3. Results and discussion.....	80
4.3.1. 3Pt1Pd/C catalyst characterization .....	80
4.3.2.1. Physical characterization.....	80
4.3.2.2. Electrochemical activity.....	93
4.3.2 xPtPd/C catalyst characterization.....	102
4.3.2.1. Physical characterization.....	102

4.3.2.2. Electrochemical activity.....	106
4.3.3. 5Pt1Pd/Ce <sub>0.5</sub> Zr <sub>0.5</sub> O <sub>2</sub> -C catalyst characterization.....	112
4.4. Conclusions.....	120
References .....	121
Abstract (in Korean).....	137

## List of Tables

Table 1. Description of major fuel cell types .....	9
Table 2. The pH values after reduction process and the physical and electrochemical properties of the prepared 20 wt% Pt/C catalysts .....	36
Table 3. Condition of hydrothermal treatment and crystallite size calculated from XRD pattern .....	61
Table 4. Crystallite size of Pt/C and Pt/CZO-C catalysts .....	68
Table 5. ICP-AES data and atomic ratio of PtPd/C catalysts .....	90
Table 6. Crystallite sizes of metal and metal oxide calculated from XRD data .....	104

## List of Figures

Fig. 1. Plots of cell potential vs. current density for the leading types of fuel cells [2]. .....	10
Fig. 2. Schematic illustration of the formation of a chemical bond between an adsorbate valence level and the s- and d-states of a transition metal surface [21]. .....	20
Fig. 3. Free-energy diagrams for the oxygen reduction reaction on Pt-based transition metal alloys [42]. .....	21
Fig. 4. X-ray diffraction patterns of 20 wt% Pt/C catalysts prepared by modified polyol reduction with various concentrations of reducing agent. ..	34
Fig. 5. X-ray diffraction patterns of 20 wt% Pt/C catalysts prepared by modified polyol reduction with various reduction times. ....	35
Fig. 6. TEM images and histograms of the particle size distribution of (a) 20Pt/C(C) and (b) 20Pt/C(M-10). .....	37
Fig. 7. Cyclic voltammograms for the prepared and the commercial 20 wt% Pt/C catalysts to observe the electrochemical active surface area. ....	38
Fig. 8. (a) Mass-normalized and (b) area-normalized activity for methanol oxidation of the 20 wt% Pt/C catalysts. ....	43
Fig. 9. X-ray diffraction patterns of the prepared and the commercial 40 wt% Pt/C catalysts. ....	44
Fig. 10. TEM image and the corresponding size distribution diagram of the 40Pt/C(M). .....	45

Fig. 11. XPS spectra of Pt 4f for (a) 40Pt/C(M) and (b) 40Pt/C(P). .....	46
Fig. 12. Cyclic voltammograms of the prepared and the commercial 40 wt% Pt/C catalysts as a cathode of the PEMFC. ....	50
Fig. 13. Performances of the single-cell from PEMFCs using the prepared and the commercial 40 wt% Pt/C catalysts as a cathode. ....	51
Fig. 14. X-ray diffraction patterns of CZO-C supports prepared by hydrothermal treatment. ....	60
Fig. 15. TEM images of (a) CZO-C-1, (b) CZO-C-2, and (c) CZO-C-3. ....	62
Fig. 16. TGA curves of Pt/CZO-C catalysts. ....	63
Fig. 17. X-ray diffraction patterns of Pt/CZO-C and Pt/C catalysts. ....	67
Fig. 18. TEM images of (a) Pt/C(S), (b) Pt/CZO-C-1, (c) Pt/CZO-C-2, and (d) Pt/CZO-C-3. ....	69
Fig. 19. (a) Linear scan voltammograms of Pt/C and Pt/CZO-C catalysts in 1 M HClO <sub>4</sub> saturated with pure oxygen at the scan rate of 1 mV/s and with the rotating speed of 2500 rpm. ....	70
Fig. 20. Mass activities at 0.80 and 0.85 V for Pt/C and Pt/CZO-C catalysts. ....	71
Fig. 21. Tafel plot for Pt/C and Pt/CZO-C catalysts. ....	72
Fig. 22. Cyclic voltammograms of the Pt/C and Pt/CZO-C catalysts in 0.5 M H <sub>2</sub> SO <sub>4</sub> at the scan rate of 20 mV/s. ....	73
Fig. 23. IR spectroscopy of Pt/C and Pt/CZO-C catalysts. ....	74
Fig. 24. pH profile in polyol reduction. ....	83
Fig. 25. (a) X-ray diffraction pattern of Pt/C and (b) crystallite size calculated from XRD data. ....	84

Fig. 26. (a) X-ray diffraction pattern of Pd/C and (b) crystallite size calculated from XRD data. ....	85
Fig. 27. (a) X-ray diffraction pattern of PtPd/C and (b) crystallite size calculated from XRD data. ....	88
Fig. 28. Expanded X-ray diffraction patterns of PtPd/C catalysts. ....	89
Fig. 29. TEM images and histograms of the particle size distribution of (a) PtPd/C(1) , (b) PtPd/C(27), and (c) PtPd/C(70) catalysts. ....	91
Fig. 30. X-ray diffraction patterns of Pd/C and Pd/Pt/C catalysts. ....	94
Fig. 31. TPR data of (a) Pd/C, (b) Pt-Pd/C, and (c) PtPd/C catalysts. ....	96
Fig. 32. Schematic diagram of core-shell typed nanoparticles preparation. ..	97
Fig. 33. CO-stripping voltammograms of Pt/C, Pd/C, and PtPd/C catalysts. ....	98
Fig. 34. Linear scan voltammograms of PtPd/C catalysts in 1 M HClO <sub>4</sub> saturated with pure oxygen at the scan rate 1 mV/s with the rotating speed of 2500 rpm. ....	100
Fig. 35. Mass activities at 0.85 and 0.90 V for Pt/C and PtPd/C catalysts. ....	101
Fig. 36. X-ray diffraction patterns of Pt/C, 7Pt1Pd/C, 5Pt1Pd/C, 3Pt1Pd/C, and Pd/C catalysts. ....	103
Fig. 37. TEM images of (a) 3Pt1Pd/C, (b) 5Pt1Pd/C(c) 7Pt1Pd/C (d) Pt/C catalysts. ....	105
Fig. 38. Cyclic voltammograms for (a) Pt/C and PtPd/C catalysts and (b) Pd/C catalyst. ....	108
Fig. 39. Linear scan voltammograms of Pd/C, 3Pt1Pd/C, 5Pt1Pd/C, 7Pt1Pd/C, and Pt/C catalysts in 1 M HClO <sub>4</sub> saturated with pure oxygen at the scan rate of 1 mV/s and with the rotating speed of 2500 rpm. ....	109

Fig. 40. Mass activities at 0.85 and 0.90 V for Pd/C, 3Pt1Pd/C, 5Pt1Pd/C, 7Pt1Pd/C, and Pt/C catalysts. ....	110
Fig. 41. Cyclic CO-stripping voltammograms of Pd/C, 3Pt1Pd/C, 5Pt1Pd/C, 7Pt1Pd/C, and Pt/C catalysts. ....	111
Fig. 42. TEM images and EDS data of 5Pt1Pd/Ce <sub>0.5</sub> Zr <sub>0.5</sub> O <sub>2</sub> -C catalyst. ....	114
Fig. 43. Linear scan voltammograms of 5Pt1Pd/Ce <sub>0.5</sub> Zr <sub>0.5</sub> O <sub>2</sub> -C catalyst and 5Pt1Pd/C in 1 M HClO <sub>4</sub> saturated with pure oxygen at the scan rate 1 mV/s with the rotating speed of 2500 rpm. ....	115
Fig. 44. Mass activities at 0.85 and 0.90 V for 5Pt1Pd/Ce <sub>0.5</sub> Zr <sub>0.5</sub> O <sub>2</sub> -C and 5Pt1Pd/C catalysts. ....	116
Fig. 45. Tafel plot for 5Pt1Pd/Ce <sub>0.5</sub> Zr <sub>0.5</sub> O <sub>2</sub> -C and 5Pt1Pd/C catalysts. ....	117
Fig. 46. Cyclic voltammograms of 5Pt1Pd/Ce <sub>0.5</sub> Zr <sub>0.5</sub> O <sub>2</sub> -C and 5Pt1Pd/C catalysts in 0.5 M H <sub>2</sub> SO <sub>4</sub> at the scan rate of 20 mV/s. ....	118
Fig. 47. CO-stripping voltammograms of 5Pt1Pd/Ce <sub>0.5</sub> Zr <sub>0.5</sub> O <sub>2</sub> -C and 5Pt1Pd/C catalysts. ....	119

## CHAPTER I

---

# INTRODUCTION

### 1.1. Fuel cell basics

#### 1.1.1. Fuel cells as a electrochemical energy conversion device

Electrical energy can be obtained by conversion from chemical energy, which is the most practical energy source such as oil and coal. Fuel as an energy source is burnt in a combustion engine, such as gasoline or diesel engine, and then, can be converted to mechanical energy and following electrical energy by an electrical generator. This multi-step process and the high operating temperature for the production of electricity limit the maximum efficiency and induce a considerable emission level, which is an important cause for air pollution. Fuel cell also releases heat under the operation conditions. However, the heat generated in a fuel cell originates from the energy difference between the initial reactants and final product.  $H_2$  and  $O_2$  as reactants are placed at higher molecular state than that of water. This energy difference is converted to the heat. Nevertheless, the main output in a fuel cell is not the heat but the electric currents.

Fuel cell is considered as a continuous energy conversion device with an input of fuel ( $H_2$  and  $O_2$ ) and an output of  $H_2O$  and electricity. This continuous production of electric energy is a key difference between a fuel cell and a battery. A battery is also an

electrochemical energy conversion device. The electrode in a battery is the active and oxidizable material that can be charged and discharged. While a battery is required to be charged by the outside electricity, a fuel cell continuously operates and produces electricity directly from the electrochemical reaction.

Fuel cells, therefore, combine the advantages of both combustion engines and batteries, and at the same time, eliminate the drawbacks of both. Thus, fuel cells continuously operate without recharging like batteries. In the most common H<sub>2</sub>-O<sub>2</sub> fuel cells, hydrogen gas is fed into the anode catalyst layer, while oxygen gas (or air) is supplied to the cathode catalyst layer. The main role of electrocatalysts is to bring a redox potential at the electrodes as close as possible to the equilibrium potentials of hydrogen oxidation reactions (HOR) and oxygen reduction reactions (ORR). Hydrogen gas supplied to the anode is splitted to protons and electrons. Protons and electrons go to the cathode layer through a polymer electrolyte membrane and external path, respectively. At the cathode, molecular oxygen is reduced to water by the protons and electrons generated at the anode.

Fuel cell also possesses some serious disadvantages. Because of prohibitive prices, its competitive power is lower than that of combustion engine or battery. Although the power density of fuel cell has been improved over the past decades, combustion engines and batteries generally outperform fuel cells on a volumetric power density basis (power per unit volume). Furthermore, operational temperature should be

concerned to the durability of fuel cells.

### 1.1.2. Polymer electrolyte membrane fuel cell (PEMFC)

Fuel cells are typically classified according to the electrolyte employed. There are five major types of fuel cells, as follows:

1. Polymer electrolyte membrane fuel cell (PEMFC)
2. Phosphoric acid fuel cell (PAFC)
3. Alkaline fuel cell (AFC)
4. Molten carbonate fuel cell (MCFC)
5. Solid-oxide fuel cell (SOFC)

Characteristics of each fuel cell are briefly described in Table 1 [1]. These fuel cells follow the same underlying electrochemical principles. However, all the fuel cells operate at different temperatures, incorporate different materials, and often have different fuel tolerance and performance, as shown in Table 1. Usually, operation temperature is limited up to about 200 °C due to the high water vapor pressure of aqueous electrolytes and the rapid degradation at high temperatures. While the low-temperature fuel cells with aqueous electrolytes are restricted to H<sub>2</sub> as a fuel, at high temperature, CO and CH<sub>4</sub> can be used as fuels because of their rapid reaction kinetics.

Fig. 1 shows typical cell potential vs. current density plots for a PEMFC and the other fuel cells [2]. All fuel cells exhibit all forms of overpotential losses (activation, mass transport, and ohmic). During operation of a fuel cell, the single cell potential ( $E$ )

is diminished by the losses in overpotential at the anode and cathode, and in the electrolyte. Therefore,  $E$  can be expressed by the following equation:

$$E = E_r - \eta_{act,a} - \eta_{act,c} - \eta_{ohm} - \eta_{mt,a} - \eta_{mt,c} \quad (1-1)$$

Where,  $E_r$  is the thermodynamic reversible potential,  $\eta_{act,a}$  and  $\eta_{act,c}$  are the activation overpotentials at the anode and cathode, respectively.  $\eta_{mt,a}$  and  $\eta_{mt,c}$  are the mass-transport and concentration overpotentials at the anode and cathode, respectively.  $\eta_{ohm}$  is the ohmic overpotential in the cell. These all overpotentials are dependent on activation, mass transport, and ohmic overpotentials. Slow charge-transfer steps in electrocatalytic reactions contribute to activation overpotentials. Reactants with low solubility such as hydrogen or oxygen gas are limited to reach the electrode surface by diffusion, migration, and convection. This limitation contributes to mass transport overpotentials. Finally, ohmic overpotential arises predominantly during the passage of an electric current and it is due to electrical resistances for the transport of ions from one electrode to the other in an electrochemical cell. In the case of PEMFCs, the oxygen reduction reaction (ORR) limits the overall cell efficiency due to its sluggish kinetics, i.e., large activation overpotential.

PEMFC, which is the primary candidate for light duty vehicles, for building, and potentially for much smaller applications such as replacements for rechargeable batteries, operate at about 80 °C. The solid electrolyte used in PEMFC is a solid

organic polymer (polytetrafluoroethylene, PTFE), which acts as a proton conductor. These cells have several advantages compared to the other types; low operating temperature, fast response to power demand, and minimal corrosion due to the solid electrolyte. In PEMFCs, water management has a critical importance for the efficient performance. The membrane should be always hydrated for the proton-transfer to prevent it from drying. Although PEMFCs have many advantages, these cells also have disadvantages such as CO-poisoning and high costs.

As mentioned above, PEMFCs employ a thin polymer membrane as an electrolyte. Protons are the ionic charge carrier in a PEMFC membrane. The electrochemical half reactions in a PEMFC are as follows:



The dissociation of hydrogen gas occurs in the anode layer, and the oxygen gas is reduced to form water in the cathode layer.

### 1.1.3 Electrode reactions

Electrode kinetics are of vital importance in determining the performance of fuel cells. The series of steps involved in electrode reactions in the fuel cells are as follows:

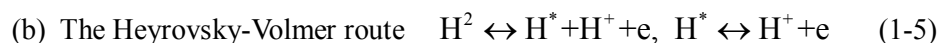
- (a) Dissolution of the reactant gases in the electrolyte
- (b) Diffusion of the dissolved reactant gas to the active sites on the electrode
- (c) Adsorption reactants and/or intermediate species formed by adsorption on the

electrode from the electrolyte

- (d) Charge transfer between reactant and electrode or from the above mentioned adsorbed species to the electrode
- (e) Diffusion of species away from the electrode
- (f) Transfer of conducting ions from one electrode to the other through the electrolyte
- (g) Transfer of electrons from one electrode to the other through the external load

Among these steps, adsorption and charge transfer steps in the interface between a solid electrode and an electrolyte are briefly described.

The anode reaction is referred to hydrogen oxidation reaction (HOR). The mechanism of this reaction is by far the most thoroughly investigated electrochemical reaction system [3-5] and contains three elementary steps [6], i.e., Tafel step (recombination reaction), Volmer step (charge transfer reaction), and Heyrovsky step (ion-plus-atoms reaction). Among various reaction routes proposed so far, the following two routes are generally accepted.



Where, \* denotes the adsorbed state,  $H^+$  is proton in the solution, and e is a free electron at the Fermi level in the electrode.

The cathode reaction is oxygen reduction reaction (ORR), in which molecular

oxygen adsorbs to the electrode surface such as Pt and reduced to water through four-electron direct pathway [7]. However, oxygen reduction is considerably more complex than hydrogen oxidation because of the strong O-O bond, the formation of highly stable Pt-O or Pt-OH species, and the generation of hydrogen peroxide (H<sub>2</sub>O<sub>2</sub>). In a PEMFC, as in the case of other low or intermediate temperature fuel cells (PAFC, AFC), Pt and Pt alloy are the best electrocatalysts. The overpotential for the HOR is considerably lower than that for the ORR on cathode catalysts; for example, in a PEMFC operating at current densities of 1 Acm<sup>-2</sup>, the overpotential at the anode is about 20 mV and at the oxygen electrode is in the range of 300-400 mV. About one half of the overpotential at the cathode is due to its loss at open circuit. Thus, the departure of the potential of the PEMFC from the reversible value is due to the extremely low cathodic exchange current density (*i*<sub>0</sub>). To reveal this sluggish kinetics, various theories have been proposed.

The overall ORR in an acid medium is shown as follows:



The ORR is highly irreversible reaction even on Pt surface, because the ORR operates at high potential region under severe corrosive environment. Even if Pt has the high surface-nobleness, it is natural that Pt surface forms the adsorption of various intermediates containing oxygen such as O, OH, and OOH. In early work on O<sub>2</sub> electrochemistry, before reliable thermodynamic data were available, the potential 1.08

V vs. RHE was considered as the reversible value for reaction (1-6). After that, thermodynamics contribute to indirect determination of the equilibrium potential (1.229 V) based on the free energy of formation of liquid water from the equilibrium potentials of a metal-insoluble metal oxide couple, i.e., Ag-Ag<sub>2</sub>O or Hg-HgO, together with the free energy of formation of the metal oxide. However, many researchers tried to reveal the nature of irreversible rest potential of most “ordinary” platinum and other noble metal electrodes in the presence of O<sub>2</sub> in the solution. Among various theories for explaining the nature of the irreversible rest potential, the concept of a mixed potential is generally accepted. It means that some anodic reaction simultaneously occurs with the four-electron cathodic reduction. Among various anodic reactions, the formation of surface oxides, the anodic dissolution, and the oxidation of a metal by oxygen diffusion into the bulk of a metal are regarded as the main reason for the mixed potential. Recently, it has been founded that high surface coverage of adsorbed OH blocks the active sites for the O<sub>2</sub> adsorption and following reduction to water [8]. This site-blocking effect of OH can be decreased and optimized by forming “Pt-skin” Pt-M (M = Fe, Co, Ni) alloys due to the optimization of the binding energies of oxygenated species such as O<sub>2</sub>, O, OH, and OOH. This control of binding energy between oxygen and metal surface has been explained by the downshift of d-band center of surface Pt.

Table 1. Description of major fuel cell types [1]

	PEMFC	PAFC	AFC	MCFC	SOFC
Electrolyte	Polymer membrane	Liquid H <sub>3</sub> PO <sub>4</sub> (immobilized)	Liquid KOH (immobilized)	Molten carbonate	Ceramic
Charge carrier	H <sup>+</sup>	H <sup>+</sup>	OH <sup>-</sup>	CO <sub>3</sub> <sup>2-</sup>	O <sup>2-</sup>
Operating temperature	80 °C	200 °C	60–220 °C	650 °C	600–1000 °C
Catalyst	Pt	Pt	Pt	Ni	Perovskites (ceramic)
Cell components	Carbon based	Carbon based	Carbon based	Stainless based	Ceramic based
Fuel compatibility	H <sub>2</sub> , Methanol	H <sub>2</sub>	H <sub>2</sub>	H <sub>2</sub> , CH <sub>4</sub>	H <sub>2</sub> , CH <sub>4</sub> , CO

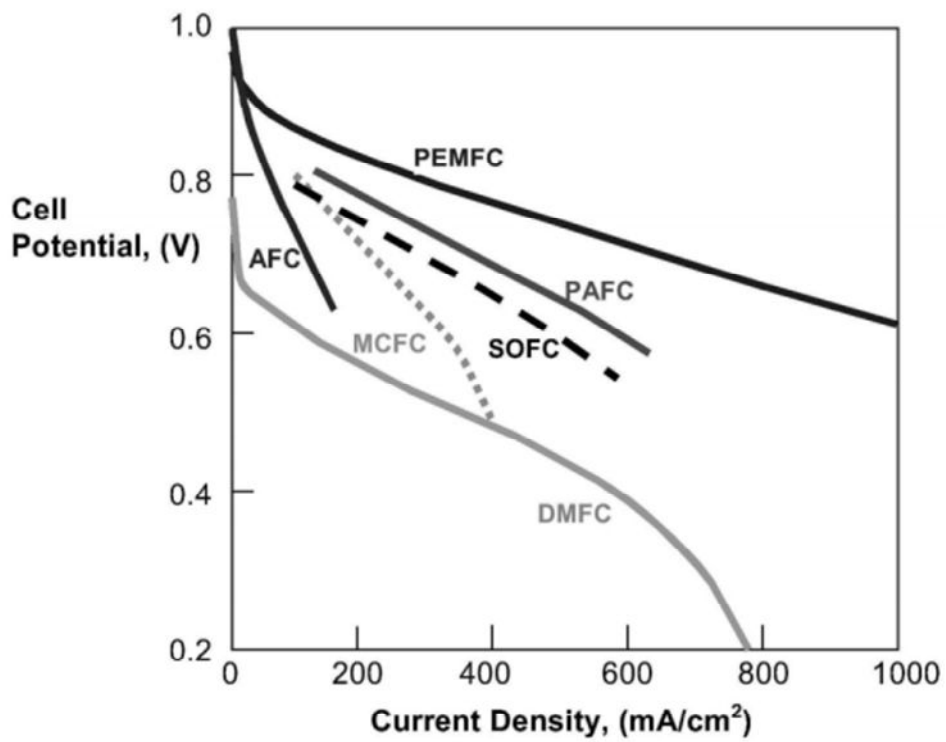


Fig. 1. Plots of cell potential vs. current density for the leading types of fuel cells [2].

## 1.2. Electrocatalyst

### 1.2.1. De-alloying in bimetallic systems

De-alloying in transition metal nanoalloys are induced by various reasons, i.e., segregation and dissolution of one component, interaction between adsorbing intermediates and surface atoms, and phase separation due to oxide formation. Because these de-alloying behaviors are strongly dependent on environmental and preparation conditions, in this section, we focused on the segregation phenomenon. The degree of segregation and mixing in A-B nanoalloys depends on the following factors [9]:

(1) Relative strengths of A-A, B-B, and A-B bonds. To a first approximation, if A-A bonds are strongest, this favors mixing; otherwise, segregation is favored, with the species forming strongest homonuclear bonds tending to be at the center (core) of the cluster.

(2) Surface energies of bulk elements A and B. The element with lowest surface energy tends to segregate to the surface.

(3) Relative atomic sizes. Smaller atoms tend to occupy the more sterically confined core, especially in icosahedral or cubooctahedral clusters, where the core undergoes compression.

(4) Charge transfer. Electron transfer from less to more electronegative elements favoring mixing.

(5) Strength of binding to surface ligands (surfactants). For supported or passivated clusters, the element that binds most strongly to the support or ligands may be pulled out toward the surface.

(6) Specific electronic/magnetic effects. Certain sizes, compositions, and/or segregation arrangements may be stabilized by electronic shell structure (as in the jellium model) or electron spin interactions.

Segregation behavior has been well understood through density functional theory (DFT) calculations, assuming that segregation occurs by only the interaction between two metals. One metal component alloyed with another may enrich the surface region depending on the heat of segregation and the surface mixing energy [10]. This segregation phenomenon is of interest as it may enhance or suppress electrocatalytic reactions [11,12]. For catalysts in fuel cells, Pt has become the most widely used electrocatalyst, and has been applied in the type of nanoalloys used for large electrochemical active surface area (EAS) and for maximum activity of an electrocatalytic reaction; therefore, surface segregation of Pt is of vital importance in electrocatalysis

In preparation of Pt-based alloy nanoparticles, when dissolved Pt ions are co-reduced with precursors of other metals, such as Ni, Co, and Ru, by various reducing agents, one observes the low surface composition of Pt, even in the presence of stabilizers, mainly due to the higher redox potential of Pt relative to other transition

metals, with the exception of Au [13,14]. Discrepancy between surface and bulk compositions in as-prepared nanoalloys may be related to many factors, such as a redox priority of metal precursors [15], surface energy of each metal component [16,17], and interaction with various adsorbing species present during a preparation procedure [18-20]. A surface with low Pt concentration results in low catalytic activity due to decreased EAS and the increased number of the second metal, which binds strongly with oxygen-containing species [21]. When using proper stabilizers that induce stronger binding with Pt relative to the second metal, enrichment of the second metal in the surface can be suppressed. However, observance of the higher surface concentration of Pt relative to the nominal value is difficult. It is therefore required that the surface concentration of Pt be increased by use of several techniques, such as thermal heating in an appropriate atmosphere [22-24], or chemical leaching of the non-noble metal [25-28] in the surface layer. Heat treatment can be used not only for removing residual impurities and unwanted oxides, but also for segregating Pt atoms at the surface. Pt segregation by heat treatment can be a novel method for improving undesirable surface composition.

Numerous theoretical studies have been carried out to elucidate the driving force and the tendency of Pt-based alloys toward surface segregation [10,11,16,23,29-37]. First-principles approaches are usually implemented based on density functional theory (DFT). Using this method, trends in segregation energies in transition metal alloys

have been reported. Christensen *et al.* [10] constructed surface phase diagrams from surface energy as a function of the surface composition and calculated the heat of segregation and the surface mixing energy. In the same line with Christensen *et al.*, Ruban *et al.* [11,33] improved the accuracy of theoretical surface segregation energies and tabulated the qualitative picture of segregation energies containing various solvent and solute transition metals. According to their results, late-group transition metals as solute in the host of early-group transition metals usually show negative values. In addition, in the hosts of Fe, Ru, and Os, noble metal solutes with more than half-filled d-bands (e.g. Pd, Pt, Ag, and Au etc.) have more negative segregation energies for lower surface energy, dependent mainly on the amount of surface core-level shifts (SCLSs). Recently, Greeley *et al.* [38] showed that trends in the thermodynamics of surface alloy dissolution in acidic media generally follow trends in surface segregation energies, and that the dissolution potential of Pt in “Pt-skins” produced by surface segregation of Pt<sub>3</sub>M alloys (M = Fe, Co, or Ni) is higher than that of Pt<sub>3</sub>M alloy surfaces. The increased dissolution potential of “Pt-skin” surface is consistent with the positive shift of OH adsorption to higher potential in the findings of Stamenkovic *et al.* [39] for Pt<sub>3</sub>Ni(111). Therefore, surface segregation energy is one of the most important factors to be considered in the initial choice of alloy systems.

Surface segregation of Pt can be of significance in electrocatalytic activities such as the methanol oxidation reaction (MOR) [22] and oxygen reduction reaction (ORR)

[24,39], because surface Pt atoms are active sites for electrochemical reactions. Furthermore, modification of d-character of surface Pt atoms by segregation is normally desirable for stable electrode materials with higher dissolution potential in fuel cells [38], because the surface energy of the alloy can be lowered by Pt segregation to the surface, as mentioned above. Ma *et al.* [11] reported Pt surface segregation energies for 16 metals. In their results, the surface segregation energy for Pt<sub>3</sub>Ru(111) alloys is -0.83 eV. The value is more negative when compared to that of other transition metals, with the exception of Re and Mo. This means that Pt enrichment at the surface can readily occur in the Pt-Ru alloy system. Experimental results of Pt segregation in several alloy systems, including Pt-Ru, have already been reported [22,23]. Despite this, electrochemical measurements of Pt segregation in carbon-supported Pt-Ru nanoparticles were scarce.

### 1.2.2. Electronic and geometric effects on electrocatalyst

The rate of electrochemical reaction and the chemisorptions are dependent on two basic properties of the electrocatalyst surface, i.e., the electronic and geometric characters. Although the electronic and geometric structures of a surface usually cannot be varied independently, it is very useful to consider the two as the independent factors on the reactivity of the catalyst surface. The primary way to influence the activity of a catalyst is through a change in the electronic factor [40]. Transition metals are mainly used as electrocatalysts. In particular, the valence band structure has the most impact

on the interaction with neighboring atoms. The modification in the electronic structure controls the binding energy of reactant molecules on surface atoms. The geometric effect correlates to the surface structure of the catalysts and its relationship to the reactant species. Thus, the separation of the surface atoms, strain, and defects (i.e., steps and twins) can affect on the catalytic activity.

#### 1.2.2.1. Electronic effect

Density functional theory (DFT) calculations have become an important tool for understanding the properties of metal surfaces and their reactivity, including the effects of structure, alloying, and adsorption. This theoretical approach has begun to suggest the design of surfaces with specific catalytic properties of interest. In fuel cells, the electrochemical reactions such as HOR and ORR have been explained by this theoretical approach. In the case of the ORR, it is truly needed to reduce a large overpotential even on Pt. Nørskov *et al.* have already shown the origin of the ORR [41]. Furthermore, they suggested the promising candidates with the enhanced ORR rate and the higher stability [42].

Alloying Pt with other transition metals can downshift the d-band center position of surface Pt [43]. This shift dominates the trends in the trends in binding energy of adsorbates, i.e., oxygen-containing species. In the d-band model, the simplest one-electron description of the quantum mechanics of atoms and molecules interacting with a metal surface is assumed and provide the essential physics for understanding the

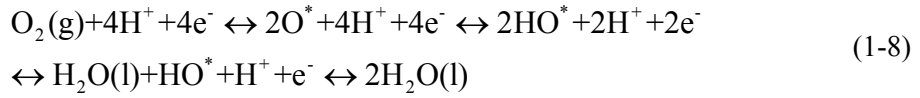
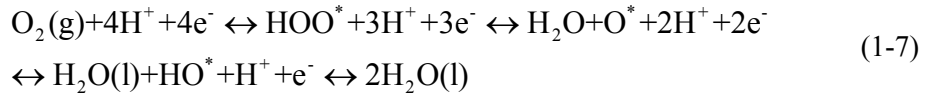
concept of the interaction between metal and adsorbates. The narrow d bands are a consequence of the small coupling matrix element  $V_{dd}$  between the localized d states; one of the important conclusions from tight binding theory is that the band width is proportional to  $V_{dd}$  [21,40]. Since d bands are narrow, the interaction of an adsorbate state with the d electrons of a surface gives rise to bonding and antibonding states just as in a simple two-state problem, as shown in Fig. 2.

In general, the coupling of the adsorbate states to the metal d-bands will depend on a number of parameters, i.e., the energy of the adsorbate state(s), the d-density of states projected onto the metal atoms, and the coupling matrix element. Therefore, changes in the position of d-band cannot fully explain trends in reactivity of all transition metals. However, if surface metal is fixed (for instance, an oxygen atom bonding to a Pt atom), its reactivity with different substrates can be conceptually explained with this model. This thesis is focused on the oxygen reduction reaction. Therefore, the binding energy of oxygen is representative of the activity, because oxygen has the scaling relationship with  $O_2$ , OH, and OOH.

As the d-band center shifts up, a distinctive antibonding state appears above the Fermi level. The antibonding states above the Fermi level are empty, and the bond becomes increasingly stronger as their numbers increase. Thus, strong bonding occurs if the antibonding states are shifted up through the Fermi level (and become empty), and weak bonding occurs if antibonding states are shifted down through the Fermi

level (and become filled). Consequently, a Pt overlayer on different substrates (surface alloys) can result in different reactivities in the ORR.

The oxygen reduction reaction can occur only when dissolved oxygen molecules diffuse and adsorb to metal surface. Nørskov *et al.* suggested two simple mechanisms of the ORR, i.e., dissociative and associative mechanisms. The first intermediate of O<sub>2</sub> determines the mechanism [41,42].



Where, \* denotes an adsorbed state. Pt and Pd usually follow the associative mechanism, and their rate-limiting step is a water formation. This implies that OH\* is a stable adsorbate on Pt or Pd. This reaction pathway for the associative mechanism is obtained from the free energy change diagram in Fig. 3 [42]. As can be seen in this diagram, Pt-based alloy shows the increased free energy change at the OOH\* formation step. However, the transfer rate to remove OH\* from the surface to form water is increased due to the increased free energy change of OH\*. Based on the overview of the reaction mechanism, the electronic modification of d-character of surface Pt is closely connected to the binding energy of oxygen and the subsequent ORR activity.

#### 1.2.2.2. Geometric effect

The chemisorptions and reaction properties of a metal surface depend on the electronic as well as the geometric structures of the surface. Although the electronic and geometric structures of a surface usually cannot be varied independently in the most cases, it is very useful to consider the two as causing independent effects on the reactivity of a surface. The geometric effect indicates that adsorbates or reaction complexes interact in different geometric arrangements with surface atoms with identical local electronic properties. The simplest measure of the geometric effect is thus the coordination number of the adsorbate with respect to the surface atoms. Therefore, the geometric factors can contain strain, defect, shape, and size effects of nanocrystallites.

Simple molecules such as di-oxygen were considered to be affected by only the electronic factor. Balbuena *et al.* have clearly demonstrated that the enhanced ORR activity for the “Pt-skin” Pt<sub>3</sub>Ni(111) and Pt<sub>3</sub>Co(111) alloys are not caused by geometric effects [11]. On the other side, Markovic *et al.* have shown that the ORR activity of supported Pt nanoparticles depends on the particle size and relating surface irregularities such as defects (step and twin) [44,45].

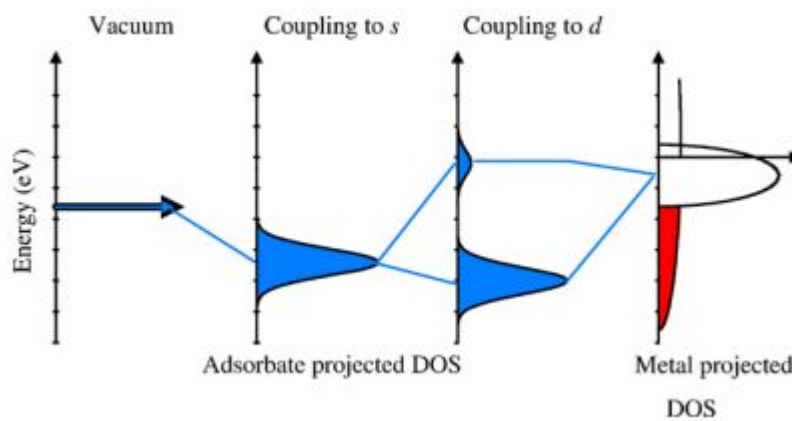


Fig. 2. Schematic illustration of the formation of a chemical bond between an adsorbate valence level and the *s*- and *d*-states of a transition metal surface [21].

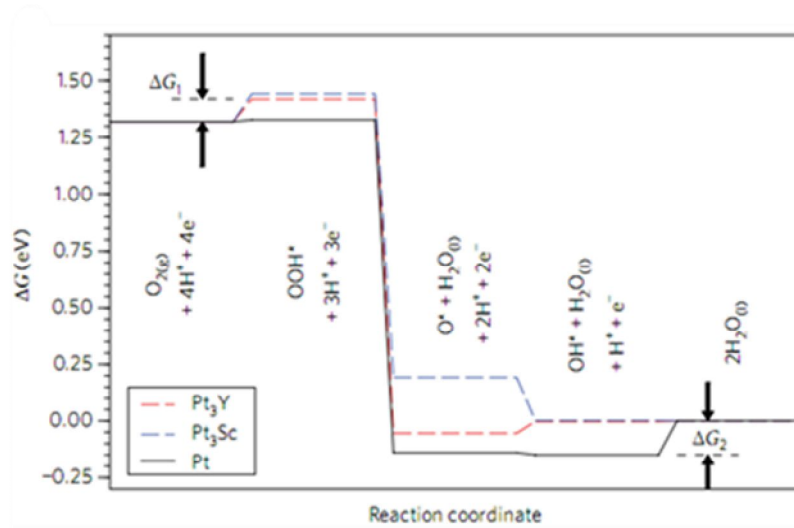


Fig. 3. Free-energy diagrams for the oxygen reduction reaction on Pt-based transition metal alloys [42].

## CHAPTER II

---

---

# Preparation of Pt nanoparticles on carbon support using modified polyol reduction for low-temperature fuel cells

## 2.1. Introduction

Low-temperature fuel cells have been largely investigated due to their various advantages such as high energy efficiency, low pollutant emission, and low operating temperature [46,47]. Regardless of these advantages, there are still many obstacles to overcome before realizing commercial application [48—51]. One of the major problems in low-temperature fuel cells is the use of expensive Pt/C as an electrocatalyst. Pt/C is a major catalyst in low-temperature fuel cells due to its high activity and superior stability [52,53]. However, catalyst preparation with high Pt loading still remains an unsolved problem due to poor reproducibility and low dispersion of the metal particles [54].

Great attention has been paid to the synthesis of small-sized and highly dispersed Pt nanoparticles in order to increase their surface availability as well as to reduce the cost [55—57]. So far, various preparation methods have been developed such as the

borohydride reduction [58] and the microemulsion [59] and colloidal methods [60]. However, these methods could not provide highly dispersed Pt nanoparticles for a catalyst with high Pt loading [61].

Recently, polyol reduction using ethylene glycol as both a reducing agent and solvent has received great attention since it provides satisfactory size control and highly dispersed nanoparticles without needing any additional stabilizers [62—64]. In the polyol reduction, the glycolate produced from ethylene glycol oxidation acts as a stabilizer for metal colloids. Therefore, well-dispersed Pt-based electrocatalyst are obtained.

In order to enhance the surface area of Pt nanoparticles, variously different modified polyol reductions were investigated. Song *et al.* applied a pulse-microwave procedure to avoid the agglomeration of the Pt nanoparticles [65]. Oh *et al.* adjusted the acidity of solution and the sort of purging gas to obtain highly dispersed Pt nanoparticles [66]. However, studies on the relation between reduction condition for conventional polyol reduction and particle size are rare.

Pure ethylene glycol is generally used as a solvent in the conventional polyol reduction, and the particle size of Pt increases with reaction rate for Pt reduction [67]. In the present study, aqueous (not pure) ethylene glycol instead of pure one was employed as a reducing agent in order to decrease the reducing rate for better particle

size control. First, 20 wt% Pt/C catalyst was prepared varying the reaction condition of reduction temperature, concentration of reducing agent, and reduction time to determine the optimum condition. After determining the optimum condition, a 40 wt% Pt/C was synthesized under the optimum reduction condition for a 20 wt% Pt/C catalyst to use in a single-cell cathode. The synthesized catalyst was compared with a catalyst prepared by the conventional polyol reduction. In order to confirm the particle size, the prepared catalysts were analyzed with several analysis tools including X-ray diffraction (XRD), transmission electron microscopy (TEM), and X-ray photoelectron spectroscopy (XPS). The electrochemical activities of the prepared catalysts were evaluated and compared with those of commercial catalysts.

## **2.2. Experimental**

### **2.2.1. Electrocatalyst preparation**

20 wt% Pt/C catalysts for the half-cell test were prepared by a modified polyol reduction. 1 g of chloroplatinic acid ( $\text{H}_2\text{PtCl}_6 \cdot 6\text{H}_2\text{O}$ , Kojima Chemicals) was dissolved in a 200 mL of ethylene glycol (Acros Organics). The solution (6.6 mL) was introduced to ethylene glycol aqueous solution (150 mL) with 0.05 g of carbon (Vulcan XC-72, Cabot Co.) in a Teflon bottle. Then, a 1 M NaOH (Daejung Chemicals) aqueous solution was slowly added to increase the pH of the mixture to 13. Subsequently, the mixture was refluxed at 90 °C with  $\text{N}_2$  purging to remove the organic

by-products and oxygen. After cooling to room temperature, a 3 M HCl (Matsunoen Chemicals) aqueous solution was added until the pH reached 2. The Teflon bottle was placed in a stainless steel vessel and sealed tightly, and hydrothermal treatment was performed in an oven at 160 °C for 10 h. After the hydrothermal treatment, the mixture was filtered, washed using distilled water, and dried in a vacuum oven for 24 h. Finally, the dried powder was heat-treated in air at 160 °C for 24 h to completely remove the solvent, which negatively affects the catalytic activity. During the hydrothermal and heat treatment, Pt nanoparticle reduced by modified polyol reduction was not oxidized to PtO or PtO<sub>2</sub> because temperatures of the treatment are not high enough to oxidize Pt [68]. In the 20 wt% Pt/C preparation, the concentration of the reducing agent and the reduction time were controlled to determine the optimum reduction condition of the modified polyol reduction. The catalysts, which were prepared with various concentrations of the reducing agent (ethylene glycol:H<sub>2</sub>O = 1:4, 1:2, 1:1, 2:1, and 4:0) and a constant reduction time (10 h), were denoted as 20Pt/C(M— $\alpha$ ), where  $\alpha$  represents the volume ratio of ethylene glycol to H<sub>2</sub>O. In addition, the catalysts prepared with various reduction times (10, 13, and 16 h) and a constant concentration of reducing agent (ethylene glycol:H<sub>2</sub>O = 1:1) were denoted as 20Pt/C(M— $\beta$ ), where  $\beta$  represents the reduction time in hours. The 40 wt% Pt/C catalyst for the single-cell test was also prepared by the modified polyol reduction described above under the optimum reduction condition for the 20 wt% Pt/C catalyst to confirm the applicability.

The 40 wt% Pt/C catalyst prepared by the modified polyol reduction was denoted as 40Pt/C(M). For comparison, commercially available 20 wt% and 40 wt% Pt/C were used and denoted as 20Pt/C(C) and 40Pt/C(C), respectively.

### 2.2.2. Physical characterization

Structural characteristics of the prepared catalysts were investigated by XRD (D/MAX2500, Rigaku) using Cu K $\alpha$  radiation. The working voltage and current were maintained at 40 kV and 200 mA, respectively. The  $2\theta$  angular region between the  $20^\circ$  and  $90^\circ$  range was explored at a scan rate of  $2^\circ/\text{min}$ . The surface morphology of the Pt nanoparticles on the carbon support was studied with TEM (JEM-2000EX, JEOL) operated at 200 kV. Particle size distribution of the Pt nanoparticles was obtained by measuring the sizes of 300 Pt particles inside a TEM images. TGA measurements were done on a thermal analyzer (SDT Q-600, TA Instruments) at  $30 \sim 800^\circ\text{C}$  in an air flow (100 ml/min) using an alumina sample pan. The surface chemical state and binding energy of the catalyst were analyzed by X-ray photoelectron spectroscopy (XPS) (VGESCALAB 220i-XL, Fisons) at 450 W with a pass energy of 50 eV and using Mg K $\alpha$  radiation as the exciting source. The XPS spectra were calculated with respect to the Au  $4f_{7/2}$  core level (83.8 eV). The peak fitting of the XPS spectra was done with a Shirley function and Gaussian-Lorentzian function by the XPS PEAK 4.1 software.

### 2.2.3. Electrochemical activity

In the half-cell test, electrochemical measurements were done with a potentiostat (PC4/750, Gamry Instrument). The CV curve was observed in a conventional three-electrode cell using 3 mm diameter glassy carbon (010422, BASi) as a working electrode, Pt mesh (219810, Princeton Applied Research) as a counter electrode, and Ag/AgCl (MF-2052 RE-5B, BASi) as a reference electrode. The catalyst ink was prepared as follows: 10 mg of the catalyst was mixed with 5 wt% Nafion solution (1100 EW, Dupont) and isopropyl alcohol (Malinkrodt) with vigorous stirring. The weight ratio of catalyst to Nafion in the catalyst ink was 3:1. The catalyst ink was dropped onto the polished glassy carbon, and dried at room temperature. In the half-cell test, potentials were recorded with respect to the normal hydrogen electrode (NHE). Before the electrochemical measurement, all electrolytes were purged with N<sub>2</sub> gas for 20 min to remove any dissolved oxygen, and the potential was cycled between 0.0 and 1.2 V (vs. NHE) at 100 mV/s to remove any impurities from the Pt surface. The H<sub>2</sub> adsorption/desorption curves were done in 0.5 M H<sub>2</sub>SO<sub>4</sub> aqueous solution as an electrolyte with a scan rate of 20 mV/s at 25 °C. In the methanol oxidation reaction (MOR), 0.5 M H<sub>2</sub>SO<sub>4</sub> and 2 M CH<sub>3</sub>OH solution were used as electrolytes with a scan rate of 20 mV/s at 40 °C.

#### 2.2.4. Single-cell test

Activities of the 40 wt% Pt/C catalysts were evaluated using a single-cell of the polymer electrolyte membrane fuel cell (PEMFC). The membrane electrode assembly (MEA) was fabricated from a commercial membrane (Nafion 112, DuPont) according to the standard membrane cleaning procedure [69,70]. In order to prepare the MEA, the catalyst ink was sprayed on the membrane using the catalyst-coated membrane (CCM) method [71]. Electrochemical activity of the single-cell was carried out using the 40 wt% Pt/C catalysts as the cathode and the commercial 20 wt% Pt/C catalyst as the anode. The geometric electrode area of the single-cell was 5 cm<sup>2</sup> and the loading amount of Pt on the anode and cathode were both 0.15 mg/cm<sup>2</sup> to avoid interference from the membrane and anode. After the gas diffusion layers (TGPH-060, Toray Inc.) were placed on the anode and cathode sides of the membrane, the MEA was mounted in a single-cell with a graphite carbon plate. In this study, the operation temperature of the single-cell was fixed at 80 °C, and the flow rates of the feeding materials for the anode and cathode were fixed at 100 mL/min. Cyclic voltammetry experiment for the half-cell test was applied to the single-cell cathode to observe the relationship between the small-sized Pt particles and the enhanced EAS. In this experiment, N<sub>2</sub> was used as a cathode feeding material instead of O<sub>2</sub>, and H<sub>2</sub> was used as an anode feeding material. For the measurement of the H<sub>2</sub> adsorption/desorption curve, the potential was cycled between 0 and 1.2 V with a scan rate of 20 mV/s using a potentiostat (PGSTA302, Autolab). Single-cell performances were observed using the 40 wt% Pt/C catalysts as

the cathode and a commercial 20 wt% Pt/C catalyst as the anode. H<sub>2</sub> and air were used for the anode and cathode feeding materials, respectively. These gases were humidified in a bubbling humidifier before entering the fuel cell. The humidification temperatures for the anode and cathode gases were 80 and 67 °C, respectively. Each prepared single-cell performance was measured on a commercial fuel cell test station (SMART II PEM/DM Hybrid Fuel Cell Test System, WonATech Co.)

## **2.3. Results and discussion**

### **2.3.1. 20 wt% Pt/C catalyst characterization**

#### **2.3.1.1. Physical characterization**

The XRD patterns of the 20 wt% Pt/C catalysts synthesized by the modified polyol reduction with various concentrations of the reducing agent and a constant reduction time (10 h) are shown in Fig. 4. The diffraction peak at 25° is associated to the carbon (002) plane, and the peaks centered at about 40°, 46°, 68°, and 81° are attributed to the Pt (111), (200), (220), and (311) crystalline planes, respectively, corresponding to the face-centered cubic (fcc) structure of the crystalline Pt. This result shows that the Pt precursor was successfully reduced by the modified polyol reduction at 90 °C although the reduction temperature was much lower than that of the conventional polyol reduction at 160 °C. Based on the XRD results, the average

crystallite sizes were evaluated using the full width at half-maximum (FWHM) of the Lorentzian-fitted Pt (220) peaks by Scherrer's equation [72,73]. All the catalysts synthesized with different concentrations of the reducing agent had similar-sized Pt crystallites (1.3 nm) except for 20Pt/C(M—1:4), which had a 4.2 nm sized Pt crystallites. In the modified polyol reduction, ethylene glycol was used as both a solvent and a reducing agent. In addition, a unique property of polyol reduction is that the preparation method does not require stabilizers to produce small-sized metal nanoparticles since glycolate produced from the ethylene glycol oxidation interact with the metal nanoparticles and hence act as a stabilizer [66]. Therefore, the result shows that ethylene glycol in the modified polyol reduction could have a similar stabilizing effect on the Pt nanoparticles irrespective of the ethylene glycol concentration when the concentration of ethylene glycol stayed above 33 vol%. On the other hand, the catalyst prepared with low ethylene glycol concentration (<33 vol%) shows larger-sized Pt crystallite than the others. This result suggests that insufficient amount of stabilizer would not show sufficient stabilizing effect resulting in insufficient reduction of crystallite size. Ethylene glycol in the modified polyol reduction acts as a solvent as well as a reducing agent. Moreover, the ethylene glycol is related to the stabilizing effect on Pt nanoparticles because the stabilizer is glycolate produced from ethylene glycol. Crystallite growth is prevented by the interaction between stabilizer and Pt crystallite. On the other hand, H<sub>2</sub>O does not have stabilizing effect in the modified

polyol reduction [74]. Therefore, only the catalysts prepared with high ethylene glycol concentration did not show crystallite growth because the Pt surface was completely covered with stabilizer produced from a threshold or higher concentration of ethylene glycol.

Additional XRD analysis was done to observe the relationship between the reduction time and the particle size. The XRD patterns of 20 wt% Pt/C catalysts synthesized by the modified polyol reduction with various reduction times and a constant concentration of the reducing agent (ethylene glycol:H<sub>2</sub>O=1:1) are shown in Fig. 5. For comparison, the pattern of a commercial catalyst (20Pt/C(C)) is also shown in the same figure. All the catalysts including the commercial one exhibited typical diffraction peaks for the carbon and the fcc structured Pt crystallites. The diffraction peak of Pt became broader as the reduction time decreased, which indicates a decrease in the particle size. It was also observed that the intensity of the Pt (220) peak gradually diminished as the reduction time decreased. The disappearance of the Pt (220) peak for 20Pt/C(M—10) means that the crystallite size of Pt in this catalyst was much smaller than those of the others [75]. The resulting particle size obtained from the XRD results are shown in Table 2. Among the prepared catalysts, 20Pt/C(M—10) had the smallest sized Pt crystallite and its crystallite size was about 1.3 nm. In the polyol reduction, ethylene glycol oxidizes to glycolate, which has a stabilizing effect on the metal nanoparticles. However, the concentration of glycolate decreases in an

acid solution since the glycolate is changed to its protonated form in an acid solution [76]. Therefore, the change in crystallite size was believed to be related to the pH of the solution decreasing during the polyol reduction. In order to observe the influence of acidity on the crystallite size, the pH of each solution was observed before the filtration process and shown in Table 2. The acidity of the solution increased as the reduction time increased since the solution received more  $H^+$  from the ethylene glycol oxidation. Thus, a larger amount of ethylene glycol could be changed to glycolic acid and the stabilizing effect would be diminished. Among the various reduction conditions, the reduction condition of the 20Pt/C(M—10) was determined to be the optimum reduction condition (reduction temperature = 90 °C, ethylene glycol:H<sub>2</sub>O concentration = 1:1, and reduction time = 10 h) for the modified polyol reduction due to the smallest crystallite size.

Fig. 6 shows TEM images and the corresponding size distribution histograms of the commercial and the optimum 20 wt% Pt/C catalysts. TEM images (Fig. 6(a)) of the commercial catalyst shows partly large-sized Pt nanoparticles (4—6 nm) and particle agglomerations. The average size of Pt particles was around 2.4 nm. On the other hand, The Pt nanoparticles of the optimum catalyst were well dispersed on the carbon support without particle aggregation, and they had a narrow particle size distribution between 0.5 and 2.0 nm (Fig. 6(b)). The average Pt particle size measured from the TEM images was around 1.6 nm, which is very close to the Pt crystallite size

calculated from the XRD result. The similarity between the particle and crystallite sizes shows that most of the Pt nanoparticles existed as a single crystallite. Based on the XRD and TEM results, the 20Pt/C(M—10) catalyst has higher EAS and catalytic activity than the commercial catalyst as shown later.

#### 2.3.1.2. Electrochemical characterizations in a half-cell

In order to estimate the EAS of the prepared catalysts, a cyclic voltammetry experiment was carried out. The potential was cycled between 0 and 1.2 V (vs. NHE) at 20 mV/s in a 0.5 mol/L H<sub>2</sub>SO<sub>4</sub> aqueous solution purged with N<sub>2</sub> at 25 °C. In Fig. 7, all the catalysts exhibited well-defined H<sub>2</sub> adsorption/desorption peaks in the potential range of 0.0–0.3 V. From the integrated charge in the H<sub>2</sub> adsorption/desorption region, the EAS values of the catalysts can be calculated as suggested by Gasteiger *et al.* [77]. The observed EAS values are also summarized in Table 2. The EAS value of the 20Pt/C(M—10) was higher than those of the other catalysts including the commercial one. This improved EAS is attributed to the high Pt surface utilization by the highly dispersed Pt nanoparticles on the carbon support, as shown by the XRD result (Table 2). In addition, the higher EAS value of the smaller-sized Pt nanoparticles suggests that the surface of the small-sized Pt nanoparticles could be an active site for electrochemical reactions.

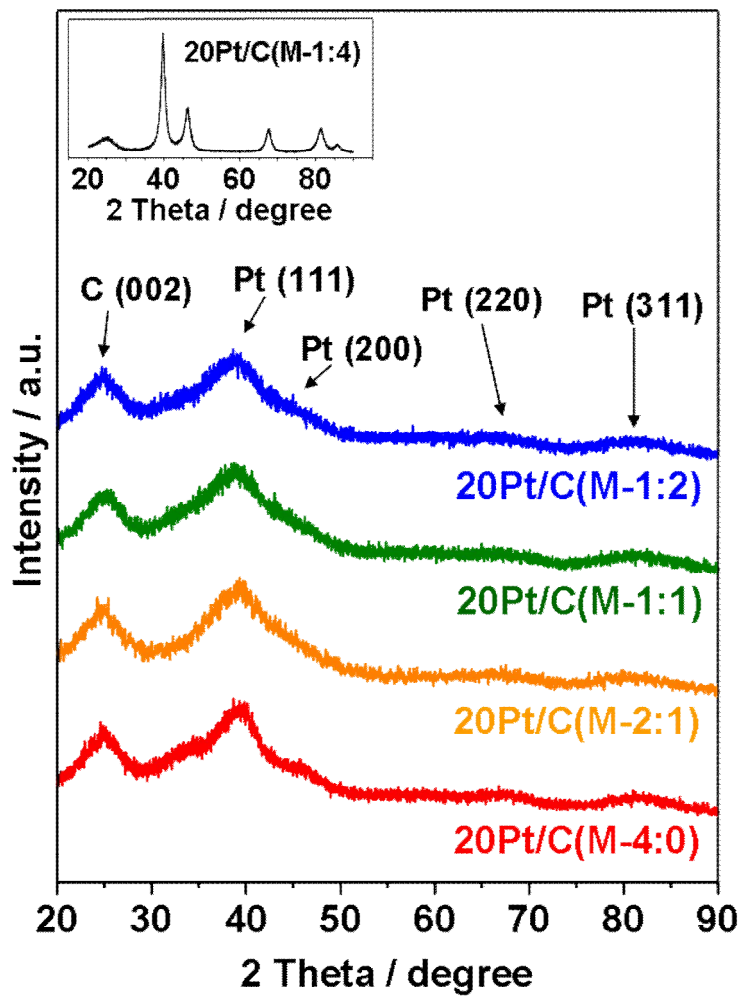


Fig. 4. X-ray diffraction patterns of 20 wt% Pt/C catalysts prepared by modified polyol reduction with various concentrations of reducing agent.

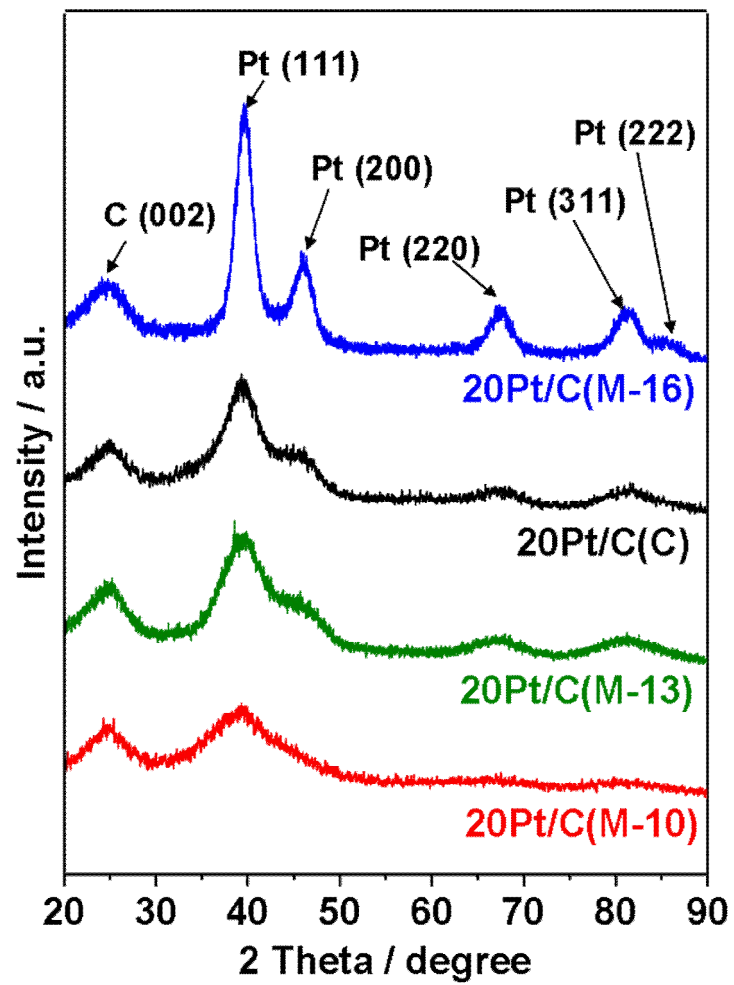


Fig. 5. X-ray diffraction patterns of 20 wt% Pt/C catalysts prepared by modified polyol reduction with various reduction times.

Table 2. The pH values after reduction process and the physical and electrochemical properties of the prepared 20 wt% Pt/C catalysts

Catalyst	pH of solution after reduction	Crystallite size of Pt / nm	Electrochemical activity	
			EAS / m <sup>2</sup> g <sub>Pt</sub> <sup>-1</sup>	MOR / mA mg <sub>Pt</sub> <sup>-1</sup>
20Pt/C(C)	-	1.9	69.2	185.1
20Pt/C(M-16)	4.2	4.2	10.1	37.8
20Pt/C(M-13)	6.1	1.8	68.9	183.5
20Pt/C(M-10)	7.8	1.2	76.7	228.8

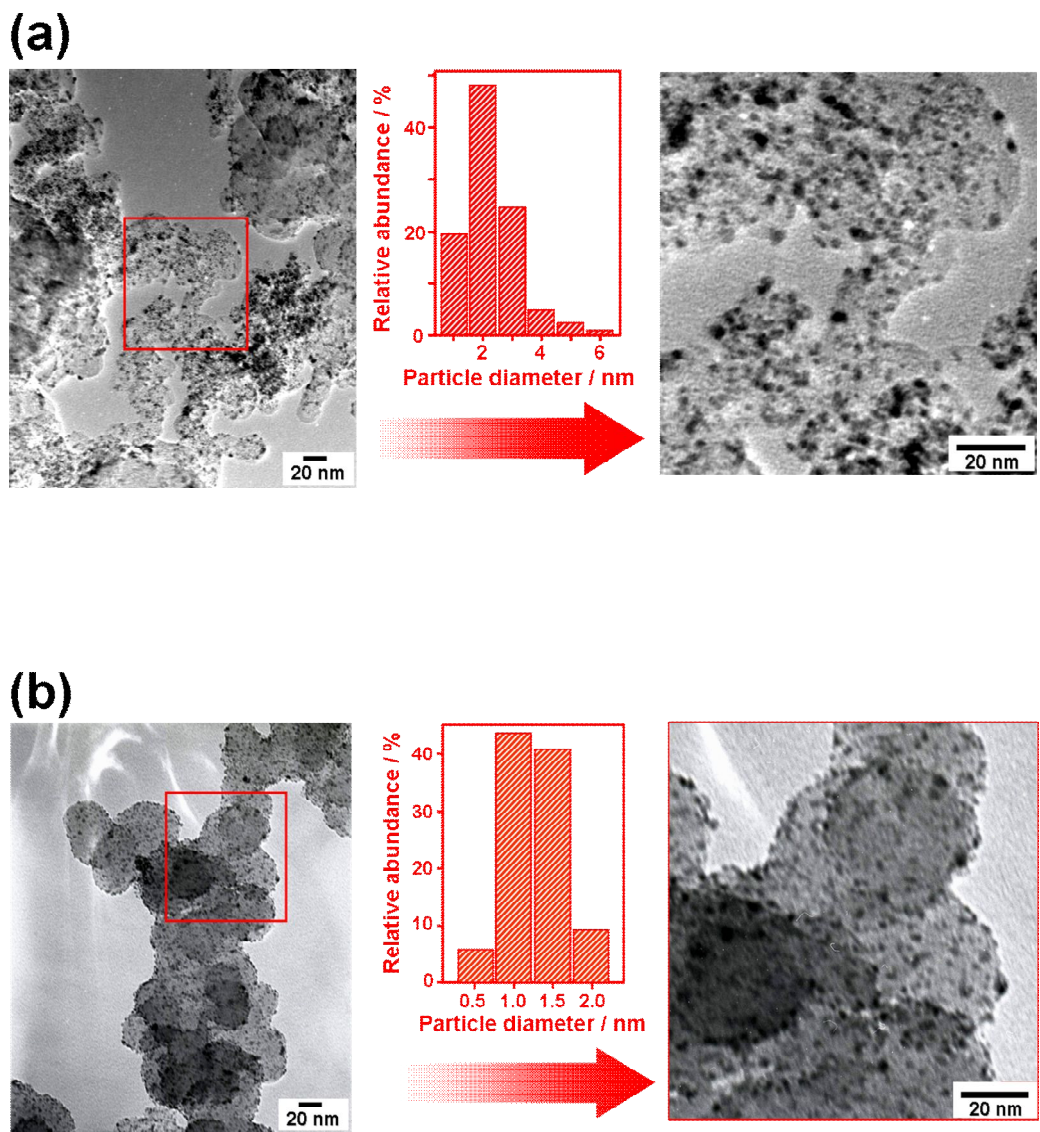


Fig. 6. TEM images and histograms of the particle size distribution of (a) 20Pt/C(C) and (b) 20Pt/C(M-10).

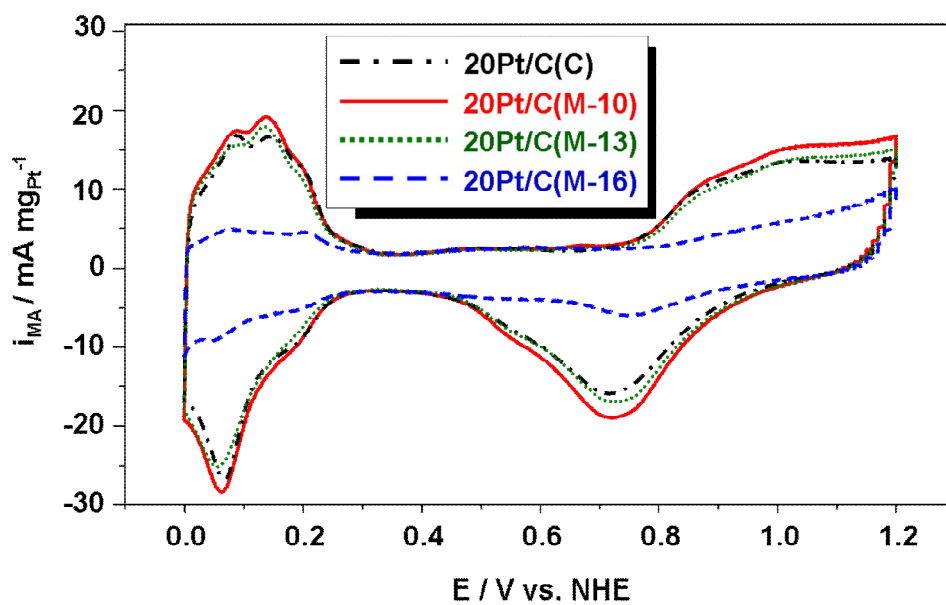


Fig. 7. Cyclic voltammograms for the prepared and the commercial 20 wt% Pt/C catalysts to observe the electrochemical active surface area.

In order to confirm the enhanced EAS, the electrochemical activities toward MOR were characterized using the CV experiment at 40 °C with a N<sub>2</sub>-purged mixed solution of 2 M CH<sub>3</sub>OH and 0.5 M H<sub>2</sub>SO<sub>4</sub> as the electrolyte. The current values were normalized by both the loading amount of Pt and the active surface area, considering that methanol adsorption and dehydrogenation occur only on the Pt surface [73,77]. As shown in Fig. 8(a), the order of activities for the mass-normalized MOR (229, 185, 184, and 38 mA/mg<sub>Pt</sub> for the 20Pt/C(M—10), 20Pt/C(C), 20Pt/C(M—13), and 20Pt/C(M—16) at 0.7 V, respectively) was same to that of the EAS. This result means that the enhanced EAS increases the MOR activity and shows that the catalyst prepared under the optimum reduction condition had a more extensive Pt surface than that of the other catalysts due to the smaller sized Pt nanoparticles.

In addition, all the catalyst had a very similar onset potential and activity for the area-normalized MOR shown in Fig. 85(b). It is well known that methanol dehydrogenation on a Pt surface produces CO as an intermediate. The CO is strongly adsorbed onto the Pt surface and blocks the continuous adsorption and dehydrogenation of methanol molecules [78—82]. When the potential increased in the CV experiment, the OH in the electrolyte was adsorbed on the Pt surface and transformed the adsorbed CO to CO<sub>2</sub>, releasing the Pt surface [82,83]. Thus, the similar onset potential and MOR activity means that the OH adsorption of each catalyst occurred at a similar potential. It has already been reported that the OH adsorption on a

Pt surface is related to the Pt d-band vacancy, i.e. electron density [84]. Therefore, it is believed that the onset potential for MOR would change if the preparation condition or particle size has an effect on the electron density of the Pt surface. The result of the area-normalized MOR activity suggests that the influence by the reduction condition on the electron density was negligible whereas EAS was greatly affected.

### 2.3.2. 40 wt% Pt/C catalyst characterization

#### 2.3.2.1 Physical characterization

In order to confirm the applicability of the single-cell, 40 wt% Pt/C catalysts were prepared. 40Pt/C(M) was prepared by the modified polyol reduction under the optimum reduction condition (reduction temperature = 90 °C, ethylene glycol:H<sub>2</sub>O concentration = 1:1, and reduction time = 10 h) for the 20 wt% Pt/C catalyst. For comparison, the 40Pt/C(P) was also prepared by the conventional polyol reduction [66,76]. Fig. 9 shows the XRD patterns for the commercial and prepared 40 wt% Pt/C catalysts. All the catalysts exhibited the typical diffraction peaks for the carbon and Pt crystallites. This shows that the platinum precursor was successfully reduced and the prepared Pt nanoparticles were well supported on the carbon. The average Pt crystallite sizes were calculated from the Pt (220) diffraction peaks by Scherrer's equation. The crystallite sizes of the Pt for the 40Pt/C(C), 40Pt/C(P), and 40Pt/C(M) were 2.8, 2.9 and 1.3 nm, respectively. TGA-DSC analysis was used to confirm the complete

reduction of the Pt precursor to Pt nanoparticles. For the 40Pt/C(M), 39.1 wt% components remained as residue after carbon combustion, which was the reduced Pt. The TGA result shows that the used preparation method could reduce most of the Pt precursor even though the amount of Pt precursor was increased by two times.

The TEM image of the 40Pt/C(M) catalyst is shown in Fig. 10. Highly dispersed Pt nanoparticles on the carbon support were also observed as in the 20 wt% Pt/C prepared under the optimum reduction condition. As shown in the histogram, the 40Pt/C(M) had a very narrow size distribution and the average particle size was estimated as 1.7 nm, which was also very close to the crystallite size from the XRD result.

Oxidation of nanoparticles differs substantially within the same process for planar metal single crystals or films at least in the dependence of the work function on the particle size [84]. Therefore, XPS analysis was used to observe the surface of the Pt nanoparticles prepared by the modified polyol reduction. Fig. 11(a) shows that XPS spectra of the Pt 4f for the 40Pt/C(M) after heat treatment in air at 160 °C for 24 h. The spectrum shows a doublet peak containing a low energy band (Pt 4f<sub>7/2</sub>) and a high energy band (Pt 4f<sub>5/2</sub>) at 71.1 and 74.4 eV, respectively. In order to identify the oxidation states of the Pt, the spectrum was deconvoluted into three pairs of overlapping curves, which can be assigned to Pt(0), Pt(II), and Pt(IV). The most

intense peak at 71.0 eV for Pt 4f<sub>7/2</sub> was assigned to the metallic Pt. The second peak, observed at a binding energy of 1.9 eV higher than that of the Pt(0), was assigned to the Pt(II) as in PtO or Pt(OH)<sub>2</sub>, and the third one corresponded to the Pt(IV) species [86]. The percentages of Pt(0), Pt(II), and Pt(IV) calculated from the relative intensity were 76.2, 18.9, and 4.9%, respectively. From this result, metallic Pt(0) was the predominant species in the catalyst (>75%) with a smaller amount of an oxidized platinum species (<25%). In the electrochemical reaction, the Pt(0) surface provides the active site for electrochemical reaction rather than the Pt(II) and Pt(IV) species [87]. In Fig. 8(b), Pt(0) peak for Pt 4f<sub>7/2</sub> at 71.0 eV with no change in binding energy, but the relative amounts of Pt(0), Pt(II), and Pt(IV) change to 78.3, 17.2, and 4.4%, respectively. In the comparison between 40Pt/C(M) and 40Pt/C(P), it was observed that small-sized Pt nanoparticle has more amount of oxidation state in the Pt surface than large-sized one because of the size effect as reported elsewhere [86]. Nevertheless, the ORR activity was higher in 40Pt/C(M) than 40Pt/C(P) due to much larger EAS of 40Pt/C(M). The size-dependent oxidation was reported by Han *et al.* and attributed slightly to the increased low-coordinated sites on smaller particles, which can bind more strongly with oxygen-containing species than terrace site [88]. It was also reported that the small-sized Pt nanoparticles show higher binding energy than large-sized Pt nanoparticles [89]. However, 40Pt/C(M) and 40Pt/C(P) showed deconvoluted peaks at similar binding energies although 40Pt/C(M) had smaller Pt nanoparticles than

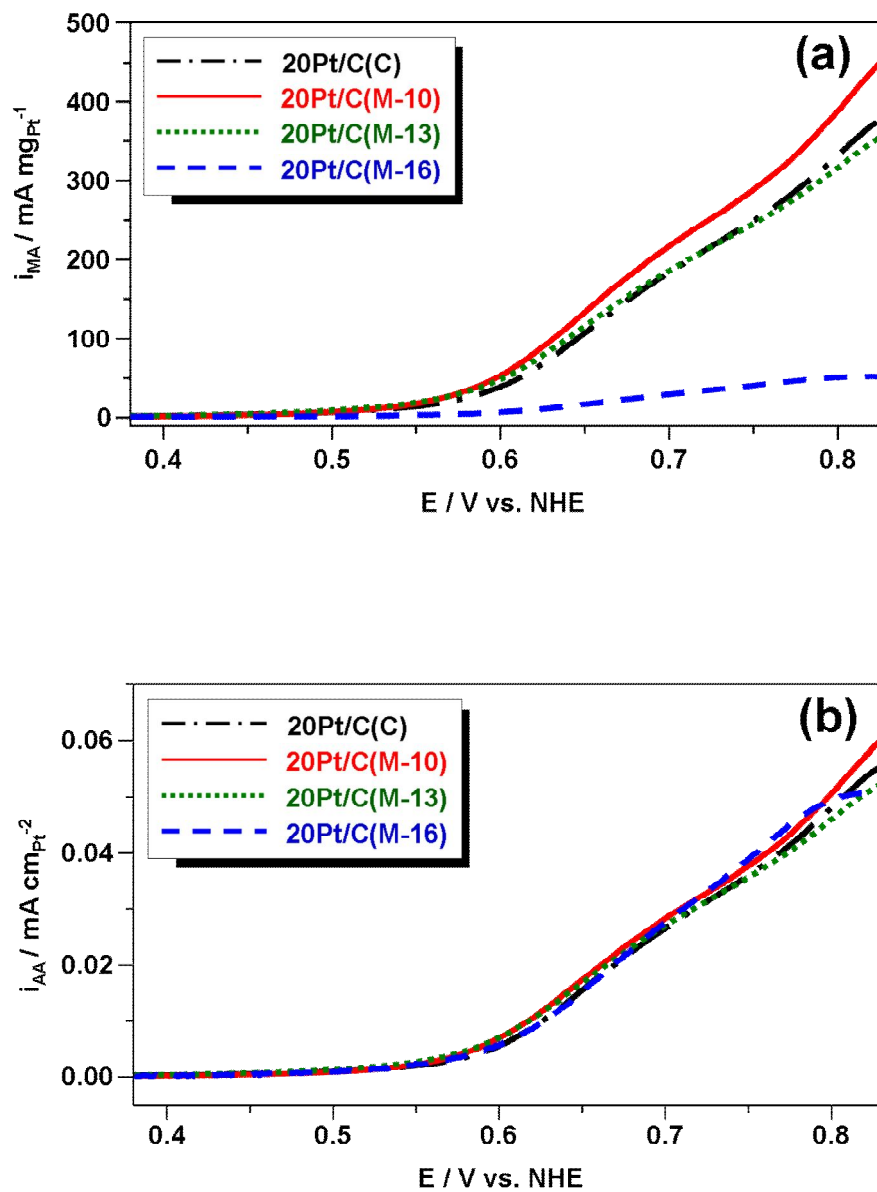


Fig. 8. (a) Mass-normalized and (b) area-normalized activity for methanol oxidation of the 20 wt% Pt/C catalysts.

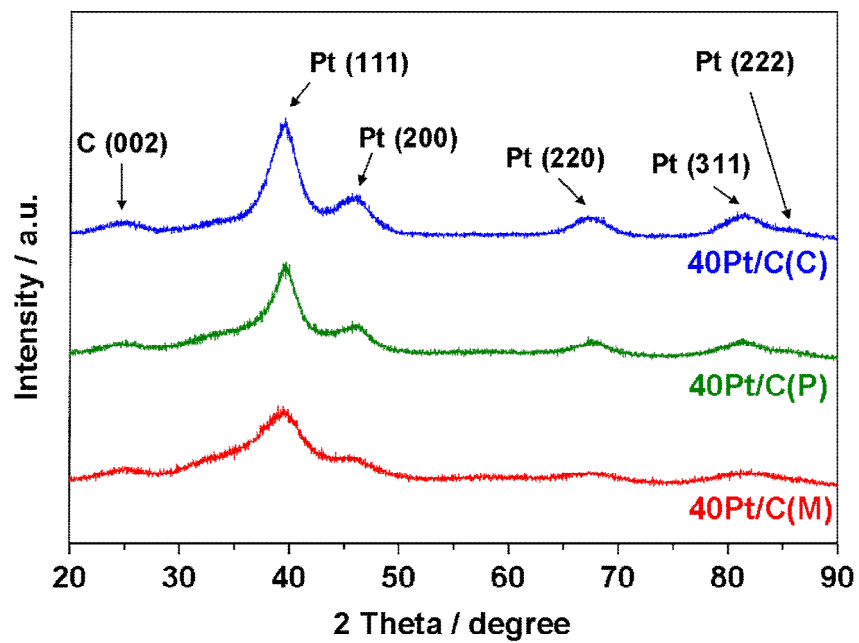


Fig. 9. X-ray diffraction patterns of the prepared and the commercial 40 wt% Pt/C catalysts.

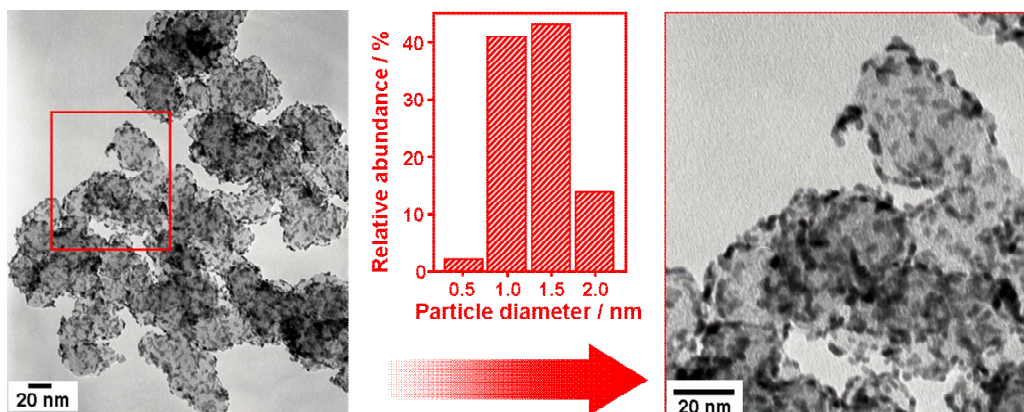


Fig. 10. TEM image and the corresponding size distribution diagram of the 40Pt/C(M).

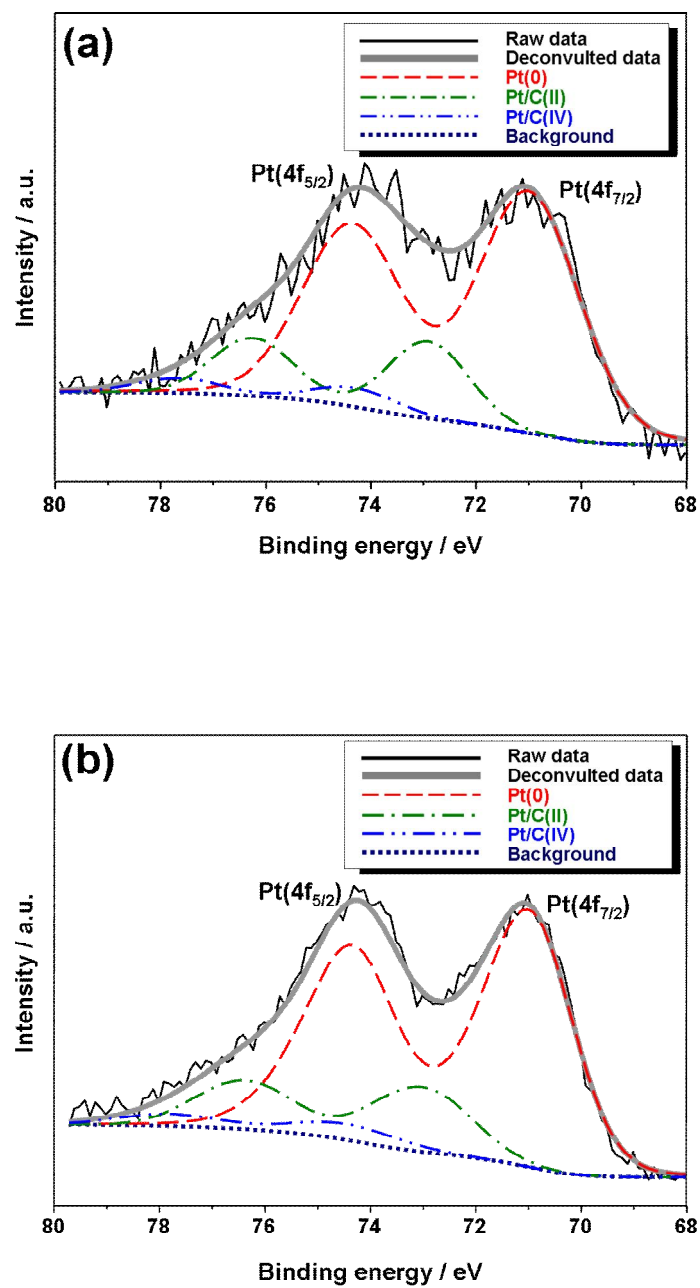


Fig. 11. XPS spectra of Pt 4f for (a) 40Pt/C(M) and (b) 40Pt/C(P).

40Pt/C(P). It suggests that there would be a threshold size difference which shows a detectable size effect, and that therefore no size effect is shown under the threshold size difference (about 1 nm) [90].

Based on the XRD, TGA, TEM, and XPS results, it was confirmed that the 40Pt/C(M) was successfully prepared by the modified polyol reduction without Pt loss and particle aggregation.

#### 2.3.2.2 Electrochemical characterization in a single-cell

The CV experiment for the half-cell test was applied to the single-cell system to confirm the EAS in an actual PEMFC. In the experiment, a modified single-cell system, which was very similar to the two electrode cell of the half-cell test, was designed. Humidified N<sub>2</sub> was used as a cathode feeding material instead of O<sub>2</sub>, and H<sub>2</sub> was used as an anode feeding material. A commercial 20 wt% Pt/C catalyst on the anode side could act as reference and counter electrodes, and Nafion membrane could act as an electrolyte. In this modified single-cell system, the anode of the fuel cell was connected to the potentiostat using the reference electrode and counter electrode cables, simultaneously. Thus, the cathode, which was connected to the working electrode cable, could be evaluated as a working electrode using a potentiostat. For comparison, the 40Pt/C(C) and 40Pt/C(P) catalysts were also evaluated under the same experiment conditions. In Fig. 12, all the catalysts exhibited well-defined H<sub>2</sub> adsorption/desorption

peaks at 0—0.3 V. Based on the H<sub>2</sub> adsorption/desorption peaks, the calculated EAS of the 40Pt/C(M) (23.0 m<sup>2</sup>/g) was higher than those of the 40Pt/C(P) (16.4 m<sup>2</sup>/g) and the 40Pt/C(C) (17.0 m<sup>2</sup>/g). This result shows that the highly dispersed Pt nanoparticles prepared by the modified polyol reduction not only enhanced the EAS in the half-cell test, but also increased the active sites in the single-cell system.

The performances of the PEMFC using the prepared and the commercial catalysts were evaluated as a cathode and shown in Fig. 13. All the catalysts had very similar open circuit voltages (OCV) and single-cell performance in the low current density region (0—300 mA/cm<sup>2</sup>). In the *I—V* curve, the current for ORR could be divided into the kinetic- and diffusion-controlling regions [91]. At the kinetic-controlling region (0.8—1.0 V), the electron density of the Pt nanoparticles is important in enhancing the ORR activity since the electron density affects the OH desorption potential. The OH adsorbed on the Pt surface inhibits the ORR, and this adsorbed OH is not derived from the reduction of O<sub>2</sub> but rather from the reaction between H<sub>2</sub>O and Pt [92]. On the other hand, mass-transfer can be neglected at the kinetic-controlling region because its effect on the current in the kinetic-controlling region was very small [93]. Therefore, a similar OCV and current in the kinetic-controlling region denotes that the small-sized Pt nanoparticles prepared by the modified polyol reduction did not have any effects on the electron density. The mass activity of the 40Pt/C(M) in the diffusion-controlling region (0.4—0.8 V) was higher

than that of the 40Pt/C(P) since the 40Pt/C(M) showed a lower polarization loss than that of the 40Pt/C(P). The measured current densities at 0.6 V for 40Pt/C(M) and 40Pt/C(P) were 678 and 630 mA/cm<sup>2</sup>, respectively. At the diffusion-controlling region (0.0—0.8 V), the ORR activity was affected by mass-transfer instead of the OH desorption because most of the OH adsorbed on Pt surface already desorbed by potential descent. In addition, the decrease of EAS increases mass-transfer resistances [94]. Therefore, the catalyst with higher EAS shows higher ORR activity in only the diffusion-controlling region because the catalyst prepared by the modified polyol reduction increases EAS of the single-cell without the influence on the electron density. This result is well matched to the mass- and area-normalized activity for the MOR activity in the half-cell test.

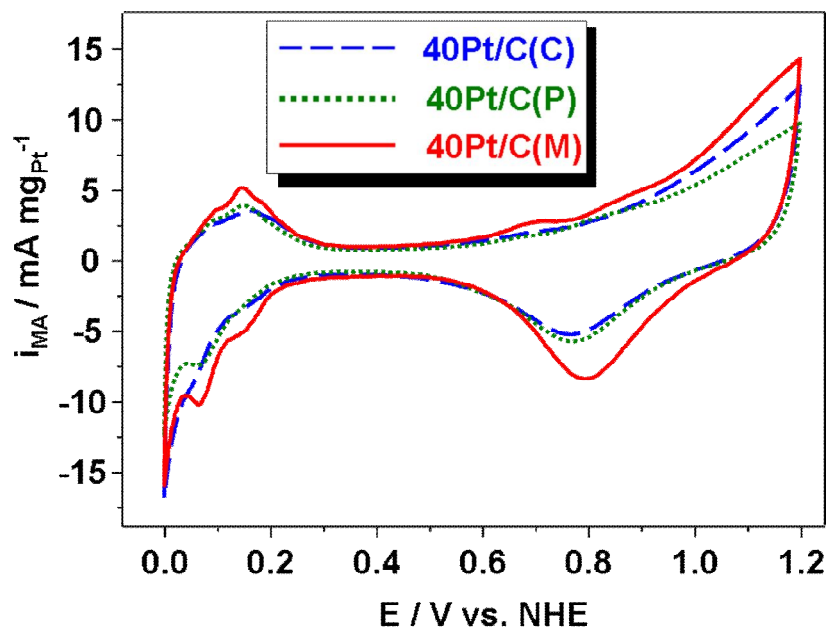


Fig. 12. Cyclic voltammograms of the prepared and the commercial 40 wt% Pt/C catalysts as a cathode of the PEMFC.

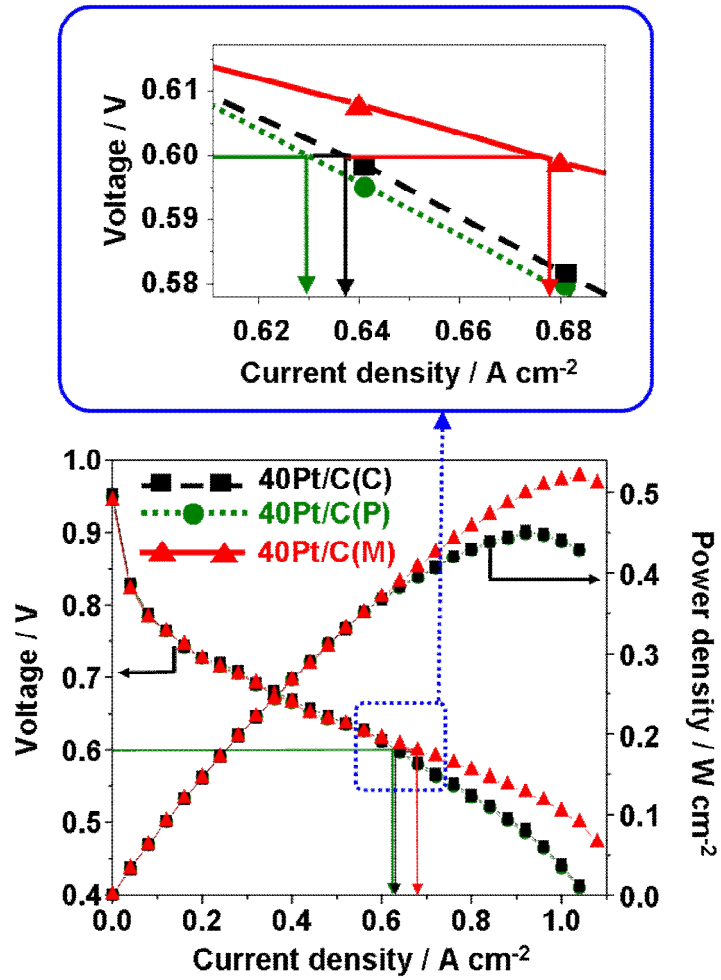


Fig. 13. Performances of the single-cell from PEMFCs using the prepared and the commercial 40 wt% Pt/C catalysts as a cathode.

## 2.4. Conclusions

Highly dispersed 20 wt% Pt/C catalysts with 1~4 nm size were successfully synthesized by the modified polyol reduction with different concentrations of a reducing agent and reduction time to control the size of Pt nanoparticles. TEM and XRD results revealed that the optimized 20 wt% Pt/C had very small-sized Pt nanoparticles (about 1.2 nm) with quite a narrow distribution between 0.5 and 2 nm. The optimized catalyst showed the highest EAS and MOR activity due to the highly dispersed Pt nanoparticles. In order to confirm the applicability of the preparation method for a single-cell catalyst, a 40 wt% Pt/C was synthesized using an optimum reduction condition (temperature = 90 °C, ethylene glycol:H<sub>2</sub>O concentration = 1:1, and reduction time = 10 h). The 40 wt% Pt/C synthesized by the modified polyol reduction had a higher EAS than a commercial catalyst in a single-cell system. In addition, the synthesized 40 wt% Pt/C catalyst had better single-cell performance than a commercial catalyst. The method used in this study provided an easy and reproducible procedure for the preparation of Pt nanoparticles supported on carbon.

## CHAPTER III

---

# Preparation and characterization of Pt/Ce<sub>0.5</sub>Zr<sub>0.5</sub>O<sub>2</sub>-C catalyst for ORR

### 3.1. Introduction

The most suitable electrocatalyst is Pt metal supported on carbon in the low-temperature fuel cell such as polymer electrolyte membrane fuel cell (PEMFC) and direct methanol fuel cell (DMFC). But Pt, which is expensive and restrictive, is not a very good catalyst for cathode material due to easy poison by strongly adsorbed OH. The hydrogen oxidation reaction (HOR) has low oxidation over potential due to ease of hydrogen oxidation and the kinetics limitation of the oxygen reduction reaction (ORR). Therefore, in low-temperature fuel cell, improving the catalytic activity for the ORR is crucial to increase overall fuel cell efficiency.

Two biggest issues on cathode catalyst for the last decade are as follows: one is the increase of active surface area for ORR to reduce the Pt loading. The other is development of Pt based alloy catalysts with transition metal to enhance ORR activity [94-108]. Although the former catalysts showed high methanol tolerance, their catalytic activities and stabilities were poor [109, 110]. The latter alloy catalysts

showed improved ORR activities of Pt-based alloy catalysts have been demonstrated by structural, ensemble, and electronic effects [97, 102, 111, 112]. Mukerjee *et al.* [97] and Jalan *et al.* [113] maintained that the increased catalytic activity of Pt-based alloy catalysts was related to the combination of electronic effect such as d-band vacancy and geometric effect such as shortening of Pt-Pt bond distance. Stamenkovic *et al.* [104] reported the activity enhancement for the ORR on 1Pt3Ni and 1Pt3Co alloy surfaces was correlated to the inhibition of Pt-OH<sub>ads</sub> formation on Pt sites surrounded by oxide covered Ni and Co atoms. Some other research groups have tried to improve the ORR activity of the Pt catalyst by mixing metal oxide such as WO<sub>3</sub> [114-115]. Among the tested metal oxides, CeO<sub>2</sub> seems to have an interesting property [116]. CeO<sub>2</sub> is a fluorite oxide whose cations can switch between +3 and +4 oxidation states and can be an oxygen buffer as CeO<sub>2</sub> can release oxygen reversibly [117, 118]. And also CeO<sub>2</sub> has demonstrated oxygen storage capability, promoted the water-gas shift reaction and stabilized the metal dispersion [119, 120]. The addition of CeO<sub>2</sub> to Pt/C catalyst for cathode electrode has been studied to our group to increase the local oxygen concentration. Our recent work has confirmed that the Pt/C catalyst physically mixed with nano-sized CeO<sub>2</sub> increased the local oxygen concentration in air atmosphere, leading to enhanced single-cell performance of direct methanol fuel cell [121]. Recently, it was reported that addition of Zr in CeO<sub>2</sub> increases the oxygen storage capacity of the CeO<sub>2</sub> and the thermal stability. The insertion of Zr into the

CeO<sub>2</sub> lattice distorts the oxygen sublattice, making mobile oxygen available for redox processes [122].

In this study, we tried to know the effect of Ce<sub>0.5</sub>Zr<sub>0.5</sub>O<sub>2</sub> addition using size-controlled Ce<sub>0.5</sub>Zr<sub>0.5</sub>O<sub>2</sub> nanoparticles. Pt/Ce<sub>0.5</sub>Zr<sub>0.5</sub>O<sub>2</sub>-C catalysts were synthesized by hydrothermal treatment and polyol reduction, and solvent and reaction time of the hydrothermal treatment were controlled to control the size of Ce<sub>0.5</sub>Zr<sub>0.5</sub>O<sub>2</sub>.

## **3.2. Experimental**

### **3.2.1. Preparation of Pt/Ce<sub>0.5</sub>Zr<sub>0.5</sub>O<sub>2</sub>-C**

The Pt/Ce<sub>0.5</sub>Zr<sub>0.5</sub>O<sub>2</sub>-C was prepared by hydrothermal treatment and conventional polyol reduction. The Pt/Ce<sub>0.5</sub>Zr<sub>0.5</sub>O<sub>2</sub>-C catalysts were prepared by continuous two steps in this study. First, nano-sized Ce<sub>0.5</sub>Zr<sub>0.5</sub>O<sub>2</sub> particles deposited on carbon support were prepared by hydrothermal treatment using CeCl<sub>3</sub>·7H<sub>2</sub>O (Aldrich) and ZrCl<sub>4</sub> (Aldrich) as precursors for Ce<sub>0.5</sub>Zr<sub>0.5</sub>O<sub>2</sub>. The preparation procedure was as follows; 0.0140 g of CeCl<sub>3</sub>·7H<sub>2</sub>O and 0.0087 g of ZrCl<sub>4</sub> were dissolved into 100 ml mixture of solvent (H<sub>2</sub>O and methyl alcohol) and 0.1 g of carbon black (Vulcan XC-72, Cabot Co.) in a Teflon bottle, then 5 M NaOH aqueous solution was slowly added until the pH reached to 11. The teflon bottle was held in a stainless steel vessel and tightly sealed. The temperature of hydrothermal treatment is 150 °C, and two kinds of reaction

time (3 or 13 h) were applied. After the hydrothermal treatment, the mixture was filtered, washed using distilled water, and dried in a vacuum oven for 24 h. 20 wt% Pt/Ce<sub>0.5</sub>Zr<sub>0.5</sub>O<sub>2</sub>-C catalysts were prepared by conventional polyol reduction. 1 g of chloroplatinic acid (H<sub>2</sub>PtCl<sub>6</sub>·6H<sub>2</sub>O, Kojima Chemicals) was dissolved in a 200 mL of ethylene glycol (Acros Organics). The solution (6.6 mL) was introduced to ethylene glycol (30 mL) with 0.05 g of prepared support. Subsequently, the mixture was refluxed at 160 °C with N<sub>2</sub> purging to remove the organic by-products and oxygen. After cooling to room temperature, a 3 M HCl (Matsunoen Chemicals) aqueous solution was added until the pH reached 2. After the polyol reduction, power could be obtained by filtration and drying procedures.

### 3.2.2. Physical characterization

Structural characteristics of the prepared catalysts were investigated by XRD (D/MAX2500, Rigaku) using Cu K $\alpha$  radiation. The working voltage and current were maintained at 40 kV and 200 mA, respectively. The 2 $\theta$  angular region between the 20° and 90° range was explored at a scan rate of 2°/min. The surface morphology of the Pt nanoparticles on the carbon support was studied with TEM (JEM-2000EX, JEOL) operated at 200 kV. Particle size distribution of the Pt nanoparticles was obtained by measuring the sizes of 300 Pt particles inside a TEM images. TGA measurements were done on a thermal analyzer (SDT Q-600, TA Instruments) at 30 ~ 800 °C in an air flow

(100 ml/min) using an alumina sample pan. TPR (BEL-CAT, BEL) was performed using a fixed bed tubular reactor unit equipped with thermal conductivity detector. A mixture gas of 5% H<sub>2</sub>/Ar with a flow of 25 ml/min was used to reduce the catalyst with raising the temperature from 25 to 1000 °C at 10 °C/min of heating rate.

### 3.2.3. Electrochemical activity

In the half-cell test, electrochemical measurements were done with a potentiostat (PC4/750, Gamry Instrument). The CV curve was observed in a conventional three-electrode cell using 3 mm diameter glassy carbon (010422, BASi) as a working electrode, Pt mesh (219810, Princeton Applied Research) as a counter electrode, and Ag/AgCl (MF-2052 RE-5B, BASi) as a reference electrode. The catalyst ink was prepared as follows: 10 mg of the catalyst was mixed with 5 wt% Nafion solution (1100 EW, Dupont) and isopropyl alcohol (Malinkrodt) with vigorous stirring. The weight ratio of catalyst to Nafion in the catalyst ink was 3:1. The catalyst ink was dropped onto the polished glassy carbon, and dried at room temperature. In the half-cell test, potentials were recorded with respect to the normal hydrogen electrode (NHE). Before the electrochemical measurement, all electrolytes were purged with N<sub>2</sub> gas for 20 min to remove any dissolved oxygen, and the potential was cycled between 0.0 and 1.2 V (vs. NHE) at 100 mV/s to remove any impurities from the Pt surface. The H<sub>2</sub> adsorption/desorption curves were done in 0.5 M H<sub>2</sub>SO<sub>4</sub> aqueous solution as an

electrolyte with a scan rate of 20 mV/s at 25 °C. The catalytic activity for ORR were measured with rotating disk electrode (RDE) (AFMSRX modulated speed rotator, Pine Instruments) installed with a glassy carbon (GC) RDE tips electrode (ARE3T050GC, Pine Instruments). A conventional three-electrode cell, in which reference, counter, and working electrodes were separated, was used for the ORR test for the catalysts in 1 M HClO<sub>4</sub> electrolyte solution.

### 3.3. Results and discussion

#### 3.3.1. 10 wt% Ce<sub>0.5</sub>Zr<sub>0.5</sub>O<sub>2</sub>-C support characterization

Fig. 14 shows the XRD patterns of Ce<sub>0.5</sub>Zr<sub>0.5</sub>O<sub>2</sub>/C powders synthesized by the modified hydrothermal treatment. Four diffraction peaks at 29.3°, 34.0°, 48.9°, and 58.0° were indentified as Ce<sub>0.5</sub>Zr<sub>0.5</sub>O<sub>2</sub> (101), Ce<sub>0.5</sub>Zr<sub>0.5</sub>O<sub>2</sub> (110), Ce<sub>0.5</sub>Zr<sub>0.5</sub>O<sub>2</sub> (221), and Ce<sub>0.5</sub>Zr<sub>0.5</sub>O<sub>2</sub> (211), respectively. The reaction condition and average crystallite size calculated from Ce<sub>0.5</sub>Zr<sub>0.5</sub>O<sub>2</sub> (101) by Scherrer's equation was shown in Table 3. In comparison between CZO-C-1 and CZO-C-2, crystallite size of Ce<sub>0.5</sub>Zr<sub>0.5</sub>O<sub>2</sub> increases with reaction time in hydrothermal treatment. In addition, the Ce<sub>0.5</sub>Zr<sub>0.5</sub>O<sub>2</sub> prepared in MeOH solvent showed smaller-sized crystallite than the Ce<sub>0.5</sub>Zr<sub>0.5</sub>O<sub>2</sub> prepared in H<sub>2</sub>O solvent because boiling point of MeOH is lower than H<sub>2</sub>O.

TEM images of CZO-C supports prepared by the hydrothermal treatment are presented in Fig. 15. Each support has different sized  $\text{Ce}_{0.5}\text{Zr}_{0.5}\text{O}_2$  nanoparticles, and CZO-C-1 among the prepared supports shows the largest-sized  $\text{Ce}_{0.5}\text{Zr}_{0.5}\text{O}_2$ . Particle sizes of the supports were, in a decreasing order: CZO-C-1 > CZO-C-2 > CZO-C-3. This result is well matched to the crystallite size calculated from XRD data. Considering the similar sizes estimated from XRD and TEM data, each crystallite seemed to form an individual particle.

### 3.3.2. 20 wt% Pt/ $\text{Ce}_{0.5}\text{Zr}_{0.5}\text{O}_2$ -C catalyst characterization

#### 3.3.2.1. Physical characterization

Fig. 16 shows the TGA data of the Pt- $\text{Ce}_{0.5}\text{Zr}_{0.5}\text{O}_2$ -C catalysts prepared by polyol reduction. Dramatic weight losses observed around between 400 and 450 °C were oxidation of carbon support. The combustion was completed at approximately 550 °C, leaving about 27 wt% components as residue in the catalysts which were due to the supported Pt and  $\text{Ce}_{0.5}\text{Zr}_{0.5}\text{O}_2$ . This result indicates that all of Pt and  $\text{Ce}_{0.5}\text{Zr}_{0.5}\text{O}_2$  were successfully loaded on the carbon support by the hydrothermal treatment and the polyol reduction because loading amounts of Pt and  $\text{Ce}_{0.5}\text{Zr}_{0.5}\text{O}_2$  were 20 wt% and 8 wt%, respectively. It is clear that our two kind of preparation method guarantees the complete preparation of Pt/ $\text{Ce}_{0.5}\text{Zr}_{0.5}\text{O}_2$ -C.

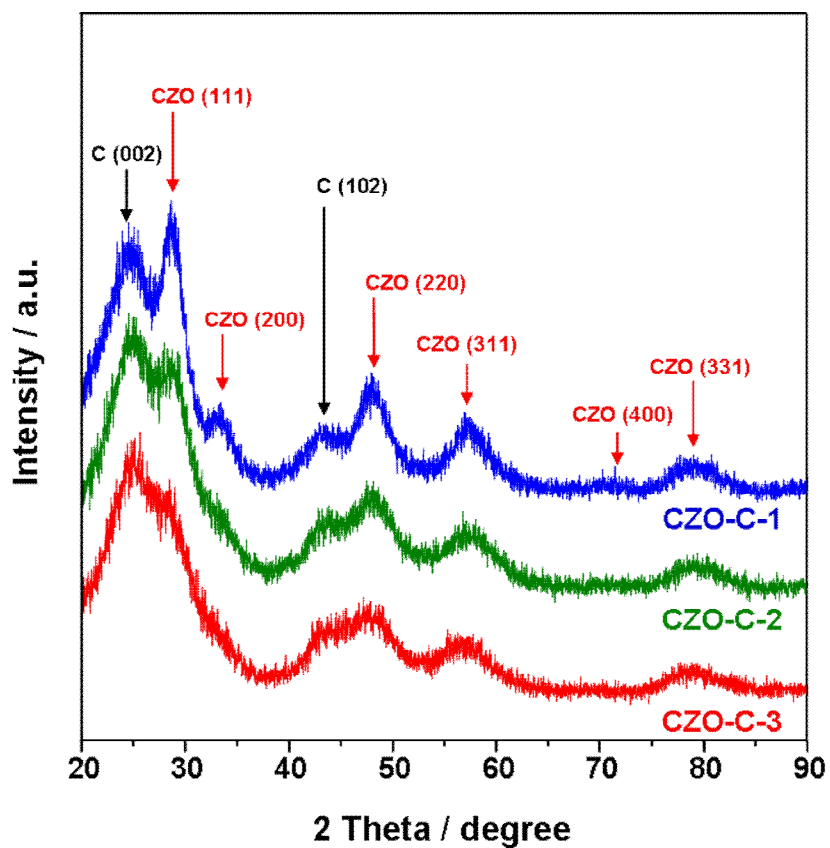


Fig. 14. X-ray diffraction patterns of CZO-C supports prepared by hydrothermal treatment.

Table 3. Condition of hydrothermal treatment and crystallite size calculated from XRD pattern

Support	Condition of hydrothermal treatment		Crystallite size of $\text{Ce}_{0.5}\text{Zr}_{0.5}\text{O}_2$ / nm
	Solvent	Time / h	
20Pt/10CZO-C-1	$\text{H}_2\text{O}$	13	3.1
20Pt/10CZO-C-2	$\text{H}_2\text{O}$	3	1.9
20Pt/10CZO-C-3	$\text{CH}_3\text{OH}$	3	1.4

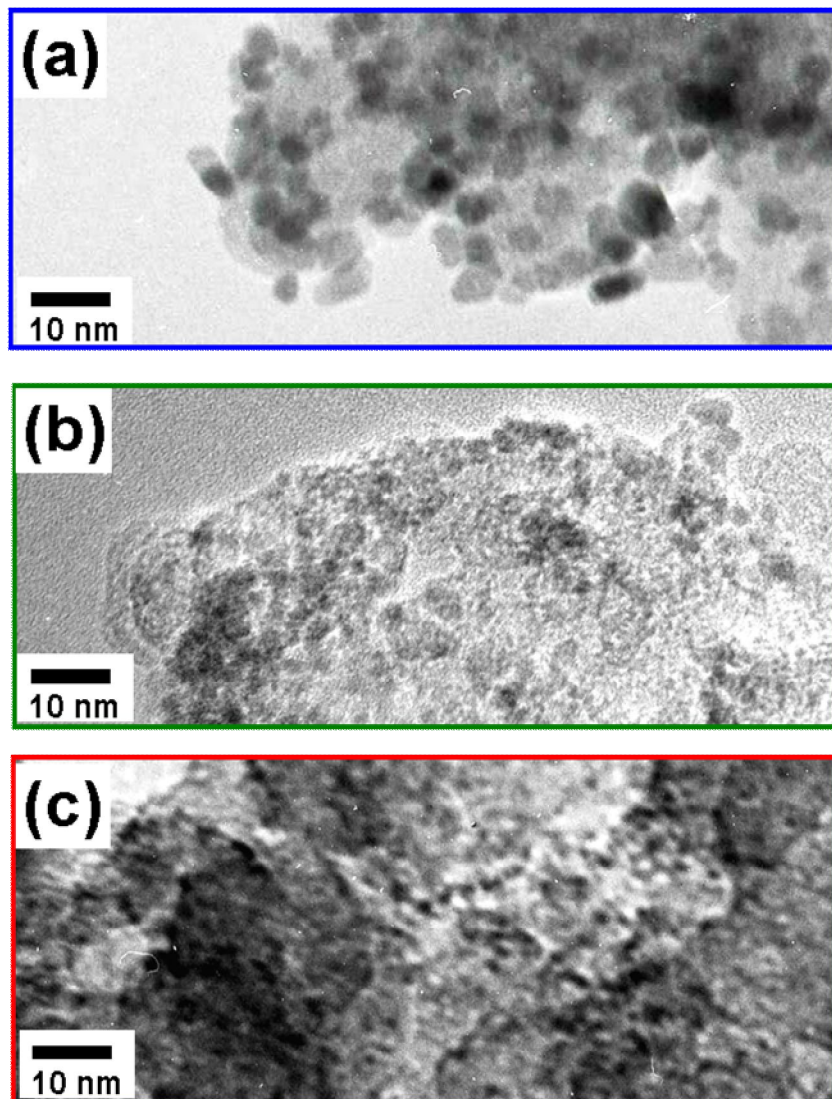


Fig. 15. TEM images of (a) CZO-C-1, (b) CZO-C-2, and (c) CZO-C-3.

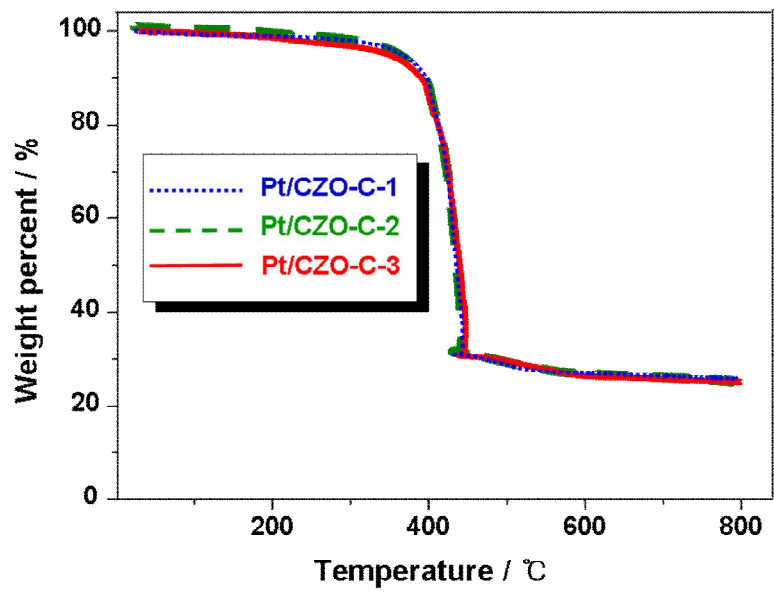


Fig. 16. TGA curves of Pt/CZO-C catalysts.

In order to observe addition effect of  $\text{Ce}_{0.5}\text{Zr}_{0.5}\text{O}_2$  on ORR activity, catalysts were prepared by polyol reduction using the  $\text{Ce}_{0.5}\text{Zr}_{0.5}\text{O}_2$  added carbon as a support. XRD data of the prepared catalysts were shown in Fig. 17. The peaks centered at about  $40^\circ$ ,  $46^\circ$ ,  $68^\circ$ , and  $81^\circ$  are attributed to the Pt (111), (200), (220), and (311) crystalline planes, respectively, corresponding to the face-centered cubic (fcc) structure of the crystalline Pt. This result shows that the Pt precursor was successfully reduced by the polyol reduction. Based on the XRD results, the average crystallite sizes were evaluated using the full width at half-maximum (FWHM) of the Lorentzian-fitted Pt (220) peaks by Scherrer's equation [72,73]. As shown in table 3, the solvent and treatment time in condition of hydrothermal treatment obviously affected the crystallite size of  $\text{Ce}_{0.5}\text{Zr}_{0.5}\text{O}_2$ , while the Pt crystallite shows similar-sized crystallite size. This result indicates that crystallite size of  $\text{Ce}_{0.5}\text{Zr}_{0.5}\text{O}_2$  was not changed during the polyol reduction, and particle size of  $\text{Ce}_{0.5}\text{Zr}_{0.5}\text{O}_2$  on carbon did not affect to the Pt nanoparticles prepared by polyol reduction. . It is generally known that Pt nanoparticles prepared by polyol reduction are not affected by a support because of stabilizing effect of glycolate. Pt nanoparticles covered with the glycolate can not contact to support.

In order to confirm the support effect on dispersion of Pt nanoparticles, TEM image of prepared catalyst including Pt/C catalyst prepared by polyol reduction were observed as shown in Fig. 18. All the catalysts showed that well-dispersed nanoparticles were on the carbon support, and difference in dispersion of nanoparticles

is not observed. Thus, it suggested that size of  $\text{Ce}_{0.5}\text{Zr}_{0.5}\text{O}_2$  also did not affect to the dispersion of Pt nanoparticles.

### 3.3.2.2. Electrochemical activity

The commercial and the prepared catalysts were evaluated in the RDE measurement as described in the experimental section to study the ORR kinetics. Fig. 19 shows voltammograms of the synthesized catalyst including the Pt/C catalyst prepared by polyol reduction and commercial Pt/C for ORR obtained at 20 °C in 1 M  $\text{HClO}_4$  aqueous solution saturated with oxygen using RDE at 2500 rpm. As shown in Fig. 20, all the  $\text{Ce}_{0.5}\text{Zr}_{0.5}\text{O}_2$ -added catalysts showed higher mass-normalized activity in the kinetic current region than synthesized and commercial Pt/C catalysts, indicating that the addition of  $\text{Ce}_{0.5}\text{Zr}_{0.5}\text{O}_2$  to Pt/C catalyst resulted in an improvement of ORR activity. Moreover, it was observed that the ORR activity increases with particle size of  $\text{Ce}_{0.5}\text{Zr}_{0.5}\text{O}_2$ . This result is also observed in the Tafel-plot (Fig. 21). All the  $\text{Ce}_{0.5}\text{Zr}_{0.5}\text{O}_2$  added catalysts showed higher kinetic currents than the Pt/C catalysts, and the catalyst hold the larger-sized  $\text{Ce}_{0.5}\text{Zr}_{0.5}\text{O}_2$  showed higher kinetic current for ORR.

It is generally known that the OH adsorbed on the Pt surface inhibits the ORR, and this adsorbed OH is not derived from the reduction of  $\text{O}_2$  but rather from the reaction between  $\text{H}_2\text{O}$  and Pt [92]. Therefore, relation between  $\text{Ce}_{0.5}\text{Zr}_{0.5}\text{O}_2$  addition and enhanced ORR activity could be observed in OH desorption of cyclic voltammetry

curve. Fig. 22 showed cyclic voltammetry curve in 0.5 M H<sub>2</sub>SO<sub>4</sub> electrolyte solution at 25 °C. In the potential region 0.6—0.8 V, the peaks of OH desorption which is the factor of evaluating how inhibitive of O<sub>2</sub> reduction were observed [123]. The peak of Pt/Ce<sub>0.5</sub>Zr<sub>0.5</sub>O<sub>2</sub>-C-1 was observed at the highest potential, and the order of peak potential is as follows: Pt/CZO-C-1 > Pt/CZO-C-2 > Pt/CZO-C-3 > Pt/C(S). The order of peak potential for OH<sub>ads</sub> desorption was well matched with the order of ORR activity. Therefore, it indicates that the addition of large-sized Ce<sub>0.5</sub>Zr<sub>0.5</sub>O<sub>2</sub> accelerates the OH<sub>ads</sub> desorption.

In order to understand correlation between OH<sub>ads</sub> desorption and Ce<sub>0.5</sub>Zr<sub>0.5</sub>O<sub>2</sub> addition, surface property of prepared catalysts were observed using FT-IR spectroscopy. In Fig. 23, singly-coordinated hydroxyl groups (type I) were observed at around 3700 cm<sup>-1</sup>. This peak is corresponding to the singly coordinated OH adsorbed on CeO<sub>2</sub>. On the other hand, doubly coordinated hydroxyl group (type II) which was generally observed at 3653 cm<sup>-1</sup> could not be observed because of OH<sub>ads</sub> on the carbon support. The Pt/C catalyst prepared by polyol reduction and carbon do not show the singly coordinated OH because they do not have Ce<sub>0.5</sub>Zr<sub>0.5</sub>O<sub>2</sub> nanoparticles. The amount of hydroxyl group was increased with increasing particle size of Ce<sub>0.5</sub>Zr<sub>0.5</sub>O<sub>2</sub> because large-sized Ce<sub>0.5</sub>Zr<sub>0.5</sub>O<sub>2</sub> had more Ce-rich phase on the surface than small-sized one. It was well matched to the activity data. Therefore, enhanced ORR activities of the Ce<sub>0.5</sub>Zr<sub>0.5</sub>O<sub>2</sub>-added catalysts were attributed to the decrease of OH coverage on Pt due to lateral repulsion between OH adsorbed on Pt and singly-coordinated OH on neighbor Ce<sub>0.5</sub>Zr<sub>0.5</sub>O<sub>2</sub>.

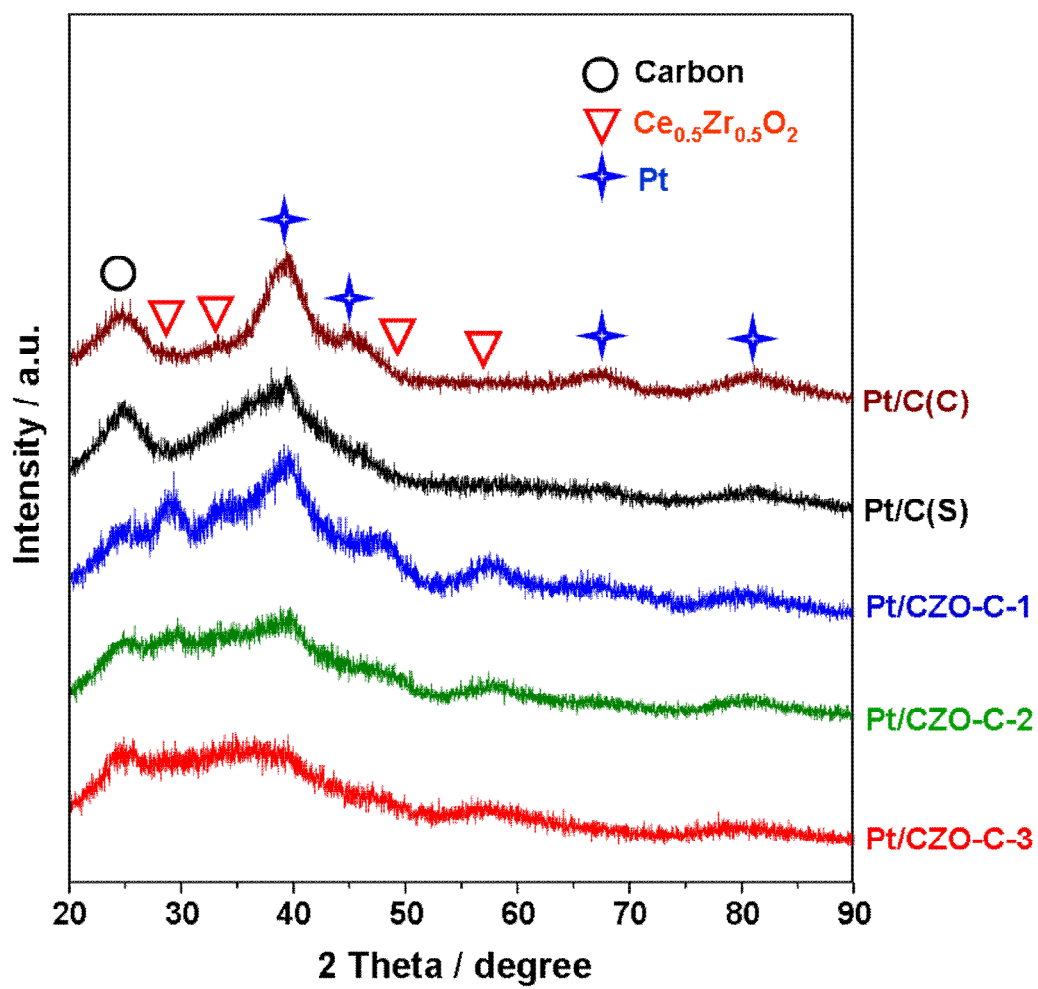


Fig. 17. X-ray diffraction patterns of Pt/CZO-C and Pt/C catalysts.

Table 4. Crystallite size of Pt/C and Pt/CZO-C catalysts

Catalyst	Crystallite size / nm	
	Pt	Ce <sub>0.5</sub> Zr <sub>0.5</sub> O <sub>2</sub>
Pt/CZO-C-1	1.4	3.1
Pt/CZO-C-2	1.3	2.3
Pt/CZO-C-3	1.3	1.7
Pt/C(S)	1.2	-

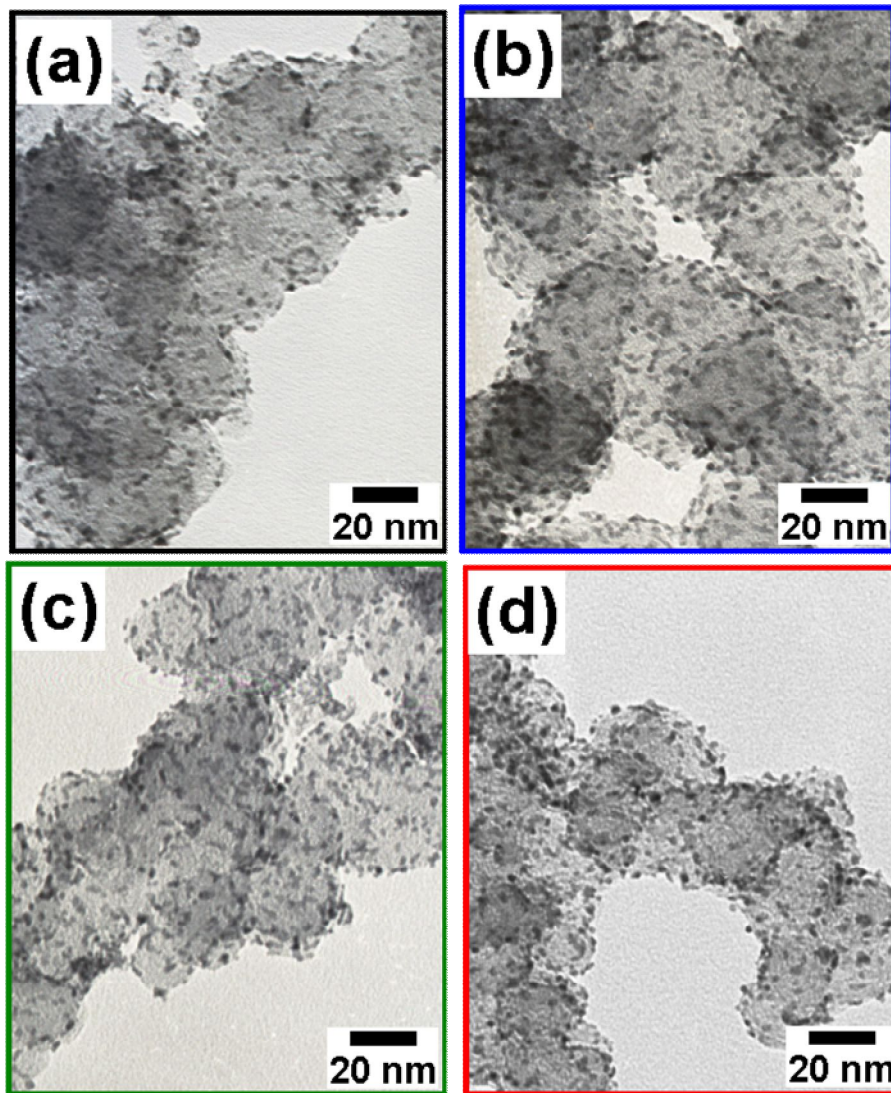


Fig. 18. TEM images of (a) Pt/C(S), (b) Pt/CZO-C-1, (c) Pt/CZO-C-2, and (d) Pt/CZO-C-3.

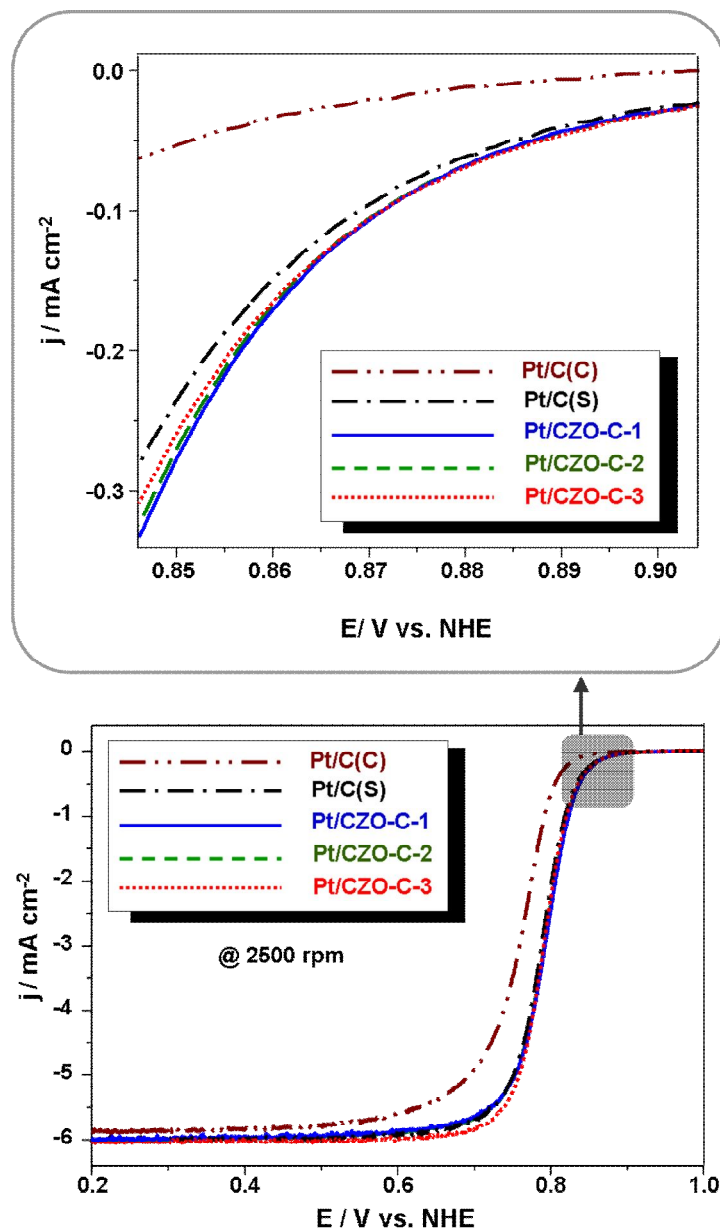


Fig. 19. Linear scan voltammograms of Pt/C and Pt/CZO-C catalysts in 1 M  $\text{HClO}_4$  saturated with pure oxygen at the scan rate of 1  $\text{mV/s}$  and with the rotating speed of 2500 rpm.

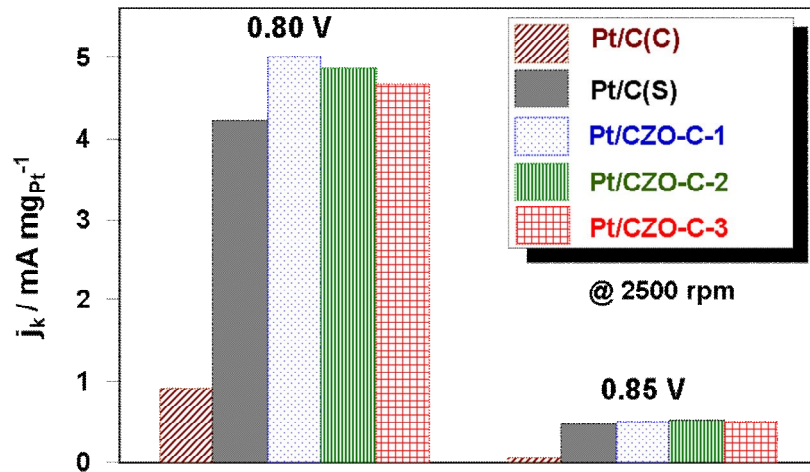


Fig. 20. Mass activities at 0.80 and 0.85 V for Pt/C and Pt/CZO-C catalysts.

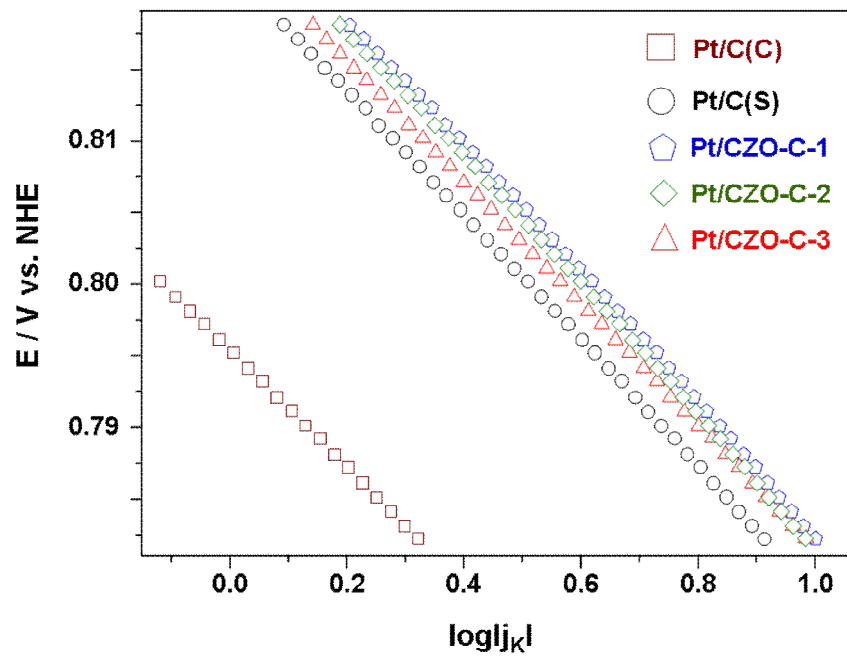


Fig. 21. Tafel plot for Pt/C and Pt/CZO-C catalysts.

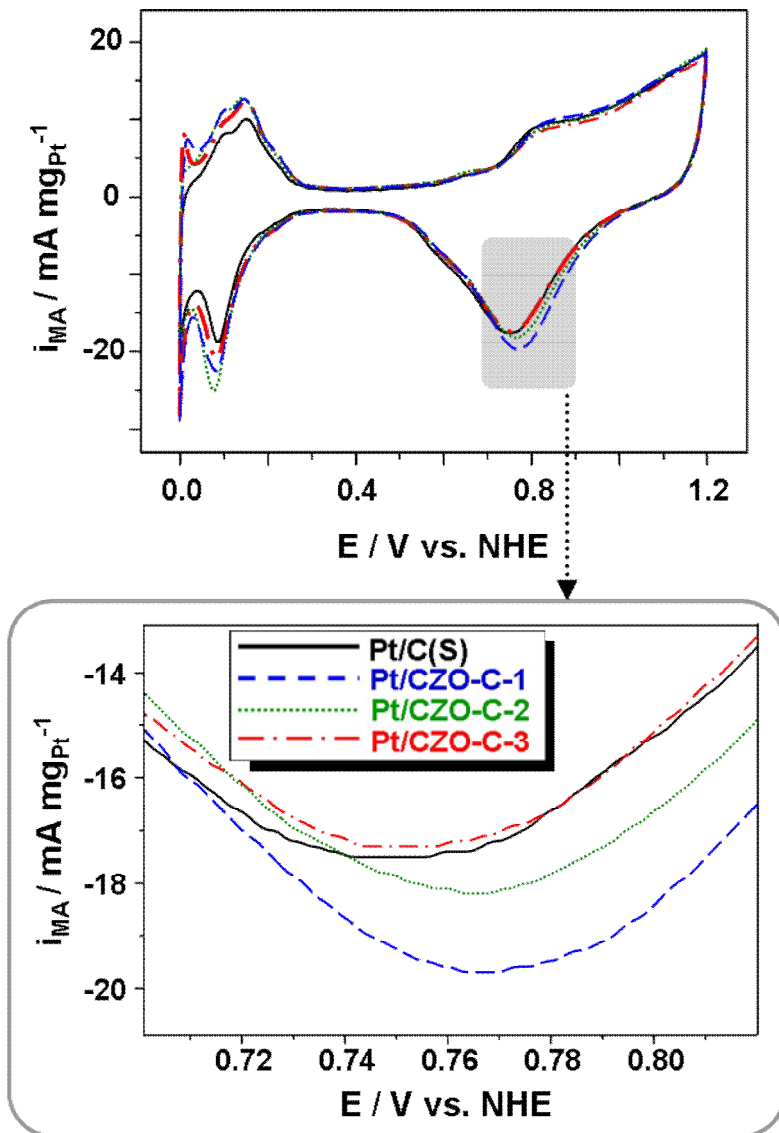


Fig. 22. Cyclic voltammograms of the Pt/C and Pt/CZO-C catalysts in 0.5 M H<sub>2</sub>SO<sub>4</sub> at the scan rate of 20 mV/s.

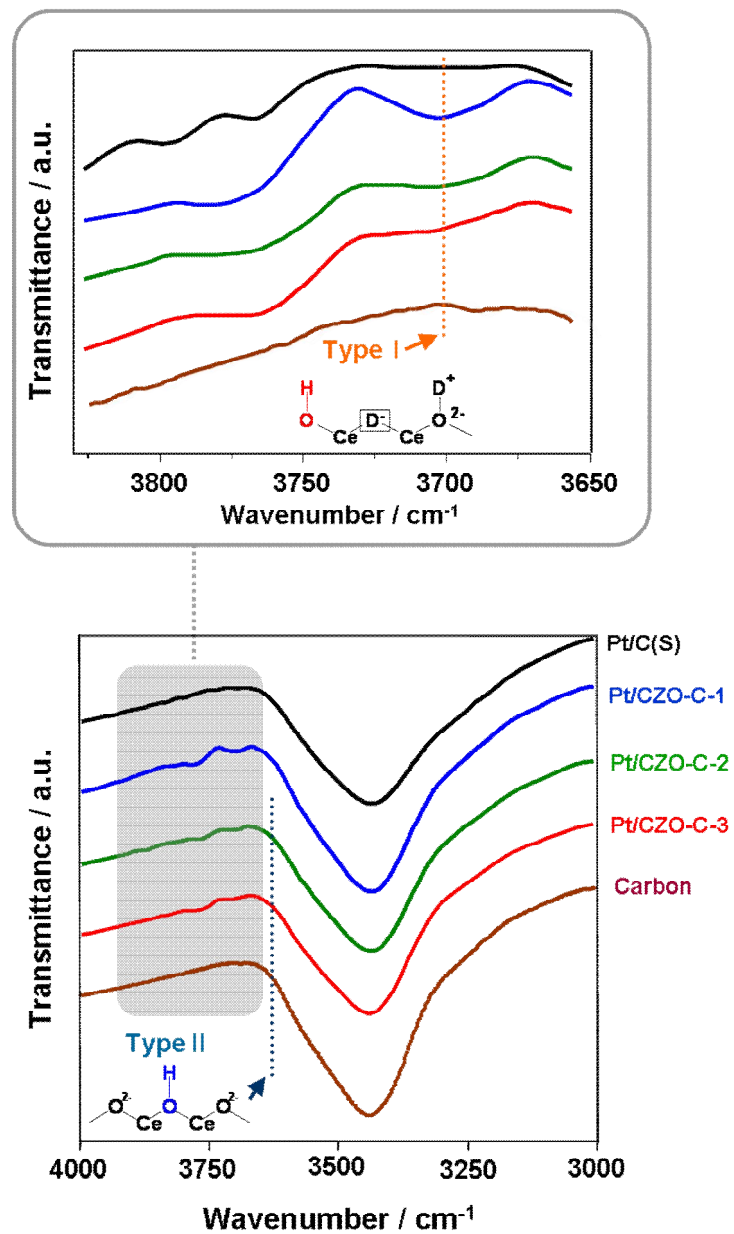


Fig. 23. IR spectroscopy of Pt/C and Pt/CZO-C catalysts.

### 3.4. Conclusions

Highly dispersed Pt and  $\text{Ce}_{0.5}\text{Zr}_{0.5}\text{O}_2$  nanoparticles were successfully prepared via ethylene glycol reduction and hydrothermal treatment using a commercial carbon as support, respectively. In the hydrothermal treatment, the size of  $\text{Ce}_{0.5}\text{Zr}_{0.5}\text{O}_2$  was affected by solvent and reaction time. However, the size difference of  $\text{Ce}_{0.5}\text{Zr}_{0.5}\text{O}_2$  did not affect the particle size and the dispersion of Pt. The XRD pattern of the Pt/ $\text{Ce}_{0.5}\text{Zr}_{0.5}\text{O}_2$ -C catalyst showed the peaks of Pt and  $\text{Ce}_{0.5}\text{Zr}_{0.5}\text{O}_2$  crystallites giving no shift of the position of Pt diffraction peak. This indicates that the addition of  $\text{Ce}_{0.5}\text{Zr}_{0.5}\text{O}_2$  did not affect the crystallite of Pt. The TEM images of the Pt catalysts having different  $\text{Ce}_{0.5}\text{Zr}_{0.5}\text{O}_2$  particles also showed well-dispersed Pt and  $\text{Ce}_{0.5}\text{Zr}_{0.5}\text{O}_2$  nanoparticles without any change of Pt nanoparticle dispersion. On the other hand, the presence of  $\text{Ce}_{0.5}\text{Zr}_{0.5}\text{O}_2$  nanoparticles increased the activity of Pt for ORR. Among the prepared  $\text{Ce}_{0.5}\text{Zr}_{0.5}\text{O}_2$  nanoparticles, the catalyst having large-sized  $\text{Ce}_{0.5}\text{Zr}_{0.5}\text{O}_2$  showed higher ORR activity because large-sized  $\text{Ce}_{0.5}\text{Zr}_{0.5}\text{O}_2$  had more Ce-rich phase on the surface than small-sized one, at which the coordinated hydroxyl groups formed more during ethylene glycol reduction. The enhanced ORR activity was attributed to the decrease of OH coverage on Pt due to the lateral repulsion between OH adsorbed on Pt and OH coordinated on neighbor  $\text{Ce}_{0.5}\text{Zr}_{0.5}\text{O}_2$ .

## CHAPTER IV

---

---

# Development of core-shell typed PtPd/C catalyst for ORR in PEMFC by polyol reduction

### 4.1 Introduction

In the last decades, Pt-based catalysts have attracted a great deal of attention due to their promising application, particularly as the electrode catalyst for low-temperature fuel cell and considerable progress were achieved [95, 109]. Although Pt-based catalyst have excellent electrocatalytic activity in both methanol oxidation and oxygen reduction, some obstacles still remain for the commercialization of fuel cell, such as the high cost of Pt and the reduction of the cell performance that originates from the mixed potential by liquid fuel crossover from anode to cathode. Consequently, the major issues facing low temperature fuel cells are cost-down of electrode and finding a new selective oxygen reduction catalyst on cathode electrode. Therefore, many research groups have attempted to develop new low-cost electrocatalyst that could reduce expensive Pt-based catalysts.

Recently, two approaches have been extensively investigated to reduce Pt cost in fuel cells: one is the increase of active surface area for ORR to reduce the Pt loading.

The other is development of Pt based alloy catalysts with transition metal to enhance ORR activity [94-108]. Although the former catalysts showed high methanol tolerance, their catalytic activities and stabilities were poor [109, 110]. The latter alloy catalysts showed improved ORR activities of Pt-based alloy catalysts have been demonstrated by structural, ensemble, and electronic effects [97, 102, 111, 112]. Mukerjee *et al.* [97] and Jalan *et al.* [113] maintained that the increased catalytic activity of Pt-based alloy catalysts was related to the combination of electronic effect such as d-band vacancy and geometric effect such as shortening of Pt-Pt bond distance. Stamenkovic *et al.* [104] reported the activity enhancement for the ORR on 1Pt3Ni and 1Pt3Co alloy surfaces was correlated to the inhibition of Pt-OH<sub>ads</sub> formation on Pt sites surrounded by oxide covered Ni and Co atoms. However, the alloy nanoparticles showed a decrease of electroactive surface area (EAS) because alloy nanoparticles had larger particle size than Pt nanoparticles.

In order to solve these problems, core-shell typed PtPd nanoparticles were prepared. In this research, 3Pt1Pd nanoparticles were prepared because Pt<sub>3</sub>Pd<sub>1</sub> is known as a best material to enhance ORR activity [93]. The prepared core-shell typed PtPd nanoparticle on carbon support has Pt-riched core and Pd shell. Therefore, the core-shell typed nanoparticles could show small-sized nanoparticle and enhanced ORR activity, simultaneously.

## 4.2. Experimental

### 4.2.1. Preparation of PtPd/C

Pt/C, Pd/C, and PtPd/C were prepared by conventional polyol reduction with pH control. The metal loading amount of PtPd/C was fixed at 20 wt%. 1 g of  $\text{H}_2\text{PtCl}_6 \cdot 6\text{H}_2\text{O}$  (Kojima Chemicals) and  $\text{PdCl}_2$  were dissolved in 200 mL of ethylene glycol (Acros Organics). The solution was introduced to ethylene glycol (30 mL) with 0.05 g of carbon support. To control the pH of the mixture, 2.5 M NaOH (Daejung Chemicals and Metals) solution was added. Subsequently, the mixture was refluxed at 160 °C for 3 h in an oil bath with  $\text{N}_2$  purging to remove the organic by-products and oxygen. After cooling to room temperature, a 3 M HCl (Matsunoen Chemicals) aqueous solution was added to mixture in order to lower the pH to 2. After the polyol reduction, powder could be obtained by filtration and drying procedures. Finally, the dried powder was heat-treated in air at 160 °C for 24 h to completely remove the solvent, which negatively affects the catalytic activity. The Prepared 20 wt% Pt/C, 20 wt% Pd/C, and 20 wt% PtPd/C catalysts was denoted to Pt/C(x), Pd/C(x), and PtPd/C(x), respectively, where x represents the concentration of NaOH.

### 4.2.2. Physical characterization

Structural characteristics of the prepared catalysts were investigated by XRD (D/MAX2500, Rigaku) using Cu K $\alpha$  radiation. The working voltage and current were maintained at 40 kV and 200 mA, respectively. The  $2\theta$  angular region between the  $20^\circ$  and  $90^\circ$  range was explored at a scan rate of  $2^\circ/\text{min}$ . The surface morphology of the Pt nanoparticles on the carbon support was studied with TEM (JEM-2000EX, JEOL) operated at 200 kV. Particle size distribution of the Pt nanoparticles was obtained by measuring the sizes of 300 Pt particles inside a TEM images. TGA measurements were done on a thermal analyzer (SDT Q-600, TA Instruments) at  $30 \sim 800^\circ\text{C}$  in an air flow (100 ml/min) using an alumina sample pan. TPR (BEL-CAT, BEL) was performed using a fixed bed tubular reactor unit equipped with thermal conductivity detector. A mixture gas of 5% H<sub>2</sub>/Ar with a flow of 25 ml/min was used to reduce the catalyst with raising the temperature from 25 to  $1000^\circ\text{C}$  at  $10^\circ\text{C}/\text{min}$  of heating rate.

#### 4.2.3 Electrochemical activity

In the half-cell test, electrochemical measurements were done with a potentiostat (PC4/750, Gamry Instrument). The CV curve was observed in a conventional three-electrode cell using 3 mm diameter glassy carbon (010422, BASi) as a working electrode, Pt mesh (219810, Princeton Applied Research) as a counter electrode, and Ag/AgCl (MF-2052 RE-5B, BASi) as a reference electrode. The catalyst ink was prepared as follows: 10 mg of the catalyst was mixed with 5 wt% Nafion solution

(1100 EW, Dupont) and isopropyl alcohol (Malinkrodt) with vigorous stirring. The weight ratio of catalyst to Nafion in the catalyst ink was 3:1. The catalyst ink was dropped onto the polished glassy carbon, and dried at room temperature. In the half-cell test, potentials were recorded with respect to the normal hydrogen electrode (NHE). Before the electrochemical measurement, all electrolytes were purged with N<sub>2</sub> gas for 20 min to remove any dissolved oxygen, and the potential was cycled between 0.0 and 1.2 V (vs. NHE) at 100 mV/s to remove any impurities from the Pt surface. The H<sub>2</sub> adsorption/desorption curves were done in 0.5 M H<sub>2</sub>SO<sub>4</sub> aqueous solution as an electrolyte with a scan rate of 20 mV/s at 25 °C. The catalytic activity for ORR were measured with rotating disk electrode (RDE) (AFMSRX modulated speed rotator, Pine Instruments) installed with a glassy carbon (GC) RDE tips electrode (ARE3T050GC, Pine Instruments). A conventional three-electrode cell, in which reference, counter, and working electrodes were separated, was used for the ORR test for the catalysts in 1 M HClO<sub>4</sub> electrolyte solution.

### **4.3. Results and Discussion**

#### 4.3.1. 3Pt1Pd/C catalyst characterization

##### 4.3.1.1. Physical characterization

In the polyol reduction, acidity of solution is very important to prepare metal nanoparticles because the acidity affect to the concentration of glycolate which has a stabilizing effect on metal nanoparticles. Moreover, acidity of solution also affect to the preparation of metal salt. Especially, transition metals such as Pd, Co, Fe, and Ni can be easily changed to metal hydroxide. Therefore, relation between concentration of NaOH and pH of solution was observed (Fig. 24).

Fig. 25 shows the XRD data of Pt/C catalysts prepared with the pH control and the relation between crystallite size and concentration of NaOH. The diffraction peak at  $25^\circ$  is associated to the carbon (002) plane, and the peaks centered at about  $40^\circ$ ,  $46^\circ$ ,  $68^\circ$ , and  $81^\circ$  are attributed to the Pt (111), (200), (220), and (311) crystalline planes, respectively, corresponding to the face-centered cubic (fcc) structure of the crystalline Pt. This result shows that the Pt precursor was successfully reduced by the polyol reduction. Based on the XRD results, the average crystallite sizes were evaluated using the full width at half-maximum (FWHM) of the Lorentzian-fitted Pt (220) peaks by Scherrer's equation [72,73]. As shown in Fig. 25(b), the catalyst prepared by polyol reduction on low concentration of NaOH ( $C_{\text{NaOH}} < 15 \mu\text{M}$ ) showed large-sized metal crystallite due to the absence of glycolate which has stabilizer effect on the metal nanoparticles. In the polyol reduction, ethylene glycol oxidizes to glycolate, which has a stabilizing effect on the metal nanoparticles. However, the concentration of glycolate decreases in an acid solution since the glycolate is changed to its protonated form in an acid solution [76]. On the other hand, all the catalyst prepared by polyol reduction on

high concentration of NaOH ( $C_{\text{NaOH}} > 15 \mu\text{M}$ ) showed similar crystallite size because of enough stabilizer.

XRD data of Pd/C catalysts prepared with the pH control and the relation between crystallite size and concentration of NaOH is shown in Fig. 26. In Fig. 26(a), the peaks at about  $40^\circ$ ,  $46^\circ$ ,  $68^\circ$ , and  $81^\circ$  are corresponding to the Pd (111), (200), (220), and (311) crystalline planes, respectively. The Pd/C prepared by polyol reduction on very low concentration of NaOH ( $C_{\text{NaOH}} < 15 \mu\text{M}$ ) also showed large-sized metal crystallite due to the absence of glycolate. In addition, the Pd/C prepared by polyol reduction shows PdO crystallite peak with Pd crystallite peak whereas Pt/C catalysts showed only the Pt crystallite peak. The peaks at  $34^\circ$ ,  $55^\circ$ ,  $60^\circ$ , and  $72^\circ$  are corresponding to the PdO (002), (112), (200), and (202) crystalline planes, respectively. This result suggests that some Pd precursor was not reduced by polyol reduction because Pd precursor was changed to  $\text{Pd}(\text{OH})_2$  by NaOH addition.  $\text{Pd}(\text{OH})_2$  is not reduced by polyol reduction due to the weak reducibility of polyol reduction. In addition, it is very interesting that intensity of Pd crystallite peak is in inverse proportion to that of PdO crystallite peak. In low NaOH concentration region ( $C_{\text{NaOH}} < 35 \mu\text{M}$ ), the increasing intensity for PdO peak and the decreasing intensity for Pd peak are simultaneously observed when the concentration of NaOH increases. This result indicates that amount of  $\text{Pd}(\text{OH})_2$  increases with concentration of NaOH in low concentration of NaOH ( $C_{\text{NaOH}} < 35 \mu\text{M}$ ).

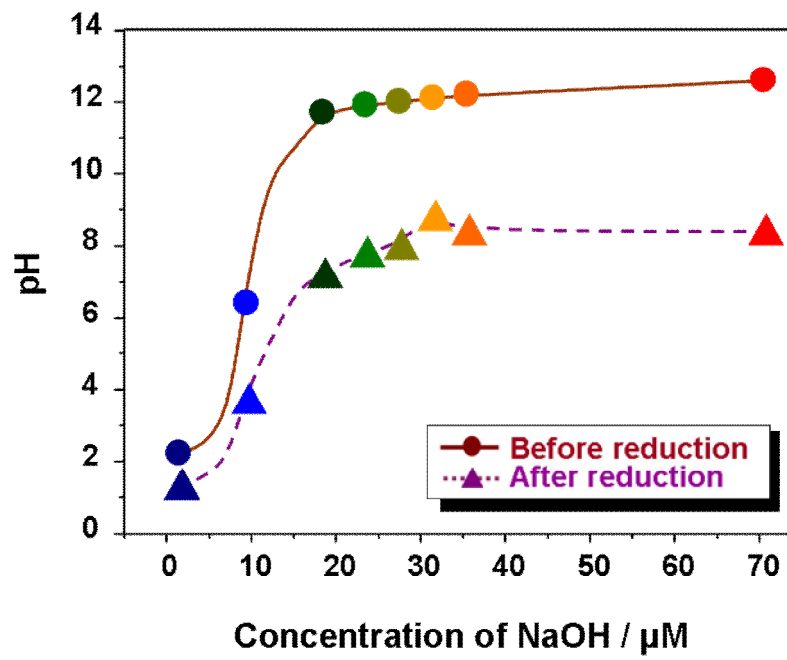


Fig. 24. pH profile in polyol reduction.

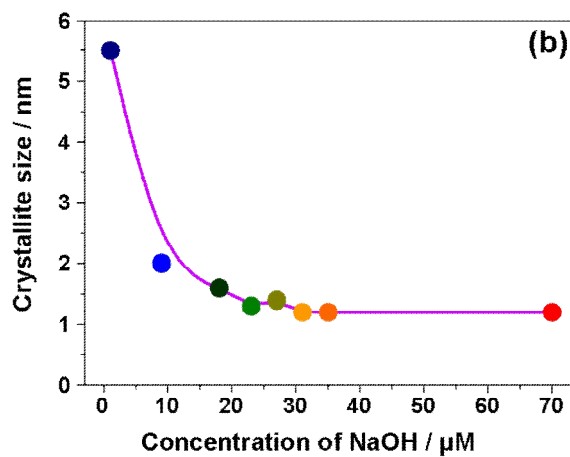
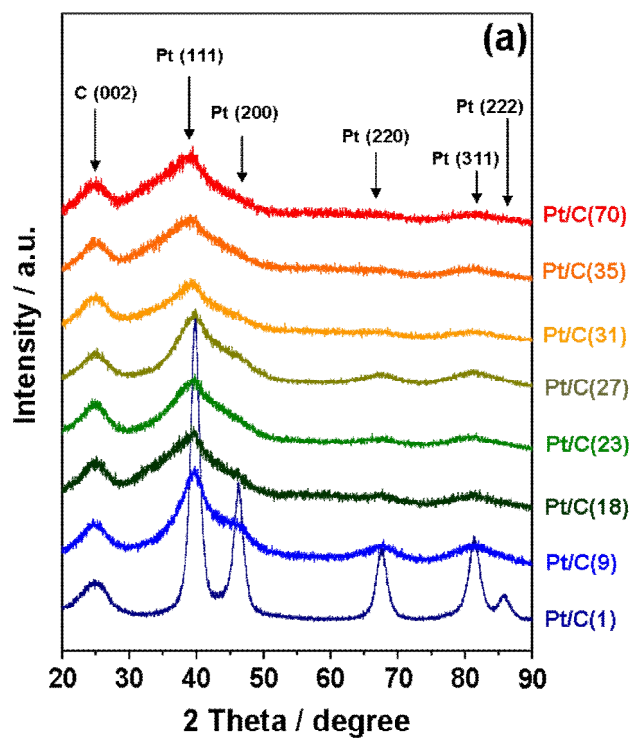


Fig. 25. (a) X-ray diffraction pattern of Pt/C and (b) crystallite size calculated from XRD data.

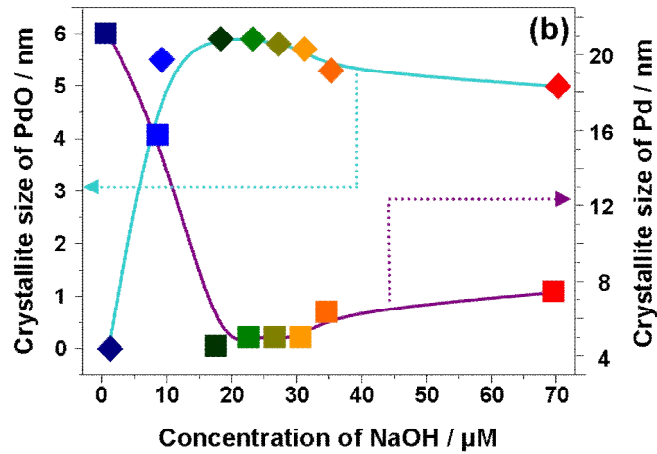
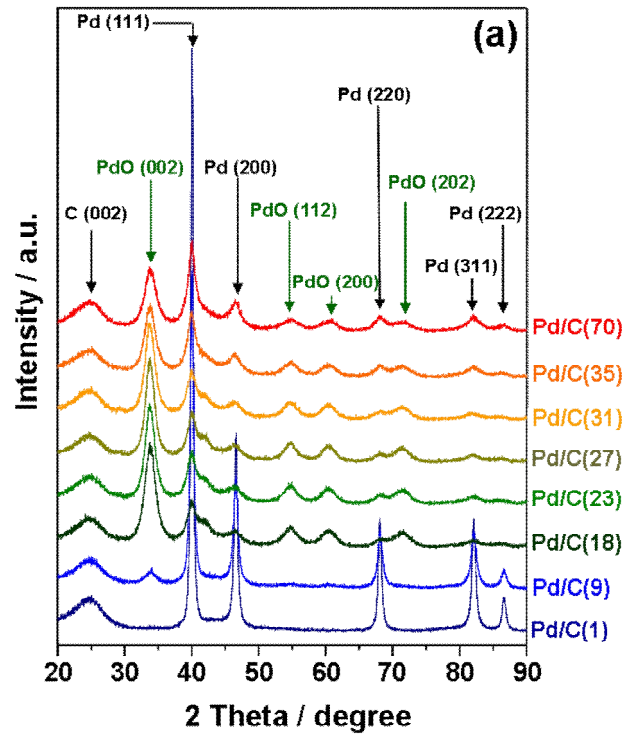


Fig. 26. (a) X-ray diffraction pattern of Pd/C and (b) crystallite size calculated from XRD data.

However, Pd/C catalysts also showed large-sized Pd crystallites when they were prepared by polyol reduction in high concentration of NaOH ( $C_{\text{NaOH}} > 35 \mu\text{M}$ ) due to high concentration of ionized Pd because a part of  $\text{Pd}(\text{OH})_2$  is changed to ionized Pd in basic solution ( $\text{pH} > 10$ ) [124]. Because only ionized Pd can be reduced by polyol, large-sized metal crystallites in basic solution might be attributed to the reduction of high concentration of ionized Pd.

In this study, PtPd/C catalyst were prepared by polyol reduction with fixed atomic ratio (Pt:Pd=3:1). Fig. 27(a) shows the XRD data of PtPd/C catalysts. All the catalysts show metal crystallite peaks corresponding to the face-centered cubic (fcc) structure. Fig. 27(b) shows the crystallite size calculated from XRD data. The catalyst prepared on very low concentration of NaOH ( $C_{\text{NaOH}} < 15 \mu\text{M}$ ) showed large-sized metal crystallites due to the absence of glycolate. In addition, the catalyst prepared on high concentration of NaOH ( $C_{\text{NaOH}} > 35 \mu\text{M}$ ) also showed size growth for metal crystallite because more ionized Pd were reduced with Pt precursor. In the polyol reduction, crystallite size of Pt-Pd alloy is larger than pure Pt because Pt is more stable material than Pd. An expanded view of the Pt (111) peak is shown in Fig. 28. It is already reported that main diffraction peak of Pt (111) shifted to higher angle with increasing the degree of Pt-Pd alloy because Pd atom which has smaller size than Pt was inserted to Pt lattice structure [125]. The shifted Pt crystallite peaks shown in Fig. 28 indicate that the ionized Pd and the Pt precursor prepare the Pt-Pd alloy because the ionized Pd and Pt precursor are simultaneously reduced by polyol reduction.

In order to observe the relation between concentration of NaOH and structure of PtPd nanoparticle, PtPd/C(1), PtPd/C(27), and PtPd/C(70) catalysts were chosen to represent each NaOH concentration. In order to confirm the chemical composition of catalysts and the loading amount of metal, ICP-AES analysis was conducted, and it is shown in Table 5. All the chosen PtPd/C showed similar metal composition, and each total amount of metal loaded on the carbon was closed to 20 wt%. This result indicates that all of the metals were deposited on the carbon support quantitatively, and effect of metal composition was negligible.

TEM images and of the PtPd/C catalysts are shown in Fig. 29. Semi-transparent cluster were carbon particles and black dots were metal particles on the carbon. TEM image of PtPd/C(1) showed relatively poor metal dispersion, compared to those of PtPd/C(27) and PtPd/C(70). This catalyst shows not only large-size metal nanoparticles but also particle agglomeration, indicating that PtPd/C(1) was not protected by stabilizing effect of glycolate in polyol reduction. On the other hand, the other catalysts showed well-dispersed metal nanoparticles without particle aggregation because of stabilizing effect of glycolate. PtPd/C(70) shows larger-sized metal nanoparticles than PtPd/C(27) because Pt-Pd alloy nanoparticles were prepared by polyol reduction. PtPd(27) shows the smallest nanoparticles, and they had a narrow particle size distribution between 1.0 and 3.5 nm

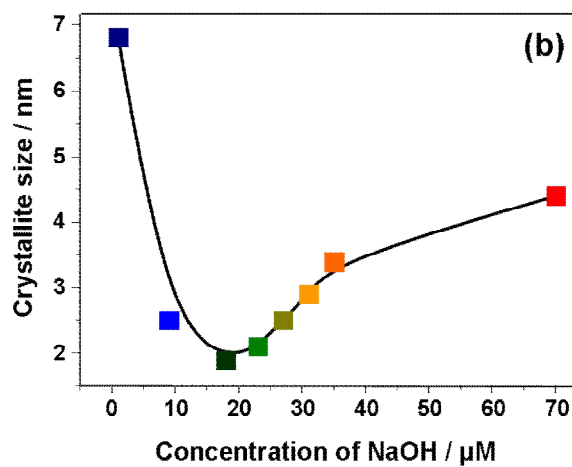
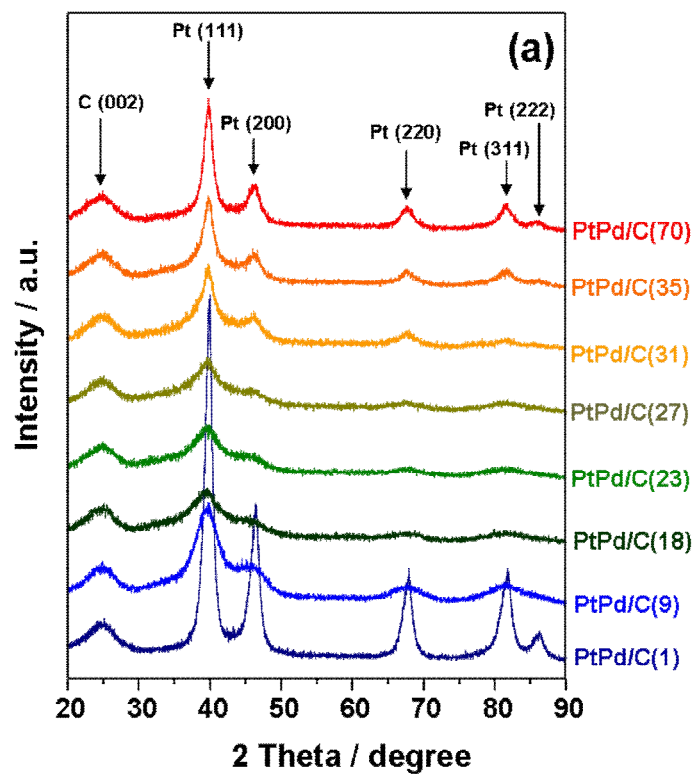


Fig. 27. (a) X-ray diffraction pattern of PtPd/C and (b) crystallite size calculated from XRD data.

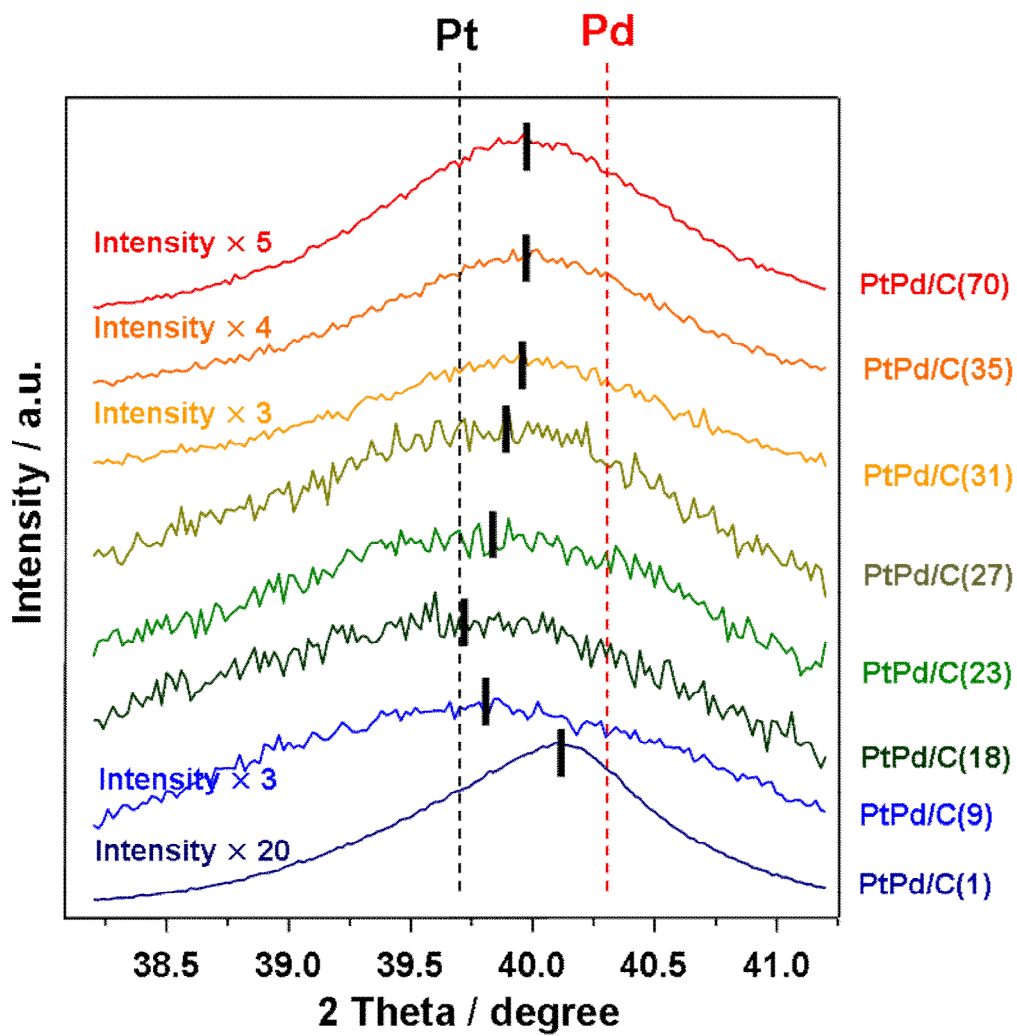


Fig. 28. Expanded X-ray diffraction patterns of PtPd/C catalysts.

Table 5. ICP-AES data and atomic ratio of PtPd/C catalysts

Catalyst	Amount of metal / wt%		Pt / Pd mole ratio
	Pt	Pd	
PtPd/C(70)	16.27	2.67	3.32
PtPd/C(27)	16.57	2.63	3.42
PtPd/C(1)	16.98	2.73	3.37

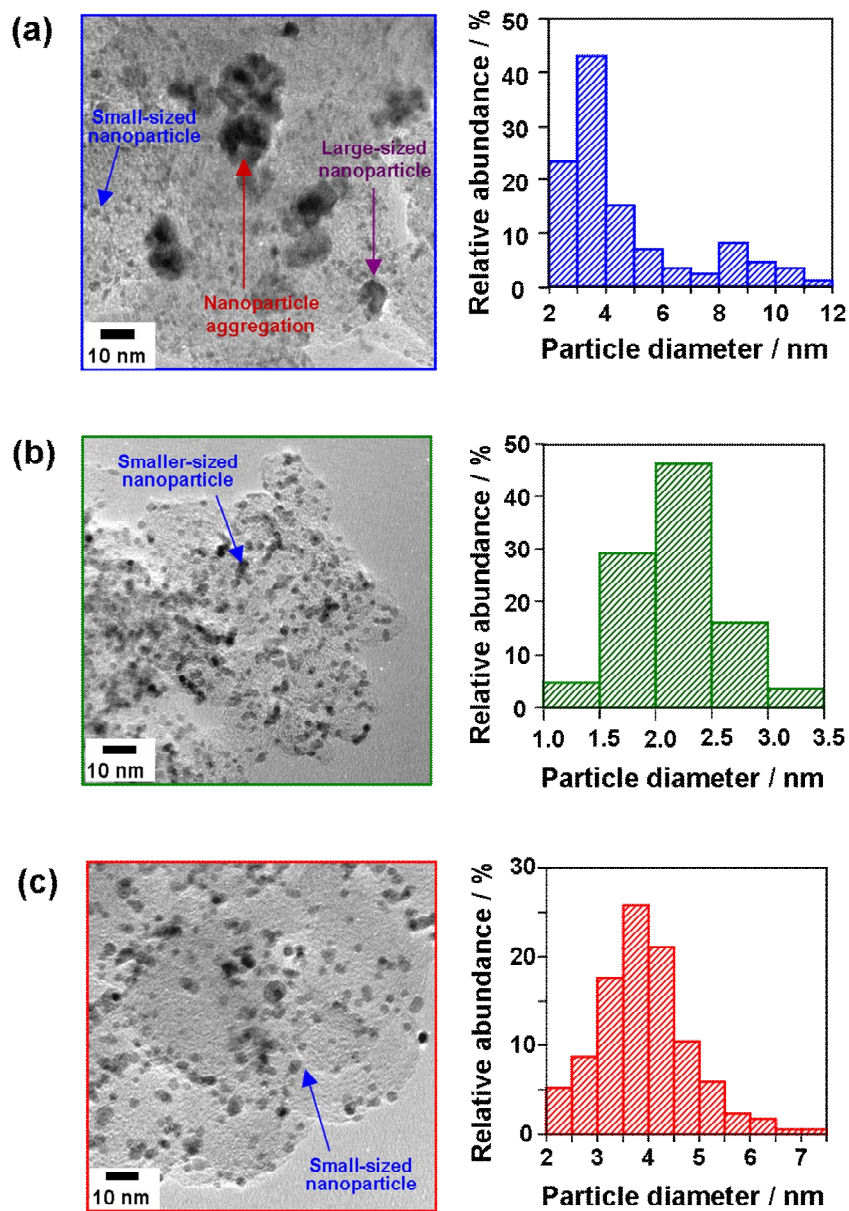


Fig. 29. TEM images and histograms of the particle size distribution of (a) PtPd/C(1) , (b) PtPd/C(27), and (c) PtPd/C(70) catalysts.

In XRD data of the Pd/C, Pd precursor was not completely reduced by polyol reduction due to the weak reducibility of polyol reduction. However, the PtPd/C catalysts did not show the peak of PdO crystallite even though the Pd precursor was used to prepare nanoparticles. In order to know the reason for the PdO disappearance, Pd/C was prepared by polyol reduction using Pt/C as a support instead of carbon. This catalyst was denoted as Pd/Pt/C. Fig. 30 shows XRD patterns of Pd/C and Pd/Pt/C catalysts. As discussed in XRD data of Pd/C catalysts, Pd/C showed various peaks related to Pd and PdO crystallites, simultaneously, whereas Pd/Pt/C catalyst shows only Pd crystallite peaks. This result indicates that Pd(OH)<sub>2</sub> could be reduced by polyol reduction when Pt nanoparticles are in solution due to the catalytic effect of Pt surface.

In order to confirm the Pd atoms prepared by catalytic effect of Pt nanoparticles, TPHD (temperature programmed hydrogen desorption) of PtPd/C and Pd/C were observed. In addition, TPHD of bimetallic catalyst (Pt-Pd/C) was also observed to compare TPHD. Fig. 31 showed TPHD of Pd/C, Pt-Pd/C, and PtPd/C catalysts. Pd/C shows very sharp TPHD peak at 50 °C (Fig. 31(a)). In addition, Pt-Pd/C shows small TPHD peak at 50 °C because loading amount of Pd is only 3.1 wt% (Fig. 31(b)). On the other hand, all PtPd/C catalysts do not show any TPHD peak (Fig. 31(c)). It is reported that preparation of perfectly mixed Pt-Pd catalyst should lead to featureless TPHD (temperature programmed hydrogen desorption) profiles, i.e. without any peaks demonstrating hydrogen release during hydrogen decomposition [126]. All the

3Pt1Pd/C catalysts don't have palladium nanoparticles because the decomposition peak of palladium  $\beta$ -hydride cannot be observed. It means that Pd atoms prepared by catalytic effect of Pt nanoparticles were placed on the Pt surface. The Pd atoms placed on the Pt surface enhanced the ORR activity of Pt because of Pt-Pd alloy effect.

From the XRD, TEM, and TPR data, the reduction process of the 3Pt1Pd/C was suggested that Pt(actually, Pt-rich) nanoparticles were prepared first, and then Pd(OH)<sub>2</sub> was reduced on the surface of Pt nanoparticles. Therefore, Core-Shell typed nanoparticles(core;Pt-rich, shell; Pd) could be prepared by polyol reduction with optimum NaOH concentration ( $15 \mu\text{M} < C_{\text{NaOH}} < 35 \mu\text{M}$ ) (Fig. 32).

#### 4.3.1.2 Electrochemical activity

Although all the PtPd/C catalysts had similar metal loading amounts, the catalysts showed different electrochemical properties depending on pH value during preparation because metal compositions of each surface were different. In the CO-stripping test (Fig. 33), the PtPd/C(27) showed CO desorption peak at higher potential than the other PtPd/C catalysts. This result indicates that the OH<sub>ads</sub> on the PtPd/C(27) formed at higher potential than the other PtPd/C's because the OH<sub>ads</sub> transformed the adsorbed CO to CO<sub>2</sub>.

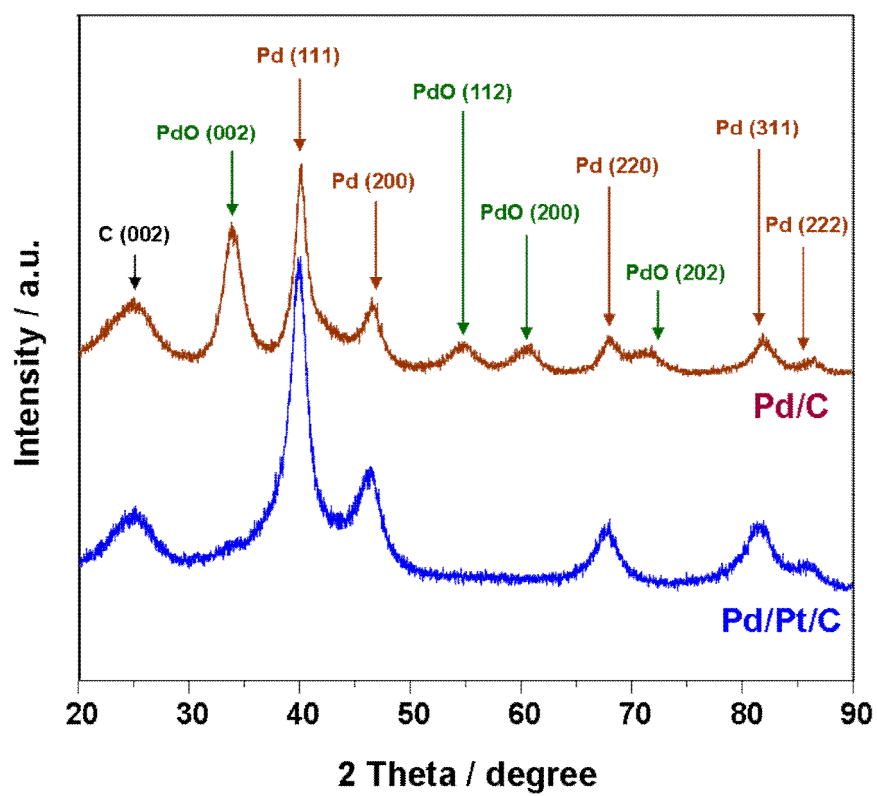
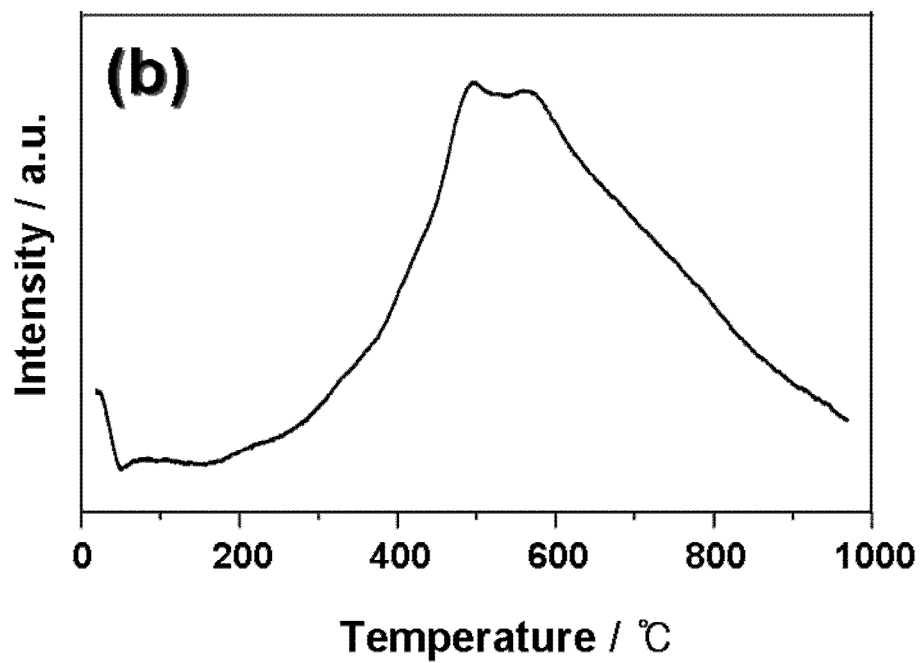
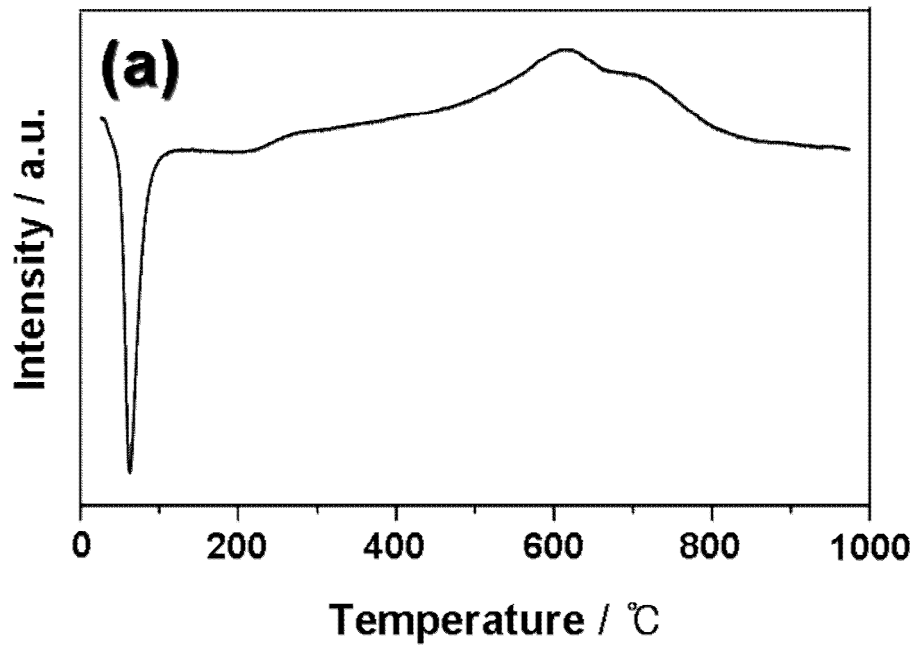


Fig. 30. X-ray diffraction patterns of Pd/C and Pd/Pt/C catalysts.



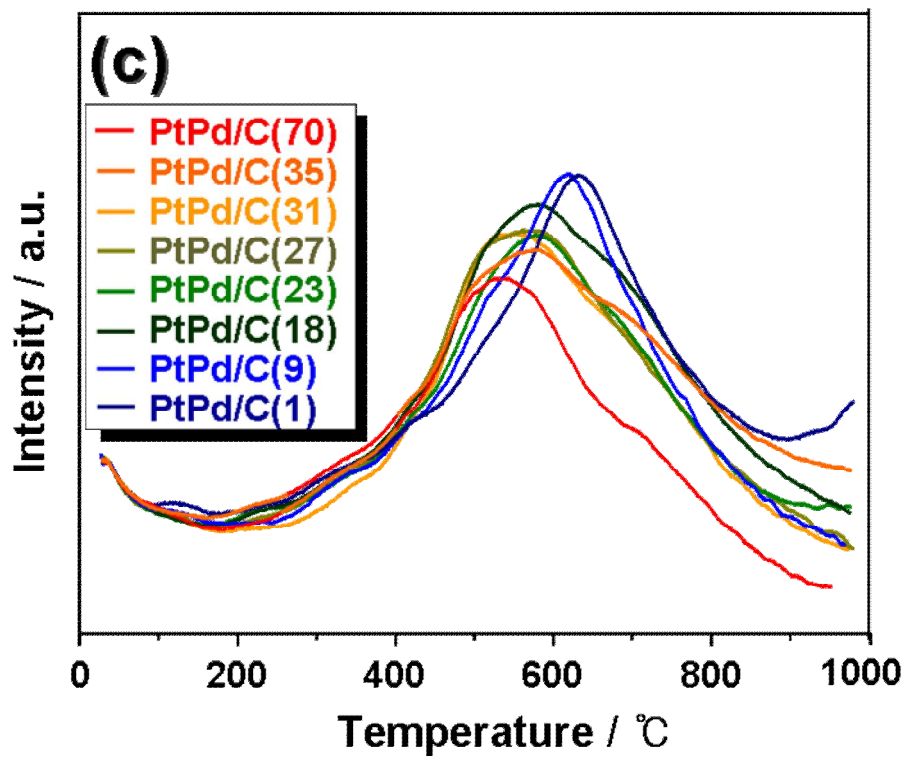


Fig. 31. TPR data of (a) Pd/C, (b) Pt-Pd/C, and (c) PtPd/C catalysts.

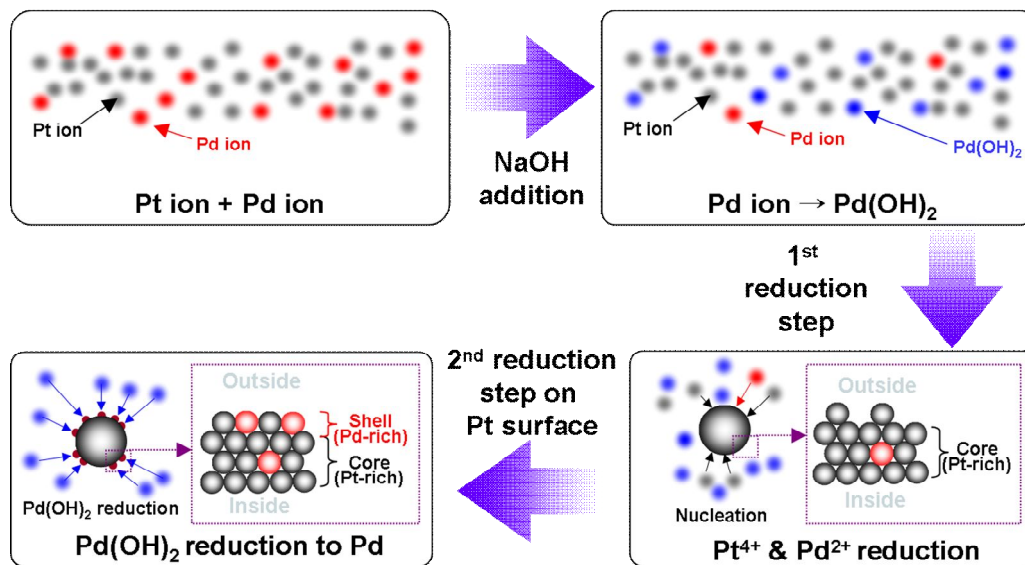


Fig. 32. Schematic diagram of core-shell type nanoparticles preparation.

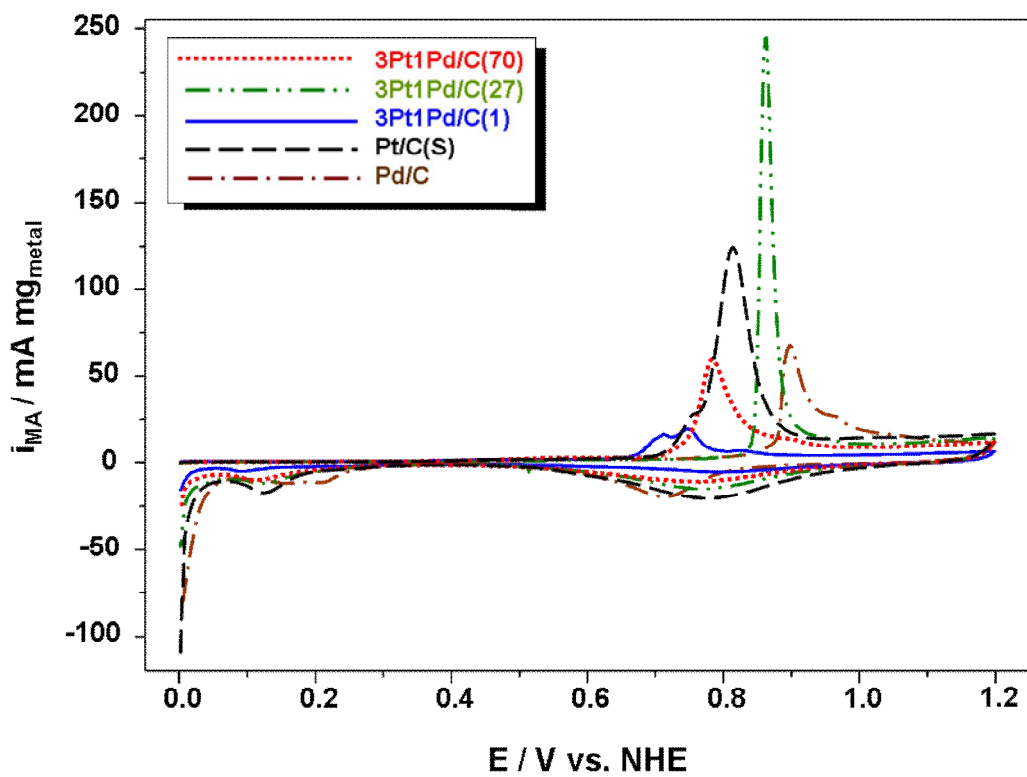


Fig. 33. CO-stripping voltammograms of Pt/C, Pd/C, and PtPd/C catalysts.

The PtPd/C catalysts were investigated in RDE measurement as described in the experimental section to study the catalytic activities of the prepared catalyst and their ORR kinetics. Based on the ORR data, the optimum concentration of NaOH is 27  $\mu\text{M}$ . Fig. 55 shows voltammograms of the PtPd/C, Pt/C(S), and Pt/C(C) catalysts for the catalytic activity for the ORR obtained at 20°C in 1 M HClO<sub>4</sub> electrolyte solution saturated with oxygen using RDE at 2500 rpm.

The kinetic current densities per milligram of Pt at two different potential for the PtPd/C, Pt/C(S), and Pt/C(C) catalysts are shown in Fig. 35. The kinetic current density at 0.85 V for PtPd/C(27) is about 5 times that of a Pt/C(C). The enhanced ORR activity for the PtPd/C(27) was caused by the shifted potential for the OH adsorption as mentioned above.

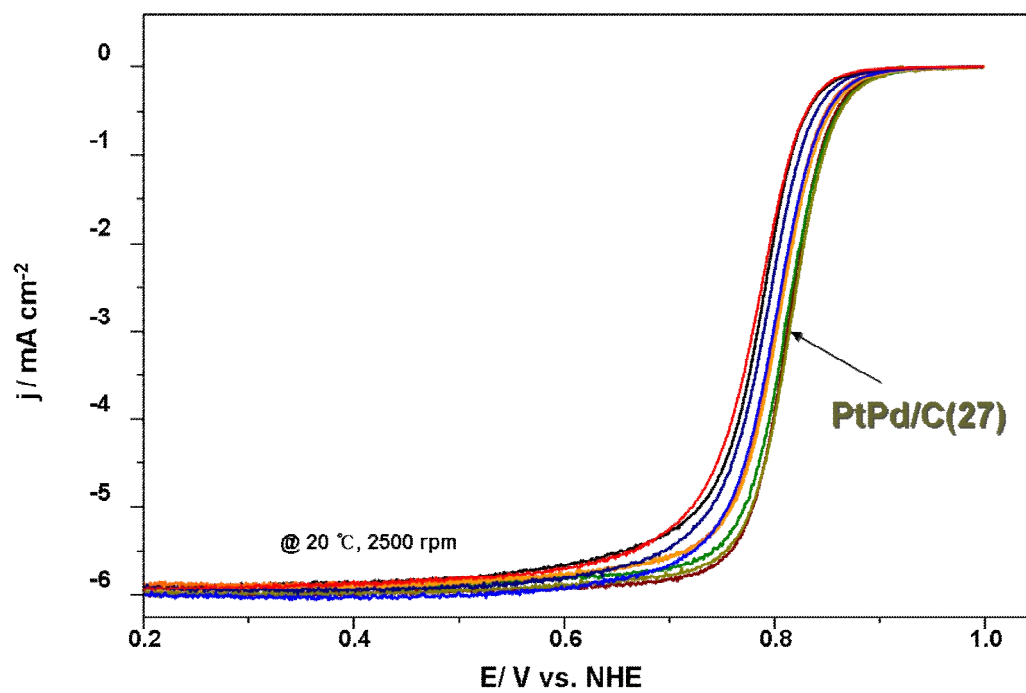


Fig. 34. Linear scan voltammograms of PtPd/C catalysts in 1 M HClO<sub>4</sub> saturated with pure oxygen at the scan rate 1 mV/s with the rotating speed of 2500 rpm.

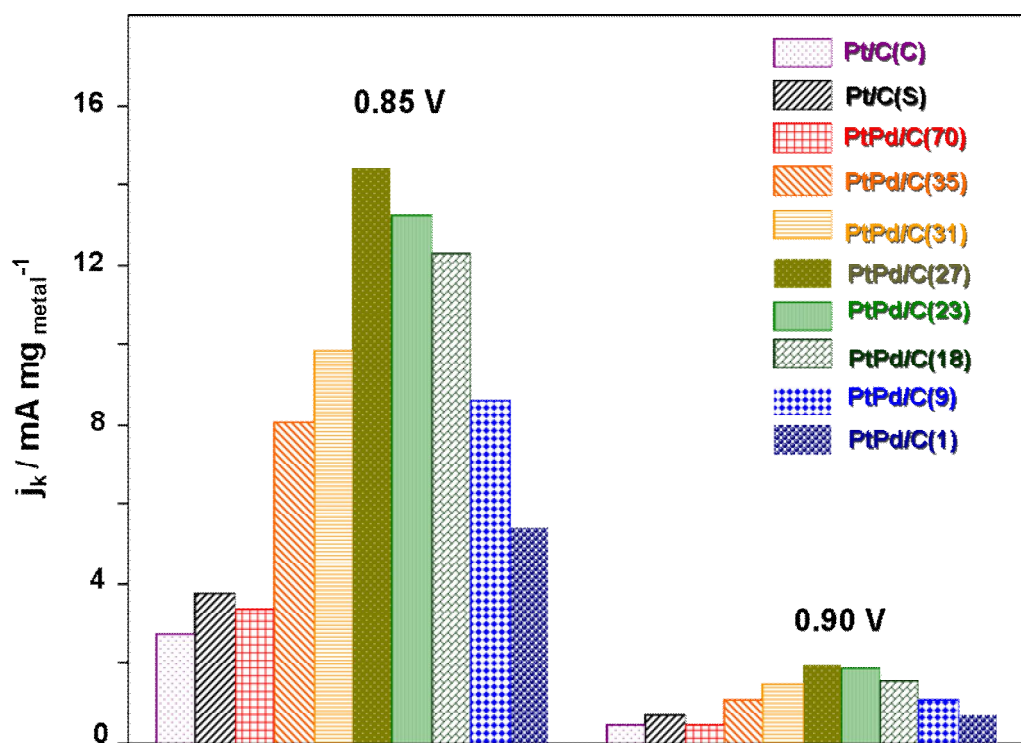


Fig. 35. Mass activities at 0.85 and 0.90 V for Pt/C and PtPd/C catalysts.

## 4.3.2 xPtyPd/C catalyst characterization

### 4.3.2.1 Physical characterization

In order to enhance ORR activity, 3Pt1Pd/C, 5Pt1Pd/C, and 7Pt1Pd/C catalysts were prepared with different Pt:Pd ratio (3:1, 5:1, and 7:1). In addition, Pt/C and Pd/C catalysts were also prepared to compare activities. In this study, all the catalysts were prepared by polyol reduction with a concentration of 27  $\mu\text{M}$  NaOH to prepare core-shell typed nanoparticles. In this NaOH concentration, most of Pd precursor changed to the  $\text{Pd}(\text{OH})_2$ . During the polyol reduction procedure, core formed from Pt precursor and remaining Pd precursor and then the formed  $\text{Pd}(\text{OH})_2$  was reduced on the surface of the core. The Pd atoms reduced from  $\text{Pd}(\text{OH})_2$  was placed on the outside of the nanocores. Resultantly, core-shell typed nanoparticles(core;Pt-rich, shell-Pd) could be prepared by polyol reduction.

Fig. 36 shows the XRD data of prepared catalysts. Among the prepared catalysts, only Pd/C shows PdO crystallite peak because the Pd/C does not have Pt atom. Therefore,  $\text{Pd}(\text{OH})_2$  prepared by NaOH addition could not be reduced by polyol reduction. The other catalyst showed metal crystallite peak corresponding to the fcc structure. As shown in crystallite size calculated from XRD data (Table 6), crystallite size increases with Pd ratio because core has more amount of Pd. This result is also

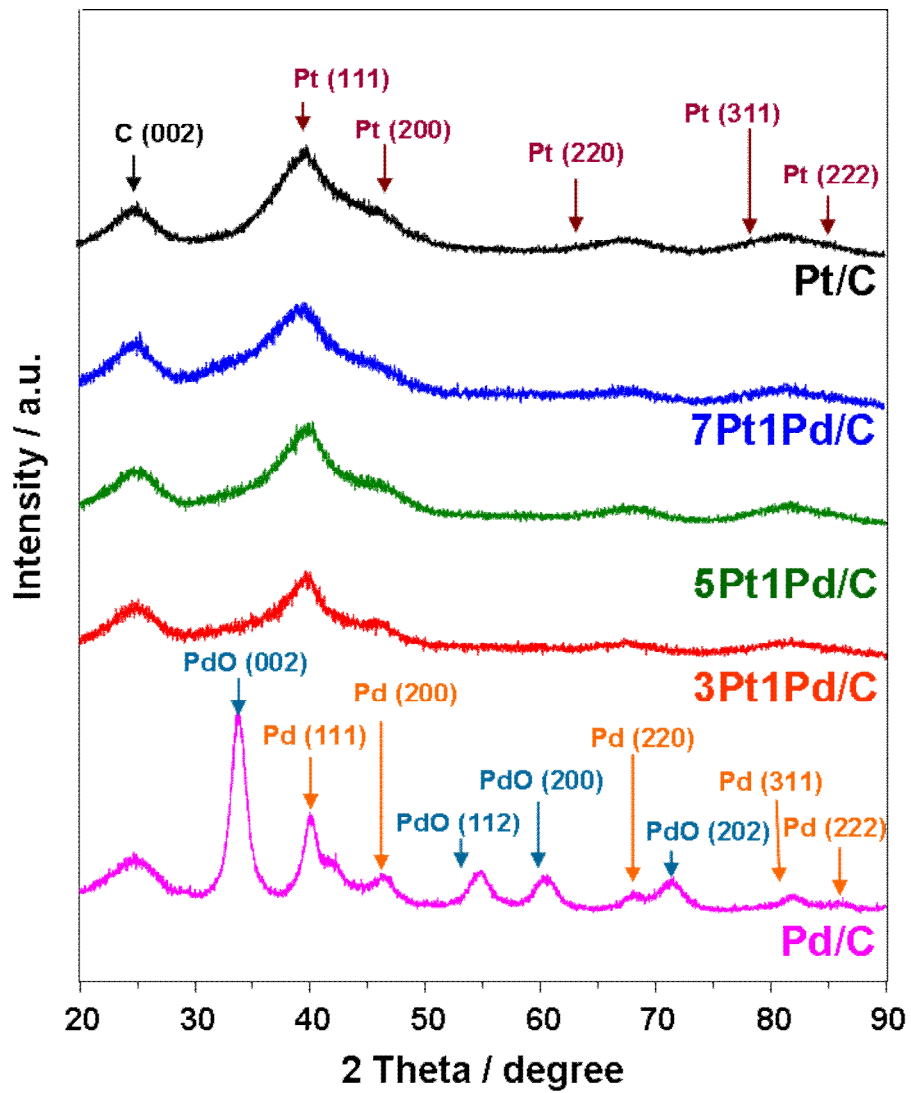


Fig. 36. X-ray diffraction patterns of Pt/C, 7Pt1Pd/C, 5Pt1Pd/C, 3Pt1Pd/C, and Pd/C catalysts.

Table 6. Crystallite sizes of metal and metal oxide calculated from XRD data

Catalyst	Crystallite size of metal / nm	Crystallite size of metal oxide / nm	EAS
Pt/C	1.8	-	231
7Pt1Pd/C	1.9	-	204
5Pt1Pd/C	2.1	-	187
3Pt1Pd/C	2.5	-	166
Pd/C	6.1	5.2	n.m

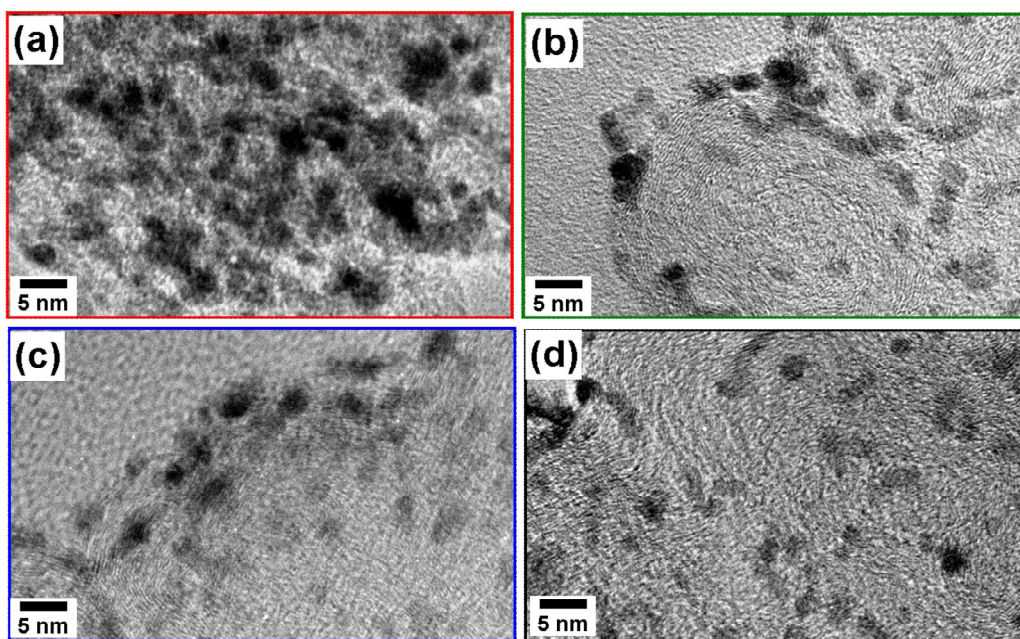


Fig. 37. TEM images of (a) 3Pt1Pd/C, (b) 5Pt1Pd/C(c) 7Pt1Pd/C (d) Pt/C catalysts.

observed in TEM images. In Fig. 37, crystallite size of the catalysts was, in decreasing order: Pt/C > 7Pt1Pd/C > 5Pt1Pd/C > 3Pt1Pd/C > Pd/C.

#### 4.3.2.2. Electrochemical activity

In order to evaluate the EAS of the prepared catalysts, a cyclic voltammetry experiment was carried out. The potential was cycled between 0 and 1.2 V (vs. NHE) at 20 mV/s in a 0.5 mol/L H<sub>2</sub>SO<sub>4</sub> aqueous solution purged with N<sub>2</sub> at 25 °C. In Fig. 29, all the catalysts exhibited well-defined H<sub>2</sub> adsorption/desorption peaks in the potential range of 0.0–0.3 V. From the integrated charge in the H<sub>2</sub> adsorption/desorption region, the EAS values of the catalysts can be calculated as suggested by Gasteiger *et al.* [77]. The observed EAS values are also summarized in Table 6. Among the prepared catalysts, EAS of Pd/C could not be calculated using H<sub>2</sub> adsorption/desorption region because H<sub>2</sub> release peak was observed in the same region (Fig. 38(b)). The EAS value of the Pt/C was higher than those of the other catalysts because of the smaller-sized Pt nanoparticles. This improved EAS is attributed to the high Pt surface utilization by the highly dispersed Pt nanoparticles on the carbon support, as shown by the XRD result (Table 6). In addition, the higher EAS value of the smaller-sized Pt nanoparticles suggests that the surface of the small-sized Pt nanoparticles could be an active site for electrochemical reactions.

The prepared catalysts were evaluated in the RDE measurement as described in the experimental section to study the ORR kinetics. Fig. 6 shows voltammograms of the synthesized catalysts prepared by polyol reduction for ORR obtained at 20 °C in 1 M HClO<sub>4</sub> aqueous solution saturated with oxygen using RDE at 2500 rpm. Among the catalysts, 5Pt1Pd/C showed the highest ORR activity in the kinetic current region (0.85~0.90 V) in spite of larger particle size than that of 7Pt1Pd/C because 7Pt1Pd/C had insufficient Pd atoms in the shell.

It is generally known that the OH adsorbed on the Pt surface inhibits the ORR, and this adsorbed OH is not derived from the reduction of O<sub>2</sub> but rather from the reaction between H<sub>2</sub>O and Pt [92]. Therefore, OH adsorption/desorption of 5Pt1Pd/C were evaluated. In Fig. 2, 5Pt1Pd/C showed CO desorption peak at higher potential than the other PtPd/C catalysts. This result indicates that the OH<sub>ads</sub> on the 5Pt1Pd/C formed at higher potential than the other PtPd/C's because the OH<sub>ads</sub> transformed the adsorbed CO to CO<sub>2</sub>.

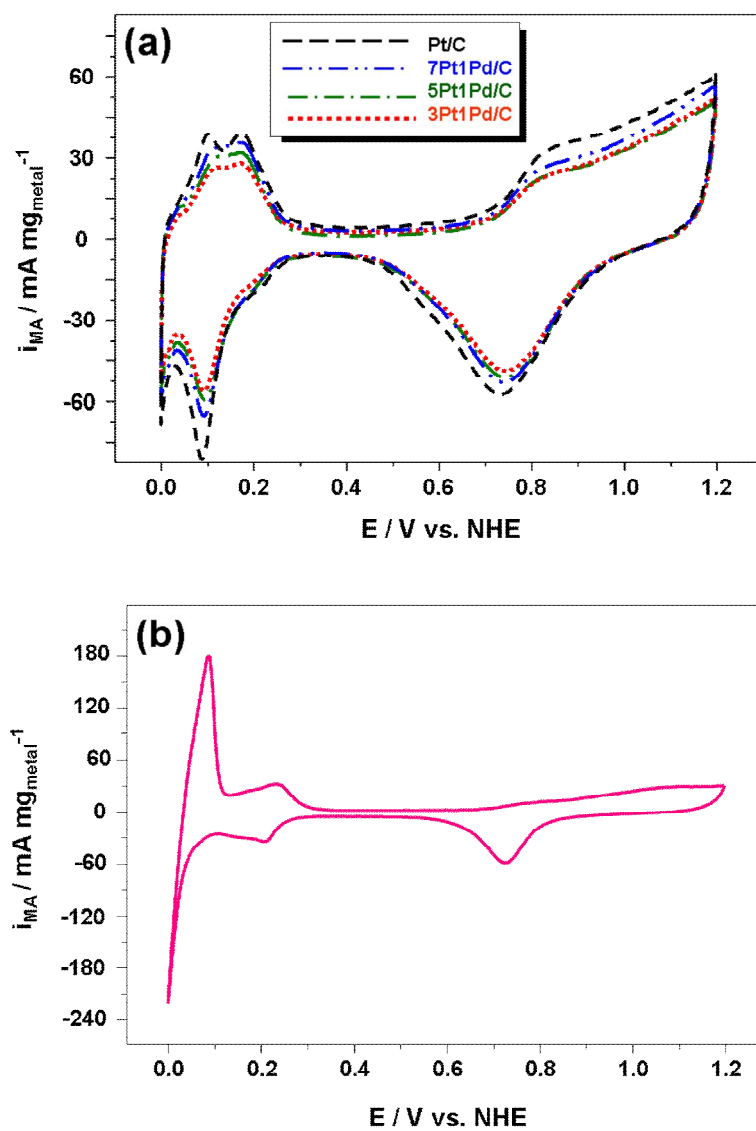


Fig. 38. Cyclic voltammograms for (a) Pt/C and PtPd/C catalysts and (b) Pd/C catalyst.

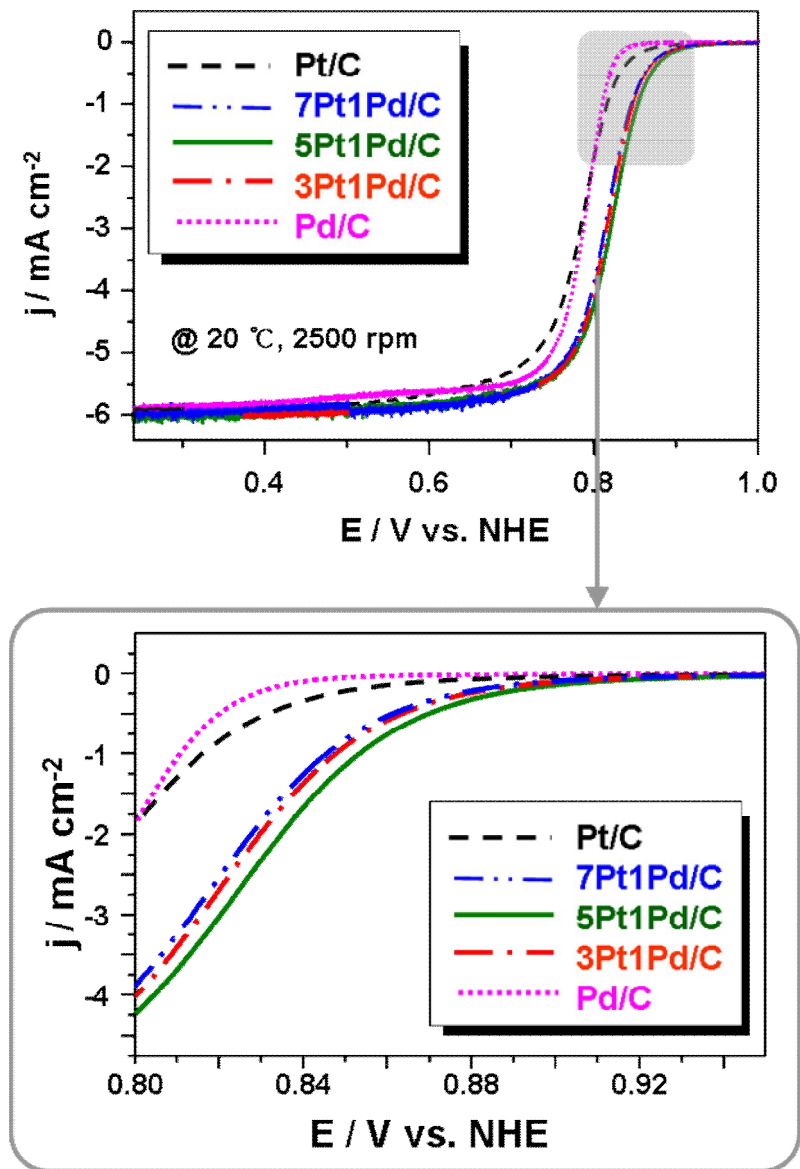


Fig. 39. Linear scan voltammograms of Pd/C, 3Pt1Pd/C, 5Pt1Pd/C, 7Pt1Pd/C, and Pt/C catalysts in 1 M HClO<sub>4</sub> saturated with pure oxygen at the scan rate of 1 mV/s and with the rotating speed of 2500 rpm.

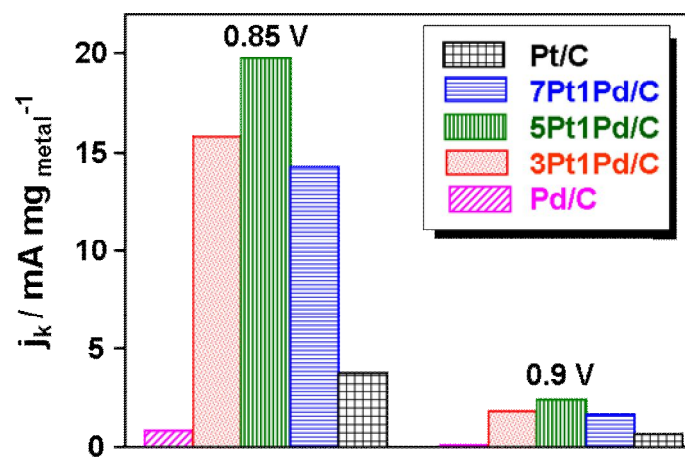


Fig. 40. Mass activities at 0.85 and 0.90 V for Pd/C, 3Pt1Pd/C, 5Pt1Pd/C, 7Pt1Pd/C, and Pt/C catalysts.

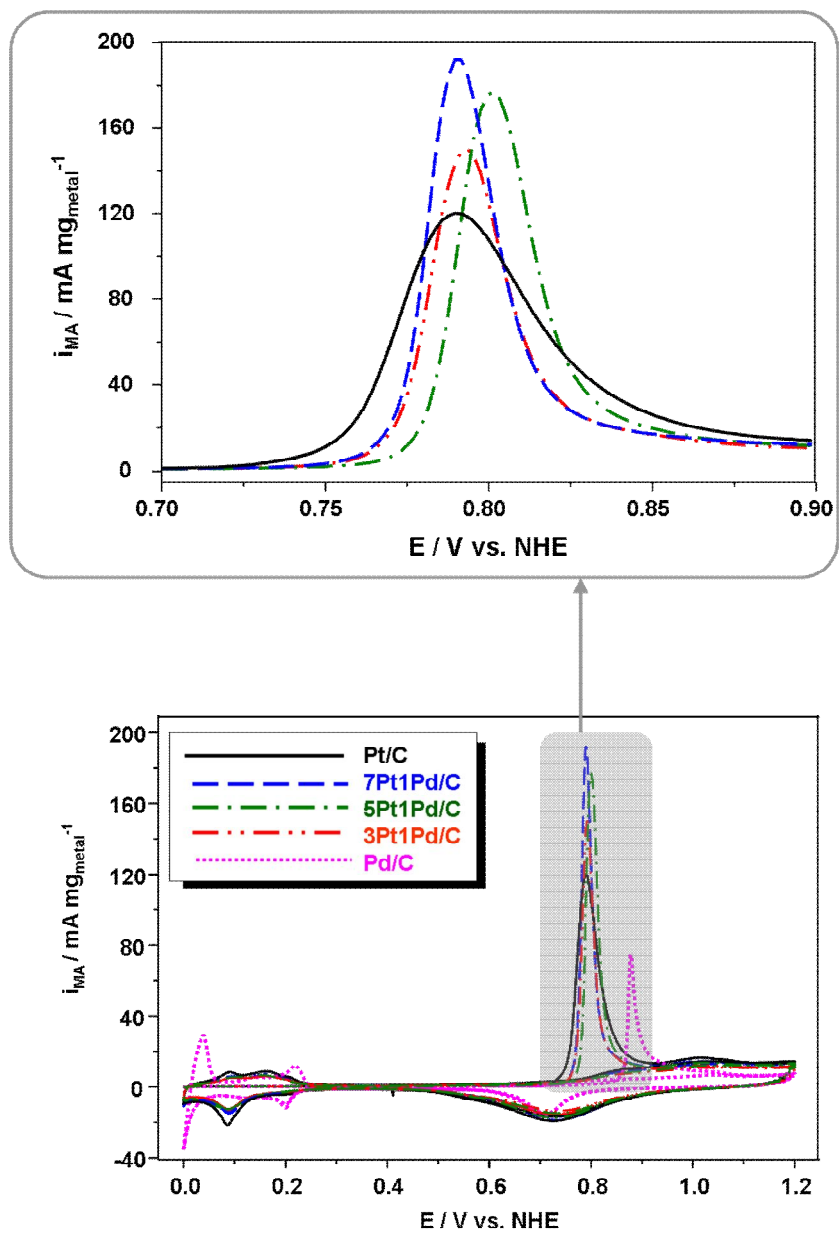


Fig. 41. CO-stripping voltammograms of Pd/C, 3Pt1Pd/C, 5Pt1Pd/C, 7Pt1Pd/C, and Pt/C catalysts.

### 4.3.3. 5Pt1Pd/Ce<sub>0.5</sub>Zr<sub>0.5</sub>O<sub>2</sub>-C catalyst characterization

#### 4.3.3.1. Physical characterization

In order to enhance ORR activity, Ce<sub>0.5</sub>Zr<sub>0.5</sub>O<sub>2</sub> nanoparticles were added to the 5Pt1Pd/C catalyst which had the best activity in previous study. Ce<sub>0.5</sub>Zr<sub>0.5</sub>O<sub>2</sub> nanoparticles were prepared by hydrothermal treatment with optimum reaction condition (solvent; H<sub>2</sub>O, reaction time; 10 h). In polyol reduction, atomic ratio of Pt/Pd and concentration of NaOH were fixed at 5:1 and 27 μM, respectively.

Fig. 42 shows TEM image and EDS data of prepared 5Pt1Pd/Ce<sub>0.5</sub>Zr<sub>0.5</sub>O<sub>2</sub>-C catalyst. The nanoparticles were well dispersed on the carbon support without particle aggregation, and they had a narrow particle size distribution. The average particle size was around 2 nm. However, it is difficult to separate metal and metal oxide because two kinds of nanoparticles have very similar particle size. However, it is thought that PtPd nanoparticles coexists with Ce<sub>0.5</sub>Zr<sub>0.5</sub>O<sub>2</sub> because EDS data show Pt, Pd, Ce, and Zr peaks, simultaneously.

#### 4.3.3.2 Electrochemical activity

In order to evaluate the ORR activity, 5Pt1Pd/Ce<sub>0.5</sub>Zr<sub>0.5</sub>O<sub>2</sub>-C and 5Pt1Pd/C catalysts were investigated in RDE measurement. Figs. 43 and 44 obviously show that addition of Ce<sub>0.5</sub>Zr<sub>0.5</sub>O<sub>2</sub> enhance the ORR activity and mass activity. In addition, Tafel

plot was used to evaluate the kinetics of the ORR on the prepared catalysts,. Assuming that the kinetic at rotating disk is mainly activation-controlled in the range  $0.78 < E < 0.85$  V, the associated Tafel plot can be depicted after mass transport correction in the liquid electrolyte. Fig. 45 shows that the kinetic of 5Pt1P/Ce<sub>0.5</sub>Zr<sub>0.5</sub>O<sub>2</sub>-C is faster than 5Pt1Pd/C catalyst.

In order to confirm the Ce<sub>0.5</sub>Zr<sub>0.5</sub>O<sub>2</sub> addition effect on enhanced ORR activity, OH<sub>ads</sub> desorption and CO-stripping test were conducted. Fig. 46 shows that OH desorption potential of 5Pt1P/Ce<sub>0.5</sub>Zr<sub>0.5</sub>O<sub>2</sub>-C is higher than that of 5Pt1Pd/C. Similar result was also observed in CO-stripping test (Fig. 47).

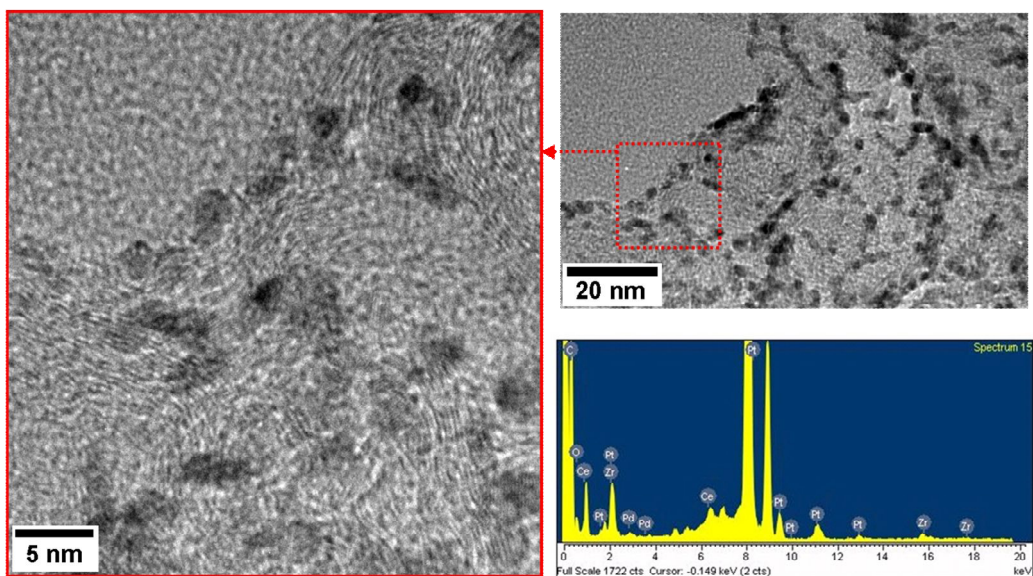
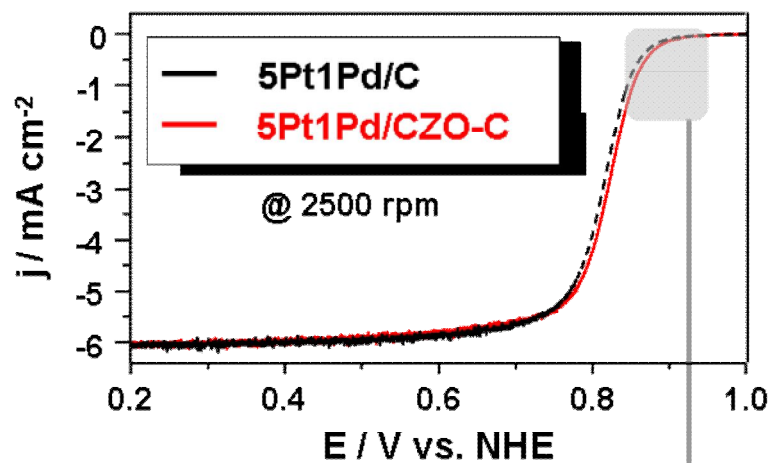


Fig. 42. TEM images and EDS data of 5Pt1Pd/Ce<sub>0.5</sub>Zr<sub>0.5</sub>O<sub>2</sub>-C catalyst.



**Kinetic current region**

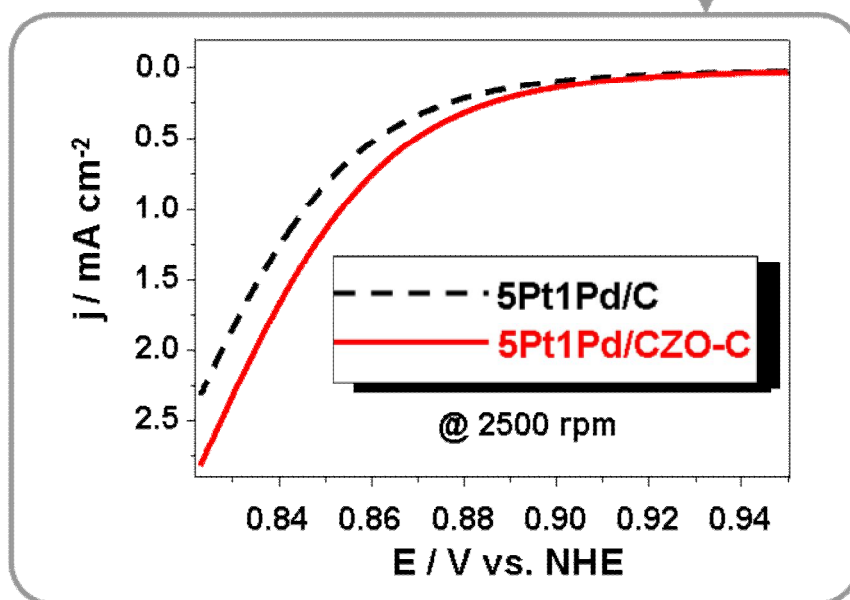


Fig. 43. Linear scan voltammograms of 5Pt1Pd/Ce<sub>0.5</sub>Zr<sub>0.5</sub>O<sub>2</sub>-C catalyst and 5Pt1Pd/C in 1 M HClO<sub>4</sub> saturated with pure oxygen at the scan rate 1 mV/s with the rotating speed of 2500 rpm.

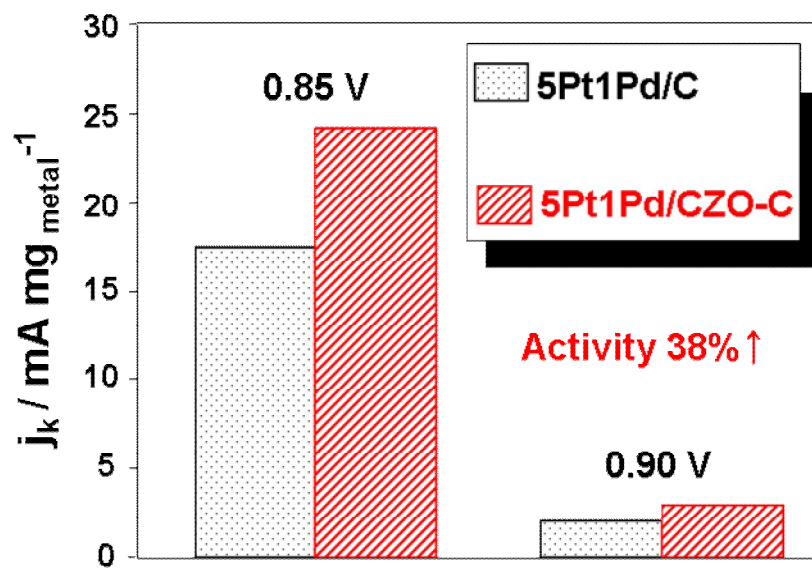


Fig. 44. Mass activities at 0.85 and 0.90 V for 5Pt1Pd/Ce<sub>0.5</sub>Zr<sub>0.5</sub>O<sub>2</sub>-C and 5Pt1Pd/C catalysts.

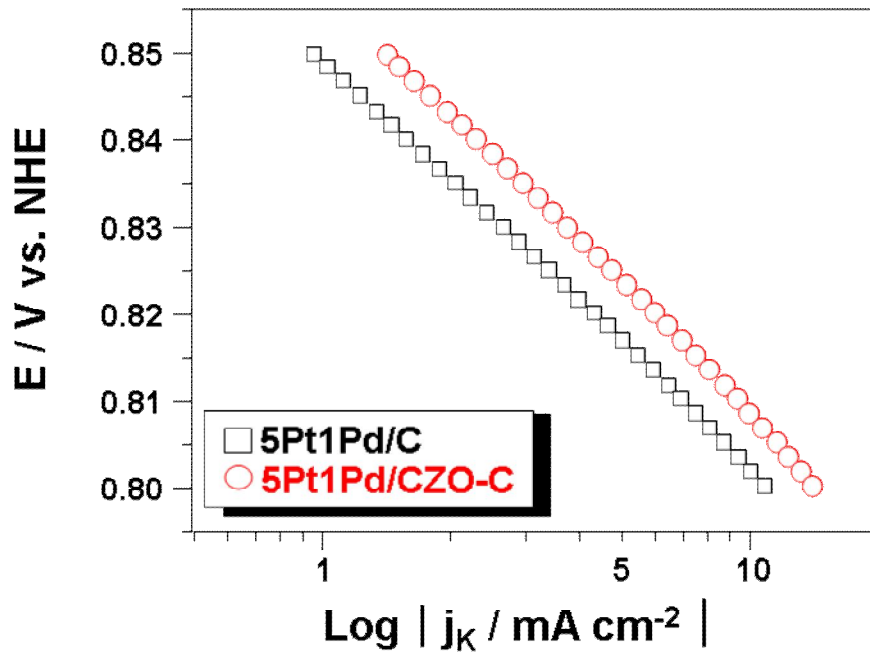


Fig. 45. Tafel plot for 5Pt1Pd/Ce<sub>0.5</sub>Zr<sub>0.5</sub>O<sub>2</sub>-C and 5Pt1Pd/C catalysts.

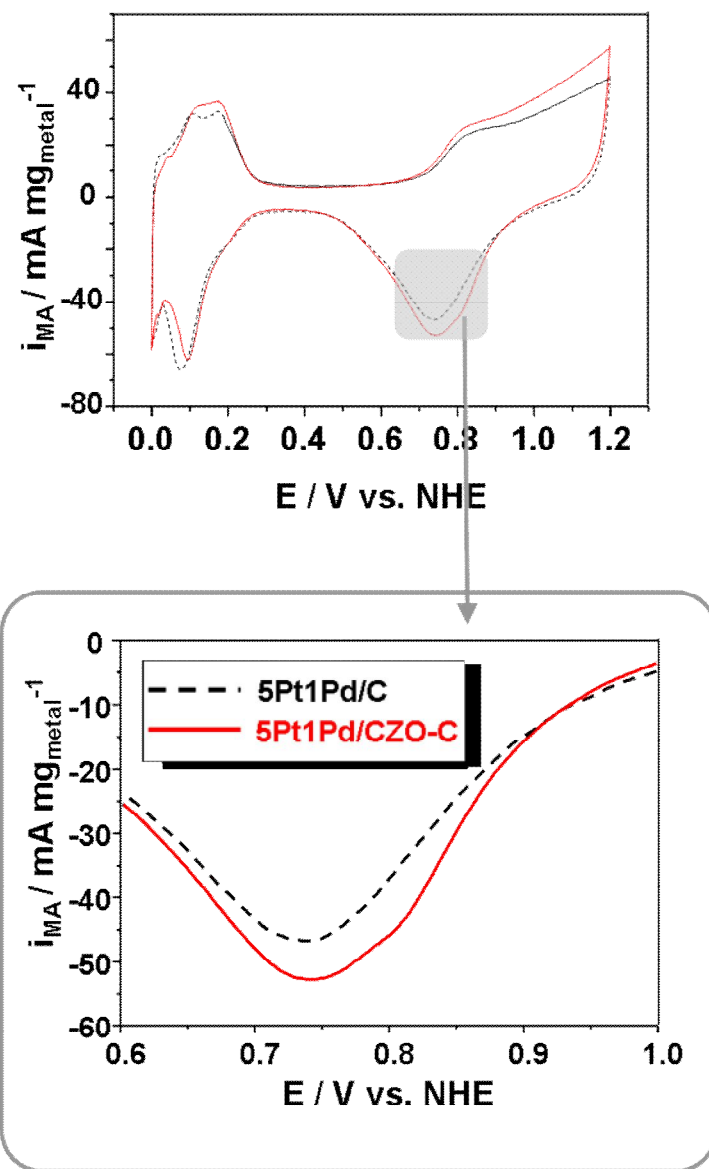


Fig. 46. Cyclic voltammograms of 5Pt1Pd/Ce<sub>0.5</sub>Zr<sub>0.5</sub>O<sub>2</sub>-C and 5Pt1Pd/C catalysts in 0.5 M H<sub>2</sub>SO<sub>4</sub> at the scan rate of 20 mV/s.

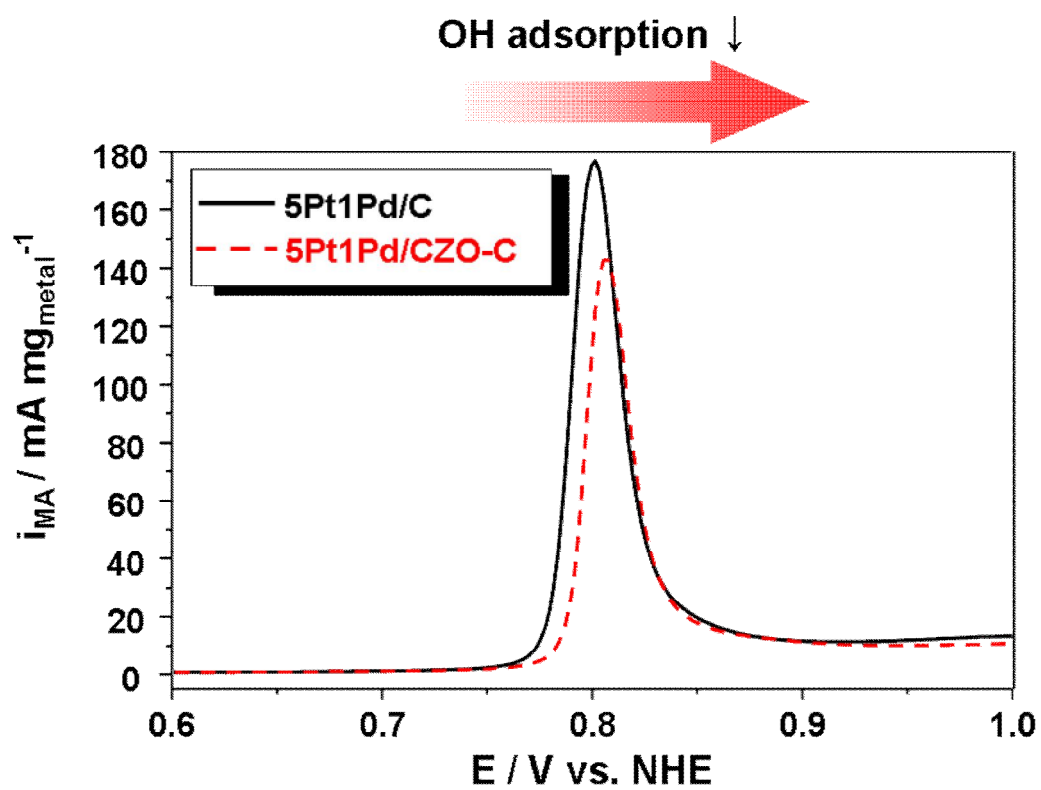


Fig. 47. CO-stripping voltammograms of 5Pt1Pd/Ce<sub>0.5</sub>Zr<sub>0.5</sub>O<sub>2</sub>-C and 5Pt1Pd/C catalysts.

#### 4.4. Conclusions

Core-shell typed PtPd nanoparticles on carbon support were developed to increase the alloyed active surface area. In order to prepare core-shell typed nanoparticles, all the catalysts were prepared by polyol reduction with a concentration of 27  $\mu\text{M}$  NaOH. In this NaOH concentration, most of Pd precursor changed to  $\text{Pd}(\text{OH})_2$ . During the polyol reduction procedure, a core formed from Pt precursor and remaining Pd precursor and then the formed  $\text{Pd}(\text{OH})_2$  was reduced on the surface of the core. Pd atoms reduced from  $\text{Pd}(\text{OH})_2$  were placed on the outside of the nanocores. Resultantly, core-shell typed nanoparticles(core;Pt-rich, shell-Pd) could be prepared by polyol reduction. In order to observe the relation between metal composition and ORR activity, several catalysts with different Pt/Pd ratio were prepared. Among the catalysts, 5Pt1Pd/C showed the highest ORR activity in the kinetic current region (0.85~0.90 V) in spite of larger particle size than that of 7Pt1Pd/C because the 7Pt1Pd/C had insufficient Pd atoms in the shell. From the CO-stripping test, it was observed that Pd atoms in the shell reduce OH adsorption on the Pt surface.

## References

1. R. O'hayre, S. W. Cha, W. Colella, and F. B. Prinz, *Fuel Cell fundamentals*, John-Wiley & Sons (2006).
2. S. Srinivasan, *Fuel Cells — from fundamentals to applications*, Springer (2006).
3. A. K. N. Reddy and J. O. M. Bockris, *Modern electrochemistry*, Plenum Press, New York (1973).
4. B. E. Conway and L. Bai, "Determination of Adsorption of H Species in the Cathodic Hydrogen Evolution Reaction at Pt in Relation to Electrocatalysis", *J. Electroanal. Chem.* **198** (1986) 149.
5. B. E. Conway and B. V. Tilak, "Interfacial processes involving electrocatalytic evolution and oxidation of H<sub>2</sub>, and the role of chemisorbed H", *Electrochim. Acta* **47** (2002) 3571.
6. I. Fishtik, C. A. Callaghan, J. D. Fehribach, and R. Datta, "A reaction route graph analysis of the electrochemical hydrogen oxidation and evolution reactions", *J. Electroanal. Chem.* **576** (2005) 57.
7. M. R. Tarasevich, A. Sadkowsky, and E. Yeager, *Comprehensive Treatise of Electrochemistry*, **Vol. 7** (Eds.: B. E. Conway, J. O. Bockris, E. Yeager, S. U. M. Khan, R. E. White), Plenum Press, New York (1983) 301.
8. V. R. Stamenkovic, B. Fowler, B. S. Mun, G. F. Wang, P. N. Ross, C. A. Lucas, and N. M. Markovic, "Improved oxygen reduction activity on Pt<sub>3</sub>Ni(111) via increased surface site availability", *Science* **315** (2007) 493.

9. R. Ferrando, J. Jellinek, and R. L. Johnston, "Nanoalloys: From theory to applications of alloy clusters and nanoparticles", *Chem. Rev.* **108** (2008) 845.
10. A. Christensen, A. V. Ruban, P. Stoltze, K. W. Jacobsen, H. L. Skriver, J. K. Norskov, and F. Besenbacher, "Phase diagrams for surface alloys", *Phys. Rev. B* **56** (1997) 5822.
11. Y. G. Ma, and P. B. Balbuena, "Pt surface segregation in bimetallic Pt<sub>3</sub>M alloys: A density functional theory study", *Surf. Sci.* **602** (2008) 107.
12. K. J. J. Mayrhofer, V. Juhart, K. Hartl, M. Hanzlik, and M. Arenz, "Adsorbate-Induced Surface Segregation for Core-Shell Nanocatalysts", *Angew. Chem. Int. Ed.* **48** (2009) 3529.
13. B. J. Hwang, S. M. S. Kumar, C. H. Chen, Monalisa, M. Y. Cheng, D. G. Liu, and J. F. Lee, "An investigation of structure-catalytic activity relationship for Pt-Co/C bimetallic nanoparticles toward the oxygen reduction reaction", *J. Phys. Chem. C* **111** (2007) 15267.
14. S. Park, A. Wieckowski, and M. J. Weaver, "Electrochemical infrared characterization of CO domains on ruthenium-decorated platinum nanoparticles", *J. Am. Chem. Soc.* **125** (2003) 2282.
15. F. A. Cotton, L. M. Daniels, C. Y. Liu, C. A. Murillo, A. J. Schultz, and X. P. Wang, "How to make a major shift in a redox potential: Ligand control of the oxidation state of dimolybdenum units", *Inorg. Chem.* **41** (2002) 4232.
16. A. Ruban, B. Hammer, P. Stoltze, H. L. Skriver, and J. K. Norskov, "Surface electronic structure and reactivity of transition and noble metals", *J. Mol. Catal. A: Chem.* **115** (1997) 421.

17. F. Gautier and A. M. Llois, "Adhesion of Transition-Metals — Energies and Thin Film Deposition — an Electronic Approach", *Surf. Sci.* **245** (1991) 191.
18. V. F. Puentes, K. M. Krishnan, and A. P. Alivisatos, "Colloidal nanocrystal shape and size control: The case of cobalt", *Science* **291** (2001) 2115.
19. N. Chakroune, G. Viau, S. Ammar, L. Poul, D. Veautier, M. M. Chehimi, C. Mangeney, F. Villain, and F. Fievet, "Acetate- and thiol-capped monodisperse ruthenium nanoparticles: XPS, XAS, and HRTEM studies", *Langmuir* **21** (2005) 6788.
20. L. M. Qiu, F. Liu, L. Z. Zhao, W. S. Yang, and J. N. Yao, "Evidence of a unique electron donor-acceptor property for platinum nanoparticles as studied by XPS", *Langmuir* **22** (2006) 4480.
21. T. Bligaard and J. K. Norskov, "Ligand effects in heterogeneous catalysis and electrochemistry", *Electrochim. Acta* **52** (2007) 5512.
22. H. A. Gasteiger, N. Markovic, P. N. Ross, and E. J. Cairns, "Methanol Electro-oxidation on Well-characterized Pt-Ru Alloys", *J. Phys. Chem.* **97** (1993) 12020.
23. E. Christoffersen, P. Stoltze, and J. K. Norskov, "Monte Carlo simulations of adsorption-induced segregation", *Surf. Sci.* **505** (2002) 200.
24. V. R. Stamenkovic, B. S. Mun, K. J. J. Mayrhofer, P. N. Ross, and N. M. Markovic, "Effect of surface composition on electronic structure, stability, and electrocatalytic properties of Pt-transition metal alloys: Pt-skin versus Pt-skeleton surfaces", *J. Am. Chem. Soc.* **128** (2006) 8813.
25. S. Koh, J. Leisch, M. F. Toney, and P. Strasser, "Structure-activity-stability relationships of Pt-Co alloy electrocatalysts in gas-diffusion electrode layers", *J. Phys. Chem. C* **111** (2007) 3744.

26. H. A. Gasteiger, S. S. Kocha, B. Sompalli, and F. T. Wagner, "Activity benchmarks and requirements for Pt, Pt-alloy, and non-Pt oxygen reduction catalysts for PEMFCs", *Appl. Catal. B: Environ.* **56** (2005) 9.
27. R. Srivastava, P. Mani, N. Hahn, and P. Strasser, "Efficient oxygen reduction fuel cell electrocatalysis on voltammetrically dealloyed Pt-Cu-Co nanoparticles", *Angew. Chem. Int. Ed.* **46** (2007) 8988.
28. S. Chen, P. J. Ferreira, W. C. Sheng, N. Yabuuchi, L. F. Allard, and Y. Shao-Horn, "Enhanced activity for oxygen reduction reaction on "Pt<sub>3</sub>CO" nanoparticles: Direct evidence of percolated and sandwich-segregation structures", *J. Am. Chem. Soc.* **130** (2008) 13818.
29. J. R. Chelikowsky, "Predictions for Surface Segregation in Intermetallic Alloys", *Surf. Sci.* **139** (1984) L197.
30. G. Treglia and B. Legrand, "Surface-Sandwich Segregation in Pt-Ni and Ag-Ni Alloys - 2 Different Physical Origins for the Same Phenomenon", *Phys. Rev. B* **35** (1987) 4338.
31. S. M. Foiles, M. I. Baskes, and M. S. Daw, "Embedded-Atom-Method Functions for the Fcc Metals Cu, Ag, Au, Ni, Pd, Pt, and Their Alloys", *Phys. Rev. B* **33** (1986) 7983.
32. M. Schmid, W. Hofer, P. Varga, P. Stoltze, K. W. Jacobsen, and J. K. Norskov, "Surface Stress, Surface Elasticity, and the Size Effect in Surface Segregation", *Phys. Rev. B* **51** (1995) 10937.
33. A. V. Ruban, H. L. Skriver, and J. K. Norskov, "Surface segregation energies in transition-metal alloys", *Phys. Rev. B* **59** (1999) 15990.

34. O. M. Lovvik, "Surface segregation in palladium based alloys from density-functional calculations", *Surf. Sci.* **583** (2005) 100.
35. G. F. Wang, M. A. Van Hove, P. N. Ross, and M. I. Baskes, "Monte Carlo simulations of segregation in Pt-Ru catalyst nanoparticles", *J. Chem. Phys.* **121** (2004) 5410.
36. S. Gonzalez, K. M. Neyman, S. Shaikhutdinov, H. J. Freund, and F. Illas, "On the promoting role of Ag in selective hydrogenation reactions over Pd-Ag bimetallic catalysts: A theoretical study", *J. Phys. Chem. C* **111** (2007) 6852.
37. C. A. Menning and J. G. G. Chen, "General trend for adsorbate-induced segregation of subsurface metal atoms in bimetallic surfaces", *J. Chem. Phys.* **130** (2009) 174709.
38. J. Greeley and J. K. Norskov, "Electrochemical dissolution of surface alloys in acids: Thermodynamic trends from first-principles calculations", *Electrochim. Acta* **52** (2007), 5829.
39. V. R. Stamenkovic, B. Fowler, B. S. Mun, G. F. Wang, P. N. Ross, C. A. Lucas, and N. M. Markovic, "Improved oxygen reduction activity on Pt<sub>3</sub>Ni(111) via increased surface site availability", *Science* **315** (2007) 493.
40. B. Hammer and J. K. Norskov, "Theoretical surface science and catalysis - Calculations and concepts", *Adv. Catal.* **45** (2000) 71.
41. J. K. Norskov, J. Rossmeisl, A. Logadottir, L. Lindqvist, J. R. Kitchin, T. Bligaard, and H. Jonsson, "Origin of the overpotential for oxygen reduction at a fuel-cell cathode", *J. Phys. Chem. B* **108** (2004) 17886.
42. J. Greeley, I. E. L. Stephens, A. S. Bondarenko, T. P. Johansson, H. A. Hansen, T. F. Jaramillo, J. Rossmeisl, I. Chorkendorff, and J. K. Norskov, "Alloys of platinum and

early transition metals as oxygen reduction electrocatalysts”, *Nature Chem.* **1** (2009) 552.

43. J. R. Kitchin, J. K. Norskov, M. A. Barteau, and J. G. Chen, “Modification of the surface electronic and chemical properties of Pt(111) by subsurface 3d transition metals”, *J. Chem. Phys.* **120** (2004) 10240.

44. M. Arenz, K. J. J. Mayrhofer, V. Stamenkovic, B. B. Blizanac, T. Tomoyuki, P. N. Ross, and N. M. Markovic, “The effect of the particle size on the kinetics of CO electrooxidation on high surface area Pt catalysts”, *J. Am. Chem. Soc.* **127** (2005) 6819.

45. K. J. J. Mayrhofer, M. Arenz, B. B. Blizanac, V. Stamenkovic, P. N. Ross, and N. M. Markovic, “CO surface electrochemistry on Pt-nanoparticles: A selective review”, *Electrochim. Acta* **50** (2005) 5144.

46. D.-H. Lim, W.-D. Lee, D.-H. Choi, and H.-I. Lee, “Effect of ceria nanoparticles into the Pt/C catalyst as cathode material on the electrocatalytic activity and durability for low-temperature fuel cell”, *Appl. Catal. B-Environ.* **94** (2010) 85.

47. K. M. McGrath, P. G. K. Surya, and G. A. Olah, “Direct methanol fuel cells”, *J. Ind. Eng. Chem.* **10** (2004) 1063.

48. S. Ge, X. Li, B. Yi, and I.-M. Hsing, “Absorption, desorption, and transport of water in polymer electrolyte membranes for fuel cells”, *J. Electrochem. Soc.* **152** (2005) A1149.

49. G. Lin and T. V. Nguyen, “Effect of thickness and hydrophobic polymer content of the gas diffusion layer on electrode flooding level in a PEMFC”, *J. Electrochem. Soc.* **152** (2005) A1942.

50. R. F. Silva, S. Passerini, and A. Pozio, "Solution-cast Nafion/montmorillonite composite membrane with low methanol permeability", *Electrochim. Acta* **50** (2005) 2639.
51. T. C. Deivaraj and J. Y. Lee, "Preparation of carbon-supported PtRu nanoparticles for direct methanol fuel cell applications-a comparative study", *J. Power Sources* **142** (2005) 43.
52. K.-W. Park and Y.-E. Sung, "Design of nanostructured electrocatalysts for direct methanol fuel cells", *J. Ind. Eng. Chem.* **12** (2006) 165.
53. J.-S. Choi, W.-S. Chung, H.-Y. Ha, T.-H. Lim, I.-H. Oh, and H.-I. Lee, "Nano-structured Pt-Cr anode catalyst over carbon support for direct methanol fuel cell", *J. Power Sources* **156** (2006) 466.
54. Z. Zhou, S. Wang, W. Zhou, L. Jiang, G. Wang, and G. Sun, "Preparation of highly active Pt/C cathode electrocatalysts for DMFCs by an improved aqueous impregnation method", *Phys. Chem. Chem. Phys.* **5** (2003) 5485..
55. M. S. Wilson and S. Gottesfeld, "Thin-film catalyst layers for polymer electrolyte fuel cell electrodes", *J. Appl. Electrochem.* **22** (1992) 1.
56. Z. Liu, L. M. Gan, L. Hong, W. Chen, and J. Y. Lee, "Carbon-supported Pt nanoparticles as catalysts for proton exchange membrane fuel cells", *J. Power Sources* **139** (2005) 73.
57. X. Yan, H. Liu, and K. Y. Liew, "Size control of polymer-stabilized ruthenium nanoparticles by polyol reduction", *J. Mater. Chem.* **11** (2001) 3387.
58. T. Matsumoto, T. Komatsu, K. Arai, T. Yamazaki, M. Kijima, and H. Shimizu, "Reduction of Pt usage in fuel cell electrocatalysts with carbon nanotube electrodes", *Chem. Commun.* **7** (2004) 840.

59. C. M. Y. Yeung, K. M. K. Yu, Q. J. Fu, D. Thompsett, M. I. Petch, and S. C. Tsang, "Engineering Pt in ceria for a maximum metal-support interaction in catalysis", *J. Am. Chem. Soc.* **127** (2005) 18010.
60. M. Watanabe, S. Saegusa, and P. Stonehart, "High platinum electrocatalyst utilizations for direct methanol oxidation", *J. Electroanal. Chem.* **271** (1989) 213..
61. B. Fang, N. K. Chaudhari, M.-S. Kim, J. H. Kim, and J.-S. Yu, "Homogeneous deposition of platinum nanoparticles on carbon black for proton exchange membrane fuel cell", *J. Am. Chem. Soc.* **131** (2009) 15330.
61. J. Guo, G. Sun, S. Sun, S. Yan, and W. Yang, Qi, "Polyol-synthesized PtRu/C and PtRu black for direct methanol fuel cells", *J. Power Sources* **168** (2007) 299.
62. M. Tsuji, M. Hashimoto, Y. Nishizawa, and T. Tsuji, "Synthesis of gold nanorods and nanowires by a microwave-polyol method", *Mater. Lett.* **58** (2004) 2326.
63. Y.-J. Zhu and X.-L. Hu, "Preparation of powders of selenium nanorods and nanowires by microwave-polyol method", *Mater. Lett.* **58** (2004) 1234.
64. S. Song, Y. Wang, and P K. Shen, "Pulse-microwave assisted polyol synthesis of highly dispersed high loading Pt/C electrocatalyst for oxygen reduction reaction", *J. Power Sources* **170** (2007) 46.
65. H. S. Oh, J.-G. Oh, Y.-G. Hong, and H. Kim, "Investigation of carbon-supported Pt nanocatalyst preparation by the polyol process for fuel cell applications", *Electrochim. Acta.* **52** (2007) 7278.
66. J. M. Garcia-Cortes, J. Perez-Ramirez, M. J. Illan-Gomez, and C. Salinas-Martinez de Lecea. "Activation by sintering of Pt-beta catalysts in deNO<sub>x</sub> HC-SCR. Structure-activity relationships", *Catal. Commun.* **4** (2003) 165.

67. J. C. Chastoi, "Reactions of oxygen with the platinum metals: II-Oxidation of ruthenium, rhodium, iridium and osmium", *Platinum Metal. Rev.* **9** (1965) 51.
68. V. Radmilovic, Y. Richardson, S. J. Chen, and P. N. Ross, "Carbon-supported Pt-Sn electrocatalysts for the anodic oxidation of H<sub>2</sub>, CO, and H<sub>2</sub>/CO mixtures Part I. Microstructural characterization", *J. Catal.* **232** (2005) 199.
69. D.-H. Lim, W.-D. Lee, D.-H. Choi, H.-H. Kwon, and H.-I. Lee, "The effect of cerium oxide nanoparticles on a Pt/C electrocatalyst synthesized by a continuous two-step process for low-temperature fuel cell", *Electrochem. Commun.* **10** (2008) 592.
70. V. Radmilovic, H. A. Gasteiger, and P. N. Ross, "Structure and chemical composition of a supported Pt-Ru electrocatalyst for methanol oxidation", *J. Catal.* **154** (1995) 98.
71. D.-H. Lim, W.-D. Lee, D.-H. Choi, D.-R. Park, and H.-I. Lee, "Preparation of platinum nanoparticles on carbon black with mixed binary surfactants: Characterization and evaluation as anode catalyst for low-temperature fuel cell", *J. Power Sources* **185** (2008) 159.
72. P. F. J. Nores, I. M. J. Vilella, H. Troiani, M. Granada, S. R. Miguel, and O. A. Scelza, "Catalytic activity vs. size correlation in platinum catalysts of PEM fuel cells prepared on carbon black by different methods", *Int. J. Hydrogen Energy* **34** (2009) 8193.
73. Z. Zhou, S. Wang, W. Zhou, G. Wang, L. Jiang, and W. Li, "Novel synthesis of highly active Pt/C cathode electrocatalyst for direct methanol fuel cell", *Chem. Commun.* **5** (2003) 394.
74. E. A. Baranova, Y. L. Page, D. Ilin, C. Bock, B. Macdougall, and P. H. J. Mercier, "Size and composition for 1–5 nm Ø PtRu alloy nano-particles from Cu K $\alpha$  X-ray patterns", *J. Alloys Compd.* **471** (2009) 387.

75. C. Bock, C. Paquet, M. Couillard, G. A. Botton, and B. R. MacDougall, "Size-selected synthesis of PtRu nano-catalysts: reaction and size control mechanism", *J. Am. Chem. Soc.* **126** (2004) 8028.
76. H. A. Gasteiger, N. M. Markovic, and P. N. Ross, "H<sub>2</sub> and CO electrooxidation on well-characterized Pt, Ru, and Pt-Ru. 1. rotating disk electrode studies of the pure gases including temperature effects", *J. Phys. Chem.* **99** (1995) 8290.
77. G. García, J. Florez-Montaño, A. Hernandez-Creus, E. Pastor, and G. A. Planes, "Methanol electrooxidation at mesoporous Pt and Pt-Ru electrodes: A comparative study with carbon supported materials", *J. Power Sources* **196** (2011) 2979.
78. L. Feng, Q. Lv, X. Sun, S. Yao, C. Liu, and W. Xing. "Enhanced activity of molybdovanadophosphoric acid modified Pt electrode for the electrooxidation of methanol", *J. Electroanal. Chem.* **664** (2012) 14.
79. L. W. Liao, S. X. Liu, Q. Tao, B. Geng, P. Zhang, and C. M. Wang, "A method for kinetic study of methanol oxidation at Pt electrodes by electrochemical in situ infrared spectroscopy", *J. Electroanal. Chem.* **650** (2011) 233.
80. J. Tayal, B. Rawat, and S. Basu, "Effect of addition of rhenium to Pt-based anode catalysts in electro-oxidation of ethanol in direct ethanol PEM fuel cell", *Int. J. Hydrogen Energy* **37** (2012) 4597.
81. X. Zhao, M. Yin, L. Ma, L. Liang, C. Liu, and J. Liao, "Recent advances in catalysts for direct methanol fuel cells", *Energy Environ. Sci.* **4** (2011) 2736.
82. S. Wang, S. P. Jiang, X. Wang, and J. Guo, "Enhanced electrochemical activity of Pt nanowire network electrocatalysts for methanol oxidation reaction of fuel cells", *Electrochim. Acta* **56** (2011) 1563.

83. D. M. Wood, "Classical size dependence of the work function of small metallic spheres", *Phys. Rev. Lett.* **46** (1981) 749.
84. P. A. Chernavskii, N. V. Peskov, A. V. Mugtasimov, and V. V. Lunin, "Oxidation of metal nanoparticles: experiment and model", *Russ. J. Phys. Chem. B* **4** (2007) 394.
85. S. Wenchao, C. Shuo, V. Elio, and S.-H. Yang, "Size influence on the oxygen reduction reaction activity and instability of supported Pt nanoparticles", *J. Electrochem. Soc.* **159** (2012) B96.
86. P.-L. Kuo, W.-F. Chen, H. Y. Hhang, I.-C. Chang, and S. A. Dia, "Stabilizing effect of pseudo-dendritic polyethylenimine on platinum nanoparticles supported on carbon", *J. Phys. Chem. B* **110** (2006) 3071.
87. B. C. Han, C. R. Miranda, and G. Ceder, "Effect of particle size and surface structure on adsorption of O and OH on platinum nanoparticles: A first-principles study", *Physical Review B* **77** (2008) 075410.
88. Y.-T. Kim and T. Mitani, "Surface thiolation of carbon nanotubes as supports: A promising route for the high dispersion of Pt nanoparticles for electrocatalysts", *J. Catal.* **238** (2006) 394.
89. J. Wang, G. Yin, Y. Shao, Z. Wang, and Y. Gao, "Platinum deposition on multiwalled carbon nanotubes by ion-exchange method as electrocatalysts for oxygen reduction", *J. Electrochem. Soc.* **154** (2007) B687.
90. G. Wu, G. Cui, D. Li, P.-K. Shen, and N. Li, "Carbon-supported  $\text{Co}_{1.67}\text{Te}_2$  nanoparticles as electrocatalysts for oxygen reduction reaction in alkaline electrolyte", *J. Mater. Chem.* **19** (2009) 6581.

91. M. Teliska, V. S. Murthi, S. Mukerjee, and D. E. Ramaker, "Correlation of water activation, surface properties, and oxygen reduction reactivity of supported Pt-M/C bimetallic electrocatalysts using XAS", *J. Electrochem. Soc.* **152** (2005) A2159.
92. M. P. Sotelo, H. R. G. González, M. J. G. Cabañas, and F. O. Solorza, "Mechanically milled  $Ru_xFe_y$  electrocatalyst for oxygen reduction in acid media", *Int. J. Electrochem. Sci.* **2** (2007) 523.
93. D.-W. Jung, S. Park, C.-Y. Ahn, J.-B. Kim, and E.-S. Oh, "Performance comparison of  $Pt_{1-x}Pd_x$ /carbon nanotubes catalysts in both electrodes of polymer electrolyte membrane fuel cells", *Fuel Cells*, **12** (2012) 398.
94. G. Faubert, D. Guay, and J. P. dodelet, "Pt Inclusion Compounds as Oxygen Reduction Catalysts in Polymer Electrolyte Fuel Cells", *J. Electrochem. Soc.*, **145** (1998) 2985.
95. M. Eikerling and A. A Kornyshev, "Modelling the performance of the cathode catalyst layer polymer electrolyte fuel cell", *J. Electroanal. Chem.* **453** (1998) 89.
96. A. K. Shukla, M. Neergat, P. Bera, V. Jayaram, and M. S. Hegde, "An XPS study on binary and ternary alloys of transition metals with platinumized carbon and its bearing upon oxygen electroreduction in direct methanol fuel cells", *J. Electronanl. Chem.* **504** (2001) 111.
97. G. Tamizhmani and G. A. Capuano, "Improved Electrocatalytic Oxygen Reduction performance of Platinum Ternary Alloy-Oxide in Solid-Polymer-Electrolyte Fuel Cell", *J. Electrochem. Soc.* **141** (1994) 968.
98. A. Freund, J. Lang, T. Lehmann, and K. A. Starz, "Improved Pt alloy catalysts for fuel cells", *Catal. Today* **27** (1996) 279.

99. T. Toda, H. Igarashi, and M. Watanabe, "Role of Electronic Property of Pt and Pt alloy on Electrocatalytic Reduction of Oxygen", *J. Electrochem. Soc.* **145** (1998) 4185.
100. M. Min, J. Cho, K. Cho, and H. Kim, "Particle size and alloying effects of Pt-based alloy catalysts for fuel cell applications", *Electrochim. Acta*, **45** (2000) 4211.
101. A. S. Arico, A. K. Shukla, H. Kim, S. Park, M. Min, and V. Antonucci, "An XPS study on oxidation states of Pt and its alloys with Co and Cr and its relevance to electroreduction of oxygen", *Appl. Surf. Sci.*, **172** (2001) 33.
102. M. Neergat, A. K. Shukla, and K. S. Gandhi, "Platinum-based Alloys as Oxygen-Reduction Catalysts for Solid-Polymer-Electrolyte Direct Methanol Fuel Cells", *J. Appl. Electrochem.* **31** (2001) 373.
103. U. A. Paulus, A. Wokaun, G. G. Scherer, T. J. Schmidt, V. Stamenkovic, V. Radmilovic, N. M. Markovic, and P. N. Ross, "Oxygen Reduction on Carbon-Supported Pt-Ni and Pt-Co Alloy Catalysts", *J. Phys. Chem. B*, **106** (2002) 4181.
104. V. Stamenkovic, T. J. Schmidt, P. N. Ross, and N. M. Markovic, "Surface Composition Effects in Electrocatalysis: Kinetics of Oxygen Reduction on Well-Defined Pt<sub>3</sub>Ni and Pt<sub>3</sub>Co Alloy Surfaces", *J. Phys. Chem. B*, **106** (2002) 11970.
105. M. D. Obradovic, B. N. Grgur, and L. M. Vracar, "Adsorption of oxygen containing species and their effect on oxygen reduction of Pt<sub>3</sub>Co electrode", *Electroanal. Chem.* **548** (2003) 69.
106. F. H. B. Lima and E. A. Ticianelli, "Oxygen electrocatalysis on ultra-thin porous coating rotating ring/disk platinum and platinum-cobalt electrodes in alkaline media", *Electrochim. Acta* **49** (2004) 4091.

107. J. F. Drillet, A. Ee, J. Friedemnan, R. Kotz, and V. M. Schmidt, "Oxygen reduction at Pt and Pt<sub>70</sub>Ni<sub>30</sub> in H<sub>2</sub>SO<sub>4</sub>/CH<sub>3</sub>OH solution", *Electrochim. Acta* **47** (2002) 1983.
108. J. E. Antolini, R. R. Passos, and E. A. Ticianelli, "Electrocatalysis of oxygen reduction on a carbon supported platinum-vanadium alloy in polymer electrolyte fuel cells", *Electrochim. Acta* **48** (2002) 263.
109. T. Toda, H. Igarashi, H. Uchida, and M. Watanabe, "Enhancement of the Electroreduction of Oxygen on Pt Alloys with Fe, Ni, and Co", *J. Electrochem. Soc.* **146** (1999) 3750.
110. L. Wan, T. Moriyama, M. Ito, H. Uchida, and M. Watanabe, "In situ STM imaging of surface dissolution and rearrangement of a Pt-Fe alloy electrocatalyst in electrolyte solution", *Chem. Commun.* (2002) 58.
111. B. C. Beard and P. N. Ross Jr., "Discharge Behavior and Thermal Stability of Synthetic FeS<sub>2</sub> Cathode Material", *J. Electrochem. Soc.* **137** (1990) 3368.
112. M. T. Paffett, J. G. Berry, and S. Gottesfeld, "On the Anodic Oxidation of Formaldehyde during the Electroless Copper Plating Process", *J. Electrochem. Soc.* **135** (1988) 1431.
113. V. Jalan and E. J. Taylor, "Importance of Interatomic Spacing in Catalytic Reduction of Oxygen in Phosphoric Acid", *J. Electrochem. Soc.* **130** (1983) 2299.
114. O. Saavadogo and A. Essalik, "Effect of Platinum Particle Size on the Oxygen Reduction Reaction on 2% Pt-1% H<sub>2</sub>SO<sub>4</sub> in Phosphoric Acid", *J. Electrochem. Soc.* **143** (1996) 1814.
115. Z. Sun, H. C. Chiu, and A. C. C. Tseung, "Oxygen Reduction on Teflon Bonded Pt/WO<sub>3</sub>/C Electrode in Sulfuric Acid", *Electrochem. Solid-State Lett.* **4** (2001) E9.

116. M. P. Rosynek, "Catalytic Properties of Rare Earth Oxides", *Catal. Rev.* **16** (1997) 111.
117. C. PerKins, M. Henderson, C. Peden, and G. Herman, "Self-diffusion in ceria", *J. Vac. Sci. Technol. A* **19** (2001) 1942.
118. W.-S. Shin, C.-R. Jung, J. Han, S.-W. Nam, T.-H. Lim, S.-A. Hong, and H.-I. Lee, "Development of Au/CeO<sub>2</sub> Catalysts for Preferential Oxidation of CO in PEMFC", *J. Ind. Eng. Chem.* **10** (2004) 302.
119. J. Nunan, H. Robbta, M. Cohn, and S. Bradley, "Physicochemical properties of Ce-containing three-way catalysts and the effect of Ce on catalyst activity", *J. Catal.* **133** (1992) 309.
120. H. C. Yao and Y. F. Yao, "Ceria in automotive exhaust catalysts: I. Oxygen storage", *J. Catal.* **866** (1984) 254.
121. H. B. Yu, J.-H. Kim, H.-I. Lee, M. A. Scibioh, J.-Y. Lee, J.-H. Han, S.-P. Yoon, and H. Y. Ha, "Development of nanophase CeO<sub>2</sub>-Pt/C cathode catalyst for direct methanol fuel cell", *J. Power Sources* **140** (2005) 59.
122. G. Vlaic, P. Fornasiero, S. Geremia, J. Kaspar, and M. Graziani, *J. Catal.* **168** (1997) 386.
123. V. R. Stamenkovis and B. S. Mun, "Trends in electrocatalysis on extended and nanoscale Pt-bimetallic alloy surfaces", *Nat. Mater.* **6** (2007) 241.
124. B. I. Nabivanets and L. V. Kalabina, "State of Palladium(II) in Perchlorate Solutions", *Russ. J. Inorg. Chem.* **15** (1970) 818.
125. H. Li, G. Sun, N. Li, S. Sun, D. Su, and Q. Xin, "Design and preparation of highly Pt-Pd/C catalyst for the oxygen reduction reaction", *J. Phys. Chem. C* **111** (2007) 5605.

126. R. M. Navarro, B. Pawelec, J. M. Trejo, R. Mariscal, and J. L. G. Fierro, "Aromatics Hydrogenation over Sulfur-resistant Pt-Pd alloys", *J. Catal.* **189** (2000) 184.

## 초 록

고분자전해질막 연료전지는 상대적으로 낮은 온도에서 작동되며 오염물질의 배출이 거의 없거나 극히 미미한 양이 발생하기 때문에 수송용도로의 적용에 상당히 각광을 받고 있다. 그러나 공기극의 반응속도가 매우 느리며, 백금 기반의 촉매 사용에 따른 높은 가격으로 인하여 상업화가 어려운 실정이다. 이미 많은 연구들을 통하여 연료전지의 활성 한계는 공기극에서 발생하는 열역학적 전위차, 즉 공기극의 과전압에 의한 것이라고 밝혀졌다. 이의 해결방안으로, 백금의 이용률 증가, 백금에 다른 금속의 첨가, 탄소담체의 성능개선 등이 제시되고 있다. 본 연구에서는 전극촉매의 구조를 조절하여 산소환원반응의 활성을 증가시키는 연구를 수행하였다.

현재 고분자전해질막 연료전지의 공기극 촉매는 낮은 온도에서 높은 산소환원반응 활성을 보이는 백금의 특성으로 인해 탄소에 담지된 백금촉매가 가장 적합한 촉매로 알려져 있다. 그러나 백금은 고가의 귀금속이기 때문에 작은 크기의 백금입자를 제조하여 활성표면적을 늘리고 사용량을 줄여야 한다. 본 연구에서는 백금나노입자를 작게 만들 수 있는 방법으로 알려진 폴리올환원법의 반응조건을 조절하여 작은 백금나노입자를 제조하고자 하였다. 이를 통해 1.2 nm의 작은 크기를 갖는 백금나노입자를 개발할 수 있었으며, 작은 크기로 인한 활성표면적의 증가효과를 가져왔다.

세리아-지르코니아 복합산화물을 수열합성법으로 제조하여 탄소와 함께 담체로 사용하는 백금촉매를 제조하였다. 세리아-지르코니아 복합산화물의 입자크기와 결정화도를 조절하면서 백금의 산소환원반응에 미치는 영향을

살펴 본 결과, 세리아-지르코니아 복합산화물의 표면에 존재하는 OH가 산소환원반응이 일어나는 동안 전해질로부터 백금에 흡착하는 OH의 흡착을 막아 백금표면의 산소환원반응의 활성을 증가시켰다.

폴리올환원법으로 금속나노입자를 제조할 때, 금속전구체간의 환원속도차를 이용하여 코어-셸과 유사한 형태의 구조를 갖는 백금-팔라듐 나노입자를 제조하였다. 제조된 나노입자는, 백금이 주성분인 내부층에 의하여 작은 입자크기와 증가된 활성면적을 보였으며, 표면층에 존재하는 팔라듐에 의하여 높은 산소환원반응 성능을 보여주었다. 또한 제조된 코어-셸 유사 형태의 백금-팔라듐 나노입자에 세리아-지르코니아 복합산화물을 더하여 우수한 산소환원반응 활성을 갖는 촉매를 개발하였다.

**주요어:** 고분자전해질막 연료전지, 백금나노입자, 세리아-지르코니아  
복합산화물, 백금-팔라듐 나노입자, 폴리올환원법  
**학 번:** 2006-23220